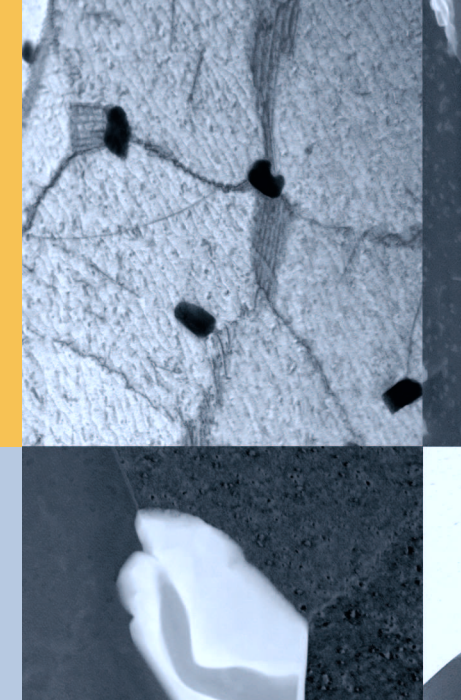
Microstructure Evolution of Laves Phase Strengthened Ferritic Steels for High Temperature Applications

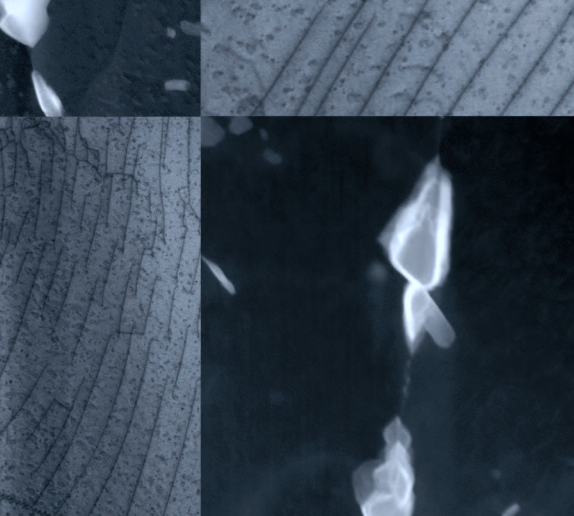
Jennifer Katharina Lopez Barrilao

375

Microstructure of Laves Phase Strengthened Steels







JÜLICH

J.K. Lopez Barrilao

Energie & Umwelt/ **Energy & Environment** Band/Volume 375 ISBN 978-3-95806-231-3



Energie & Umwelt/ Energy & Environment Band/Volume 375 ISBN 978-3-95806-231-3



Forschungszentrum Jülich GmbH Institute of Energy and Climate Research (IEK) Microstructure and Properties of Materials (IEK-2)

Microstructure Evolution of Laves Phase Strengthened Ferritic Steels for High Temperature Applications

Jennifer Katharina Lopez Barrilao

Bibliographic information published by the Deutsche Nationalbibliothek. The Deutsche Nationalbibliothek lists this publication in the Deutsche Nationalbibliografie; detailed bibliographic data are available in the Internet at http://dnb.d-nb.de.

Publisher and Forschungszentrum Jülich GmbH

Distributor: Zentralbibliothek

52425 Jülich

Tel: +49 2461 61-5368 Fax: +49 2461 61-6103

Email: zb-publikation@fz-juelich.de

www.fz-juelich.de/zb

Cover Design: Grafische Medien, Forschungszentrum Jülich GmbH

Printer: Grafische Medien, Forschungszentrum Jülich GmbH

Copyright: Forschungszentrum Jülich 2017

Schriften des Forschungszentrums Jülich Reihe Energie & Umwelt / Energy & Environment, Band / Volume 375

D 82 (Diss. RWTH Aachen University, 2016)

ISSN 1866-1793 ISBN 978-3-95806-231-3

The complete volume is freely available on the Internet on the Jülicher Open Access Server (JuSER) at www.fz-juelich.de/zb/openaccess.



This is an Open Access publication distributed under the terms of the <u>Creative Commons Attribution License 4.0</u>, which permits unrestricted use, distribution, and reproduction in any medium, provided the original work is properly cited.

List of Symbols and Abbreviations

Symbols ΔG_{Def} Saved free enthalpy[J] Free lattice deformation enthalpy [J] $\Delta G_{\rm m}$ ΔG_{Ph} Total free enthalpy[J] $\Delta G_{\rm total}$ ΔG_{V} Creep rate[s⁻¹] Secondary creep rate $\dots [s^{-1}]$ $\dot{\varepsilon}_S$ Concentration of vacancy defects.....[-] c_{L}^{a} Saturation concentration [mol m⁻³] c_0 $C_{\rm c}$ Chromatic aberration coefficient [nm] Spherical aberration coefficient [nm] C_{S} $d_{\rm c}$ Chromatic aberration.....[nm] d_{S} Lattice spacing with Miller indices hkl......[nm] d_{hkl} Distance between slip planes [m] $d_{\mathbf{s}}$ Energy[J] E_r G_i^0 Gibbs free energy of a pure phase of component i..........[J mol⁻¹] G_{m} Molar Gibbs free energy [J mol⁻¹] ${\rm H_B^L}$ Enthalpy of formation of vacancy defects [JK⁻¹]

$\dots [J \text{ mol}^{-1}]$	Redlich-Kister coefficient	$ m L_{ij}$	
[kg]	Rest mass of an electron	m_0	
$\ldots \ldots [m]$	Initial mean particle radius	$ m r_{T_0}$	
[m]	Mean particle radius after coarsening	$ m r_{T}$	
[JK ⁻¹]	Oscillation entropy of vacancy defects	$S_{ m v}^{ m L}$	
[V]	Acceleration voltage	U_{A}	
[mol]	Molar fraction of the component i	x_i	
[°]	Tilt angle	Θ	
[°]	Aperture angle	α	
[kg s ⁻²]	Effective boundary energy	γ	
[Jm ⁻²]	Specific enthalpy of phase boundary	$\gamma_{\rm Ph}$	
[nm]	Wavelength	λ	
[-]	Poisson's ratio	γ	
[m ⁻²]	Dislocation density	ρ	
[GPa]	Peierls-Nabarro stress	$ au_{ m P}$	
[-,%]	Time-independent initial strain	$arepsilon_0$	
[-,%]	Elastic strain part of ε_0	$arepsilon_e$	
[-,%]	Creep strain	$arepsilon_f$	
[-,%]	Plastic strain part of ε_0	$arepsilon_i$	
[-,%]	Total strain	$arepsilon_t$	
[kg s ⁻² m ⁻¹]	Field of tension	$\vec{\sigma}$	
[m]	Norm of the Burgers vector	$ \mathbf{b} $	
[kg m s ⁻²]	Norm of Peach-Koehler force	K	
[m]	Norm of line element	s	
[ms ⁻¹]	Speed of light	c	
$\dots \dots [m^2s^{-1}]$	Diffusion constant	D	
[m]	Distance of dislocations	d	
$\dots \dots [m^2s^{-1}]$	Material-dependent diffusion constant	D_0	

E	Modulus of elasticity [GPa]
e	Elementary charge [C]
G	Shear modulus [GPa]
g	Resolution[nm]
h	$Dislocation \ hardening[m^{-2}s^1]$
\mathbf{h}_p	Planck's constant
J	$\label{eq:matter-flux} \text{Matter flux} \ \dots \dots [\text{mol } m^{-2}s^{-1} \]$
k	Boltzmann constant
k_{c}	Coarsening constant
m	Mass of a particle [kg]
n	Refractive index
p	Momentum of a particle [Ns]
Q	Activation energy [J mol^{-1}]
r	$Dislocation \ softening. \qquad \qquad [m^{-2}s^1]$
R	Ideal gas constant [J $\mathrm{mol^{-1}K^{-1}}$]
Т	Temperature [K]
v	Velocity of a particle
Abbreviation	\mathbf{s}
AFM	Advanced Ferritic-Martensitic
APU	Auxiliary Power Unit
ATP	Atom Probe Tomography
BF	Bright Field
BSE	Backscattered Electron
Calphad	Calculation of Phase Diagrams
COST	Cooperation in Science and Technology
CS	Creep Specimens
DF	Dark Field
EBSD	Electron Backscattered Diffraction

ECCC European Creep Collaborative Committee

ECD Equivalent Circle Diameter

EDX Energy Dispersive X-ray

EPDC Electric Power Development Co., Ltd

EPRI Electric Power Research Institute

FA Furnace Annealed
FIB Focused Ion Beam

GL Gauge Length

HAADF High Angle Annular Dark Field

HAGB High-Angle Grain Boundaries

HiperFer High Performance Ferrite

HR-FESEM High Resolution Field Emission Scanning Electron Microscopy

HS Head Section

HT High Temperature

LAGB Low-Angle Grain Boundaries

LIMS Liquid Metal Ion Sources

LT Low Temperature

MITI Ministry of International Trade

PAGB Prior Austenite Grain Boundaries

PFZ Particle-Free Zone

SE Secondary Electron

SEM Scanning Electron Microscope/Microscopy

SG Space Group

SOFC Solid Oxide Fuel Cell

STEM Scanning Transmission Electron Microscope/Microscopy

TC Thermocalc®

TEM Transmission Electron Microscope/Microscopy

USC Ultra-Supercritical

List of publications

Parts of the presented results in this work are related to the following articles and conferences:

- B. Kuhn, M. Talik, J. Lopez Barrilao, W. Chen, J. Ning; *Microstructure Evolution and Creep Properties of High Performance Ferritic (HiPerFer) steels at 600 °C, and 650 °C*; Proc.: 3rd International ECCC Conference; ECCC Creep and Fracture 2014; 5th-7th May 2014; Rome (Italy)
- J. Lopez Barrilao, M. Talik, B. Kuhn, E. Wessel; *Microstructure Evolution of High Temperature Fully Ferritic Steels*; Proc.: 1st International Conference on Advanced High-Temperature Materials Technology for Sustainable and Reliable Power Engineering (123 HiMAT-2015); 29th June-3rd July 2015, Sapporo (Japan); ISBN 978-4-9908874-0-7; pp. 15-18
- B. Kuhn, M. Talik, J. Lopez Barrilao, L. Singheiser; *Microstructure Stability of Ferritic-Martensitic, Austenitic and Fully Ferritic Steels Under Fluctuating Loading Conditions*; Proc.: 1st International Conference on Advanced High-Temperature Materials Technology for Sustainable and Reliable Power Engineering (123 HiMAT-2015); 29th June-3rd July 2015, Sapporo (Japan); ISBN 978-4-9908874-0-7; pp. 94-97
- J. Lopez Barrilao, B. Kuhn, E. Wessel, M. Talik; *Microstructure of Intermetallic Particle Strengthened High Chromium Fully Ferritic Steels*; Proc.: Parsons 2015: The 9th International Charles Parsons Turbine and Generator Conference; 15-17 September 2015, Loughborough (UK)
- B. Kuhn and M. Talík and J. Lopez Barrilao and L. Singheiser and Y. Yamamoto; Ferritische Hochleistungsstähle (HiperFer) Ein Entwicklungsstatus; 38. Vortragsveranstaltung zum "Langzeitverhalten warmfester Stähle und Hochtemperaturlegierungen"; Verein Deutscher Eisenhüttenleute; ; November 2015; Düsseldorf (Germany)
- J. Lopez Barrilao, B. Kuhn, E. Wessel, M. Talik; *Microstructure of Intermetallic Particle Strengthened High Chromium Fully Ferritic Steels*; Materials Science and Technology Special Issue Parsons 2015; 2016; http://dx.doi.org/10.1080/02670836.2016.1244039

- J. Lopez Barrilao, B. Kuhn, E. Wessel; *Microstructure and Intermetallic Particle Evolution in Fully Ferritic Steels*; Proc.: 8th International Conference on Advances in Materials Technology for Fossil Power Plants; 10th 14th October 2016; Albufeira (Portugal); pp. 1029-1037; ISBN-13: 978-1-62708-131-3
- B. Kuhn, M. Talík, J. Lopez Barrilao, L. Singheiser, Y. Yamamoto; *Development Status of High performance Ferritic (HiperFer) steels*; Proc.: 8th International Conference on Advances in Materials Technology for Fossil Power Plants; 10th 14th October 2016; Albufeira (Portugal); pp. 1019-1028; ISBN-13: 978-1-62708-131-3

Kurzfassung

Die vorliegende Arbeit befasst sich mit der mikrostrukturellen Untersuchung hochfester, hochchromhaltiger (18 - 23 wt.%), voll ferritischer Stähle, die eine neue Konzeptidee zur Anwendung in Energieumwandlungssystemen darstellen. Hierbei ist die Matrix bei jeder Temperatur unterhalb des Schmelzpunktes ferritisch und nicht das Ergebnis einer martensitischen Umwandlung. Technologische Grundlage dieser Stähle ist der Werkstoff Crofer[®] 22 H, welcher neben Crofer[®] 22 APU in Kooperation zwischen dem Institut für Werkstoffstruktur und -eigenschaften (IEK-2) des Forschungszentrums Jülich und VDM Metals GmbH entwickelt wurde. Beide Werkstoffe werden als Interkonnektormaterialien in Hochtemperaturbrennstoffzellen eingesetzt. Während der Entwicklungsphase dieser Stähle wurden mehr als 50 verschiedene Versuchslegierungen mit unterschiedlicher chemischer Zusammensetzung konzipiert. Aufgrund des hohen Chromgehaltes weisen diese Versuchslegierungen eine potentiell hohe Dampfoxidationsbeständigkeit bis hin zu Temperaturen von 650 °C auf [1], im Gegensatz zu den bisher eingesetzten ferritisch-martensitischen 9 - 12 %Cr Stählen, die nur bis etwa 620 °C eingesetzt werden können. Um eine Dampfoxidationsbeständigkeit ienseits von 620 °C zu gewährleisten, bedarf es eines höheren Chromgehaltes [2, 3]. Allerdings begünstigt eine Erhöhung des Chromgehaltes in 9 - 12 %Cr Stählen die Bildung der Z-Phase. Diese bildet sich auf Kosten der für die Steigerung der Kriechfestigkeit verantwortlichen MX (M = V, Nb; X = C, N) Ausscheidungen aus [4], was zu einer Verminderung der Langzeit-Kriechbeständigkeit führt.

Die Verfestigung der neuen ferritischen Materialen erfolgt durch Mischkristallhärtung, sowie zusätzlich im Falle von Crofer[®] 22 H durch Partikelhärtung mittels intermetallischer Laves Phasen der Form (Fe,Cr,Si)₂(Nb,W). Aufgrund dieser Verfestigungsmechanismen besitzen die 22 H Modelllegierungen im Temperaturbereich von 600 °C bis 650 °C ein vielversprechendes Kriechverhalten [1] und bieten dadurch eine mögliche Materialalternative für zukünftige Kraftwerksanwendungen. Die Hauptanforderungen dieser zukünftigen Kraftwerksanwendungen sind unter anderem ein flexiblerer Kraftwerksbetrieb, höherer Wirkungsgrad und somit ein geringerer CO₂ Ausstoß. Um den Optimierungsprozess dieser Legierungen weiter voran zu treiben, wurden im Rahmen dieser Arbeit drei unterschiedliche 22 H Modelllegierungen hinsichtlich Identifizierung der Laves Phasen und Größenklassifizierung im Temperaturbereich von 600°C bis 650 °C untersucht. Hierzu wurden die Einflüsse der chemischen Zusammensetzung auf die Ausbildung verschiedener Laves Phasen, sowie deren Größenentwicklung betrachtet. Die Untersuchungen erfolgten nach unterschiedlichen Alterungszeiten unter Verwendung von Raster- und Transmissionselektronenmikroskopie. Parallel dazu wurde die Eignung eines kommerziell verfügbaren thermodynamischen Modellierungsprogramms bewertet. Hierbei stellte sich eine unzureichende Genauigkeit der Modellierung für zukünftige Legierungsentwicklungen von voll ferritischen Werkstoffen heraus. Die Ergebnisse der Ausscheidungsentwicklung erklären das unterschiedliche Kriechverhalten der Versuchslegierungen und zeigen außerdem, dass die Ausscheidungen über den gesamten betrachteten Bereich (z.B. ca. 40,000 h bei 600 °C und ca. 10,000 h bei 650 °C) thermodynamisch stabil sind. Des Weiteren wurden ergänzende Untersuchungen zur Mikrostrukturentwicklung bei 650 °C durchgeführt. Diese Untersuchungen bezogen sich im Detail auf die Bildung von Subkornstrukturen und partikelfreien Zonen, sowie der Versetzungsdichte in diesen. Partikelfreie Zonen sind von besonderem Interesse, da sie ein vermuteter Hauptgrund für frühzeitiges Materialversagen aufgrund fehlender Partikelhärtung sind.

Abstract

The present investigation focuses on a new concept of high strength, high chromium (18 - 23 wt.%), fully ferritic steels on the technical basis of Crofer[®] 22 H for the application in high temperature energy conversion systems. Fully ferritic means, that these steels possess a ferritic matrix at any temperature below the melting point, i.e. no martensitic transformation occurs. During Crofer® 22 APU and Crofer® 22 H development, over 50 trial alloys with slight changes in chemical composition were designed. Both steels are used as interconnect materials for solid oxide fuel cells (SOFCs) and were developed by the Institute for Microstructure and Properties of Materials (IEK-2) at Forschungszentrum Jülich GmbH in cooperation with VDM Metals GmbH. Such steels possess potentially sufficient steam oxidation resistance up to 650 °C, because of their high chromium content [1]. In contrast the steam oxidation resistance of state of the art 9 - 12 %Cr advanced ferritic martensitic (AFM) steels is limited to temperatures of approximately 620 °C. To ensure sufficient steam oxidation resistance of AFM steels above 620 °C a higher chromium content is needed [2,3]. However, this promotes Z-phase formation on the expense of the strengthening MX (M = V, Nb; X = C, N) particles [4], what causes a drop in long-term creep strength.

Strengthening of the new fully ferritic steels is achieved by solid-solution hardening and in case of Crofer® 22 H by supplemental intermetallic (Fe,Cr,Si)₂(Nb,W) Laves phase particles. The 22 H trial alloys possess superior creep behaviour in the temperature range from 600 °C to 650 °C [1] and therefore may potentially provide a basis for tackling the future requirements of power plant operation, e.g. higher operational flexibility, higher conversion efficiency and thus lower CO_2 emission.

In order to further optimisation of these fully ferritic alloys the investigation was performed on three various 22 H trial alloys. The investigations aimed on the identification and classification of Laves phase particles as well as on the influence of chemical composition on the presence of different Laves phases and particle size evolution in the temperature range from 600 °C to 650 °C after different annealing time utilising electron microscopy techniques. Concurrently the suitability of a commercially available thermodynamic modelling tool was checked and rated as doubtful for further in detail alloy development of such ferritic steels. Particle evolution results explain the different creep behaviour of the trial alloys and show promising thermodynamic stability of particle over the whole covered time range (e.g. approximately 40,000 h at 600 °C and approximately 10,000 h at 650 °C). Furthermore, investigation of microstructure evolution at 650 °C focused on sub-grain formation, the formation of particle free zones and associated dislocation density in these. Due to missing particle strengthening in these zones and consequently a drop in creep strength, the particle free zones are suspected to be a reason of premature material failure.

Contents

1	Intr	oduction
	1.1	Background and Motivation
	1.2	Outline
2	Scie	entific Background
	2.1	State of the art 9-12% Cr steels
	2.2	Crofer® 22 APU and Crofer® 22 H
	2.3	Strengthening Particles
		2.3.1 Carbide and Nitride
		2.3.2 Laves Phase
		2.3.3 σ-Phase
		2.3.4 Z-Phase
	2.4	Crystallographic Defects
		2.4.1 0-dimensional Lattice Defects
		2.4.2 1-dimensional Lattice Defects
		2.4.3 2-dimensional Lattice Defects
	2.5	Ageing Processes in Solids
		2.5.1 Diffusion
		2.5.2 Precipitation
		2.5.3 Structural Ageing
	2.6	Phase Diagrams
	2.7	Mechanical Properties
	2.8	Transmission Electron Microscopy (TEM)
		2.8.1 Fundamental Principles
		2.8.2 Architecture

		2.8.3	Imaging	. 32			
		2.8.4	General Sample Preparation	. 34			
	2.9	Scann	ing Electron Microscopy (SEM)	. 37			
3	Exp	erime	ntal	39			
	3.1	Mater	ials and Production	. 39			
	3.2	Annea	ding Experiments and Sample Preparation	. 39			
	3.3	Micros	structural Analysis	. 41			
		3.3.1	HR-FESEM and Image Analysis	. 41			
		3.3.2	STEM	. 44			
	3.4	Therm	nodynamic Modelling of Phase Diagrams	. 44			
4	Res	ults ar	nd Discussion	45			
	4.1	Previo	ous Studies	. 45			
	4.2	Selecti	ion of Sample Preparation	. 47			
	4.3	3 Thermodynamic Modelling and Verification by Electron Microscopy Ex-					
		amina	tion	. 48			
		4.3.1	Thermodynamic Modelling	. 48			
		4.3.2	STEM Examination at 600 °C and 650 °C	. 50			
		4.3.3	Chemical Composition at 600 °C and 650 °C $\dots \dots$. 60			
		4.3.4	Examination of Phase Structure	. 70			
	4.4	Partic	le Evolution at 600 °C and 650 °C	. 73			
		4.4.1	Particle Diameter Evolution	. 76			
		4.4.2	Evolution of Particle Size Distribution	. 77			
	4.5	Summ	ary and Conclusion:				
		Partic	le Verification and Evolution	. 86			
	4.6	Micros	structure Evolution at 650 °C	. 87			
		4.6.1	Sub-Grain Structure Evolution	. 87			
		4.6.2	Particle-Free Zone Evolution	. 87			
	4.7	Summ	ary and Conclusion:				
		Micros	structure Evolution	. 98			
5	Ove	erall Co	onclusion and Outlook	101			

A Appendix:										
Thermodynamic Modelling	Thermodynamic Modelling									
and Verification by Electron										
Microscopy Examination	103									
A.1 STEM Examination at 600 °C and 650 °C \hdots	103									
A.2 Phase Distinction	105									
A.2.1 EDX measurement	105									
A.2.2 Diffraction measurement	107									
B Particle Evolution	109									
C Microstructure Evolution	111									
C.1 Particle-Free Zone Evolution	111									
Bibliography	115									
List of Figures										
List of Tables										

1 Introduction

1.1 Background and Motivation

Demographic growth and technical progress of modern societies result in an increase of energy consumption. A comparison of global energy consumption in 1990 and 2011 shows an increase by 50%, whereby 80% was covered by fossil fuels [5]. The power generation to meet the demand of the continuous increasing trend of the global energy consumption are predicted in several scenarios. The forecasts of electricity generation by energy source commissioned by the German Federal Ministry of Economics and Technology considering the German "Energiewende" or the U.S. Department of Energy are given in Figure 1.1. Contents of German "Energiewende" are for example the turn away from nuclear energy technology until year 2022 and an increase of renewables to 80% of the gross electricity production until year 2050. The latter results in a more flexible operation mode of thermal power plants (flexible start up and shut down periods) with longer downtimes to ensure the supply of electricity [6]. Therefore the forecasts contain different political decisions and trends. The forecast commissioned by the German Federal Ministry of Economics and Technology "presents probable future energy industry developments as well as [...] further stringent energy and climate protection policies and existing obstacles to their implementation" [5] and "assume[s] the advancing integration of the global economy during the observation time frame 2011-2050" [5]. While the U.S. Department of Energy forecast "is a business-as-usual trend estimate, given known technology and technological and demographic trends" [7]. But regardless of the appropriated trend data both forecasts still predict fossil fuels as one main source for electricity generation in the future. For this reason a strong demand for more efficient, sustainable and flexible energy technologies and materials in steam power plants is needed.

Materials currently used in power plants are 9-12% Cr advanced ferritic-martensitic (AFM) steels, which were developed for advanced cycle power plants under ultrasupercritical (USC) steam conditions. However the oxidation resistance of state of the art 9-12% Cr AFM steels is limited to temperatures up to 620 °C. Beyond 620 °C higher chromium contents are necessary to guarantee adequate steam oxidation resistance [2,3], but this is accompanied by undesirable phase formation on the expense of material strength [4].

For that reason improvements are necessary to decrease CO₂ emissions and to increase

the efficiency of power plants. An improvement of power plant efficiency means an increase of the process parameters and therefore a reduction of needed primary resources. Fulfilment of national and international requirements in the future necessitates the advancement of known materials or the development of new materials.

(a)

(b)

Figure 1.1: (a) Gross electricity generation by energy source in Germany (2011-2050, in kWh) [5]. (b) World net electricity generation by energy source (2012-2040, in 10¹² kWh) [7].

1.2 Outline

A new approach for the application in high temperature energy conversion systems are high strength fully ferritic steels. The Institute for Microstructure and Properties of Materials (IEK-2) at Forschungszentrum Jülich GmbH developed a fully ferritic steel strengthened by a combination of solid solution and intermetallic Laves phase strengthening on the technological basis of Crofer® 22 H [1], a successor of Crofer® APU. Both materials were designed originally as interconnect materials for solid oxide fuel cells (SOFCs) in cooperation with and commercially produced by VDM Metals GmbH under license of Forschungszentrum Jülich GmbH. Due to the high chromium content the fully ferritic trial steels from Crofer® 22 H development possess superior creep behaviour and sufficient steam oxidation resistance in the temperature range from 600 °C to 650 °C [1].

Within the framework of Crofer® APU and Crofer® 22 H development more than 50 trial alloys were designed. These trial alloys featured chromium contents of 18 - 23 wt.%. Further development of the trial alloys resulted in the novel HiperFer steels (**High Per**formance **Fer**rite), a new generation of fully ferritic steels with a chromium content of 17 wt.% [8,9].

This work focuses on the identification, size classification and evolution as well as indepth analyses of chemical compositions and lattice structures of the strengthening Laves phase particles. Therefore three different trial alloys from Crofer® 22 H development were analysed after annealing at 600 °C and 650 °C for different times. For the size evolution of particles, HR-SEM images were analysed. The results were associated with the different creep performance of the trial alloys. Investigation of chemical compositions and lattice structures were performed by means of TEM/EDX measurements. Concurrently the commercial software Thermocalc® was evaluated for suitability by comparison to chemical compositions of particles and reliability of phase prediction. Additionally microstructural characterisation of the most creep resistant trial alloy 2.5W0.57Nb0Ti from Crofer® 22 H development was performed after annealing and creep at 650 °C concerning grain, sub-grain and dislocation density evolution and to provide information about potential phenomena, which are suspected to have significant influence on creep damage and failure.

The studies and results obtained in this work will help to increase the accuracy of optimised databases for thermodynamic modelling of ferritic high performance steels, which is an essential requirement for goal oriented alloy optimization. Furthermore the characterisation of phases and the investigation of microstructural evolution provides important information to understand underlying damage mechanisms and therefore contribute to further development/optimisation of HiperFer steels.

2 Scientific Background

2.1 State of the art 9-12% Cr steels

Materials widely used in current power plants are 9-12% Cr advanced ferritic-martensitic (AFM) steels with a tempered martensitic structure [10,11]. The development of these steels was motivated by two main reasons: First, the development of steam power plants in the temperature range from 538 °C to 566 °C in the 1950's and second, the requirement of environmental pollution reduction by increasing the steam temperature in the 1980's [12].

AFM steels were developed for advanced cycle power plants with ultra-supercritical (USC) steam conditions (31 MPa, 566 °C and above) to increase efficiency [13,14], e.g. an increase from 538 °C, 18.5 MPa to 593 °C, 30 MPa result in an increase of 6% in efficiency, to 650 °C even by up to 8% [14]. Research and development have progressed in several projects in Europe, Japan and the USA. Figure 2.1 gives an overview about the these projects. In Europe the research started in 1983 with the first Cooperation in Science and Technology (COST) project. The Japanese research was initiated by the Ministry of International Trade and Industry (MITI), was performed by the Electric Power Development Co., Ltd (EPDC) and started in year 1981. Basic studies in the US started in 1978 and were conducted by the Electric Power Research Institute (EPRI) [13].

Figure 2.1: International research projects on AFM steels [13].

The development of ferritic-martensitic steels for boilers with their proposed 10⁵ h creep rupture strength at 600 °C is given in figure 2.2 along with the associated nominal chemical compositions in figure 2.3. Developments were mainly aimed at thick section pipes and headers [14] and to decrease material costs [13]. 9-12% Cr steels with a 10⁵ h rupture strength of 40 MPa (600 °C) were used over a long period. The first generation of materials for the use at 60 MPa was motivated to provide an alternative to the austenitic 18%Cr-8%Ni steels and were developed between 1960-1970. Advanced creep rupture strength was achieved in the 1980s (100 MPa, second generation) and in the 1990s (140 MPa, third generation). The use at 100 MPa in case of T/P91 as well as the use of T/P92 at 140 MPa for the third generation was corrected to approx. 80 MPa or rather 112 MPa in the year 2005 [15]. The 180 MPa generation was "expected to emerge" [13] in 2000.

Figure 2.2: Development of ferritic-martensitic steels for boilers with 10⁵ h rupture strength at 600 °C [13] like expected in year 2000.

Figure 2.3: Nominal chemical composition of AFM steels for boilers [13].

The best-known representatives of 9%Cr AFM steels are T/P91 and T/P92 for the use at 593 °C in case of T/P91 and at temperatures up to 620 °C in case of T/P92 with

the highest allowable stress reported by Viswanathan and Bakker [14]. Beyond 620 °C these steels are limited by oxidation resistance. An increase in chromium content to 12 wt.% leads to a sufficient oxidation resistance up to 620 °C, e.g. HCM12A (P-122), which is used for headers and piping up to 620 °C [14].

The high creep strength of AFM steels is mainly obtained on the one hand by MX (M = Nb, V; X = C, N) and partly by $M_{23}C_6$ (M = Cr) particle hardening. Whereby the MX particles precipitate within grains as well as on sub-grain boundaries (lath boundaries) and preferentially $M_{23}C_6$ on prior austenite grain boundaries (PAGBs). On the other hand the steels are strengthened by solid-solution hardening with solute atoms like W and Mo [11, 14, 16] (cf. section 2.3.1). Besides MX and $M_{23}C_6$ particles Laves phase particles occur in these steels. The use for material strengthening by this particle class is certainly controversial [17, 18] (cf. section 2.3.2).

For improved resistance to steam oxidation at temperatures above 620 °C a higher chromium content is mandatory [2,3]. However this benefits the formation of the Z-phase, a complex nitride on the expense of strengthening MX particles, and thus a breakdown in long-term creep strength [4] (cf. section 2.3.4).

2.2 Crofer® 22 APU and Crofer® 22 H

The fully ferritic steels Crofer® 22 APU (Auxiliary Power Unit) and the advanced Crofer® 22 H are commercially available from VDM Metals GmbH. Both steels were developed in cooperation with the Institute of Energy and Climate Research (IEK), Microstructure and Properties of Materials (IEK-2) at Forschungszentrum Jülich GmbH. The chemical composition of Crofer® 22 APU (1.4760) and Crofer® 22 H (1.4755) is given in tables 2.1 and 2.2.

Table 2.1: Chemical composition of Crofer® 22 APU in wt.% [19].

		Cr	Fe	C	Mn	Si	Cu	Al	\mathbf{S}	P	Ti	La
mir	ı.	20.0	R		0.3						0.03	0.04
max	х.	24.0	R	0.03	0.8	0.5	0.5	0.5	0.02	0.05	0.2	0.2

Table 2.2: Chemical composition of Crofer® 22 H in wt.% [20].

	\mathbf{Cr}	Fe	\mathbf{C}	Mn	Si	Cu	Al	S	P	Ti	La
min.	20.0	R			0.1					0.02	0.04
max.	24.0	R	0.03	0.8	0.6	0.5	0.1	0.006	0.05	0.20	0.20

	N	Ni	Nb	W
min.			0.2	1.0
max.	0.04	0.5	1.0	3.0

Both steels were designed as an interconnect material for solid oxide fuel cells (SOFCs) and operation temperatures of up to 900 °C and are characterized by an excellent corrosion resistance due to the high chromium content, but a low rate of chromium vaporization. Additionally these steels feature a low coefficient of thermal expansion $(12.7 \cdot 10^{-6} \frac{1}{K} [19] \text{ in case of Crofer}^{\otimes} 22 \text{ APU}$ and $12.8 \cdot 10^{-6} \frac{1}{K} [20] \text{ for Crofer}^{\otimes} 22 \text{ H}$, temperature range between 20 °C and 1000 °C) and good electrical conductivity of the formed surface oxide layer (fine grained Cr_2O_2 inner scale and columnar $\text{Mn}, \text{Cr}_3\text{O}_4$ spinel outer layer). The steels are strengthened by solid solution hardening (tensile strength $\text{R}_{\text{m}} \geq 350 \text{ MPa}$ for $\text{Crofer}^{\otimes} 22 \text{ APU}$ and $\text{R}_{\text{m}} = 450 \text{ MPa}$ in case of $\text{Crofer}^{\otimes} 22 \text{ H}$, ambient temperature) [19,20]. The increase in strength in case of $\text{Crofer}^{\otimes} 22 \text{ H}$ results from additional particle hardening. Due to the combined addition of tungsten, niobium and silicon the formation of Laves phase particles is triggered [21,22].

Besides the properties of these steels for the application as SOFC component, the trial alloys designed within the framework of Crofer® 22 H development show promising steam oxidation and creep behaviour in the temperature range from 600 °C to 650 °C, which makes this material also interesting for applications in power plants [1]. These promising properties at temperatures from 600 °C to 650 °C require specific investigation with regard to particle formation and stability and are part of this work.

2.3 Strengthening Particles

Besides solid solution hardening, where foreign atoms are fully dissolved in the matrix, targeted implementation of second phase particles can as well increase the strength of a material. The reason is that particles serve as obstacles for dislocation movement and/or grain boundary sliding, if the particles are located on grain boundaries (cf. section 2.5.3) and thus plastic deformation can be impeded. However also an opposite effect can be achieved by the formation of undesired particles (e.g. Z-phase formation in 12% Cr AFM steels).

2.3.1 Carbide and Nitride

The compounds of Carbon (C) and Nitrogen (N) with elements of lower electronegativity are called carbide or rather nitride. In metals the bonding occurs mainly with transition metals like chromium, tungsten, vanadium, titanium, niobium, tantalum, manganese or zirconium and form non-stoichiometric compounds. More precisely carbon or nitrogen diffuses to an interstitial in the metal lattice and forms strong compounds suitable for technical use, e.g. TiC, TiN or in martensitic steels (Nb,V)(C,N) [16]. The structure of these examples is the cubic NaCl structure (cf. figure 2.4a and b), space group Fm3m (No. 225) [23]. Besides the cubic structure the compounds can also appear in hexagonal close packed or orthorhombic lattice structures. An overview of carbide structures is given in [24]. The formation of carbide with chromium represents a special case. This element mainly forms $Cr_{23}C_6$ or more general $M_{23}C_6$ particles. The

structure of this carbide is cubic, too (cf. figure 2.4c), SG: Fm3m, No. 225 [25]). In 9-12% Cr steels carbides and nitrides rich in vanadium and niobium as well as $M_{23}C_6$ rich in chromium ensure the strength of the material [11, 14, 16, 26] (cf. section 2.1).

(a) (b)

(c)

Figure 2.4: Lattice structure of (a) TiC, (b) TiN [27] and (c) $Cr_{23}C_6$ [28].

2.3.2 Laves Phase

Laves phases are intermetallic phases which are formed preferentially by the connection of alkali and/or alkaline earth metals with transition metals. The lattice structure is AB₂ whereby the atom radius of element A is larger than the radius of element B and therefore the formation of a solid solution is not possible. For Laves phases the ideal radius ratio is given by $\frac{r_A}{r_B} = 1.22$. The lattice structure of Laves phases can be distinguished in three types depending on

The lattice structure of Laves phases can be distinguished in three types depending on the stacking order: the hexagonal C14 and C36 (space group (SG) P63mmc [29]; No. 194) and the cubic C15 structure (SG: Fd3m [29]; No 227). The most popular examples for these structures are the MgZn₂ (C14), MgCu₂ (C15) and MgNi₂ (C36) [30,31] Laves phases. Figure 2.5 shows the stacking orders of the different Laves phase types. The use of Laves phases for strengthening in 9-12 % Cr martensitic steels is controver-

sial. The impact of Laves phase formation and coarsening [32,33] on creep strength was in the focus of several studies, but is not yet fully understood. Early studies [17,34,35] report a decrease in creep strength due to a reduction of solid-solution hardening. This reduction was proposed to be caused by the formation of Laves phases and thus the depletion of Mo and W from the matrix. This is not confirmed by other studies, where the formation of $(\text{Fe,Cr})_2(\text{Mo,W})$ Laves phases was proposed to increase the creep strength by precipitation hardening under certain conditions [16, 18, 36].

In case of fully ferritic steels based on $\operatorname{Crofer}^{\otimes}$ 22 H (cf. section 2.2) the utilisation for strengthening by means of $(\operatorname{Fe,Cr,Si})_2(\operatorname{Nb,W})$ Laves phase particles is clear. The phases increase the creep strength significantly [1,22] and are stable during service [37].

Figure 2.5: Examples for Laves phase structure types and stacking order: $MgZn_2$ (C14), $MgCu_2$ (C15) and $MgNi_2$ (C36). Open circles: Mg atom, full dots: smaller atom (here: Zn, Cu, Ni) [38].

2.3.3 σ -Phase

The σ -phase is an intermetallic phase with potentially harmful effect on creep strength in case of precipitation on grain boundaries and occurs in Fe-Cr systems [25]. Due to its high Cr content the σ -phase reduces corrosion resistance [39–41]. The reduction is caused by chromium depletion in the zones around the σ -phase, which results in preferential areas for pitting corrosion [39, 42]. However, prevention of this phase is difficult in stainless steels with a Cr contents above 20 wt.%. The formation is caused by diffusion of chromium, molybdenum or silicon, which are strong ferrite stabilizers, in δ -ferrite [39]. In pure Fe-Cr alloys the formation of the σ -phase starts at a Cr content of 15 wt.% below 800 °C (cf. figure 2.6). Besides chromium, molybdenum or silicon the

formation can also be promoted by niobium, titanium and vanadium, but is aggravated by nickel or cobalt [43]. Formation of the σ -phase is in many cases accompanied by the formation of χ -phase [25, 39], a cubic phase, with as well harmful effects on corrosion resistance [44]. The tetragonal structure (SG: P4₂/mnm, No. 136 [25, 40]) of the σ -phase is depicted in figure 2.7.

Figure 2.6: Equilibrium diagram of the Fe-Cr-system [43] (based on [45]).

Figure 2.7: Tetragonal lattice structure of σ -phase [46].

2.3.4 **Z-Phase**

The Z-phase is a tetragonal complex nitride of the original form CrNbN (first observation in the 1950s) or the modified form ${\rm Cr_2(V,Nb)_2N_2}$ [47] and precipitates preferably around prior austenite grain boundaries in 9-12% Cr martensitic steels [48]. In martensitic steels with Cr contents above 8 wt.% the formation of this nitride is validated [4]. Z-phase formation depends on the chromium content of the alloy. In steels with chromium contents of 11-12 wt.% the formation of the phase is faster than in alloys with 9 wt.% of chromium [4, 47, 49]. The consuption of Nb and V by the Z-phase, on the

expense of strengthening MX particles, is made responsible for a breakdown in long-term creep strength [49] (cf. section 2.1 and 2.3.1). Thus newer research focuses on the utilization of the Z-phase for strengthening of 12%Cr martensitic steel [50, 51]. The lattice structures of the original or modified Z-phase is given in figure 2.8.

Figure 2.8: Tetragonal lattice structure of Z-phase [4, 52].

2.4 Crystallographic Defects

The structure of real crystals is never free of defects. These defects can be distinguished in different types. Point defects (0-dimensional lattice defects), dislocations (1-dimensional lattice defects) as well as grain and phase boundaries (2-dimensional lattice defects). The formation of phases (3-dimensional lattice defects) is a special feature. However, this formation is part of thermal equilibrium so that the actual defect is a 2-dimensional defect of a phase boundary. Thus these defects can be subordinated to the 2-dimensional defects. Due to the presence of defects a crystal can not reach an ideal thermodynamic equilibrium but an energetically favourable condition. Paradoxically these defects ensure the properties of metals as structural materials, e.g. diffusion for phase formation requires vacancies, plastic deformation or recrystallisation implies generation and movement of dislocations or grain boundaries.

2.4.1 0-dimensional Lattice Defects

Point defects can be distinguished into two types. On the one hand vacant lattice spaces (vacancy defects, cf. figure 2.9a) and on the other hand the occupancy of interstitial lattice spaces (interstitial defects, cf. figure 2.9b).

Literature used in section 2.3: [43,53–57]

In metals vacancy defects can occur individually in appreciable concentration (cf. equation 2.1). On this occasion an atom close to the surface moves to the surface and leaves a vacancy behind which can move to the crystal interior. In case of atom movement from a lattice space to an interstitial lattice space a defect pair appears (cf. figure 2.9c). This pair is a so called Frenkel defect or Frenkel pair. In ionic crystals vacancy defects cannot occur individually in order to maintain charge neutrality. Here only Frenkel pairs or Schottky defects appear. A Schottky defect describes vacancy pairs (anion and cation vacancies, cf. figure 2.9d). Additionally the arrangement of impurity atoms in the lattice assigned to point defects is not unusual in alloys (cf. figure 2.9e and f). All types of defects cause slight deformation of the crystal lattice.

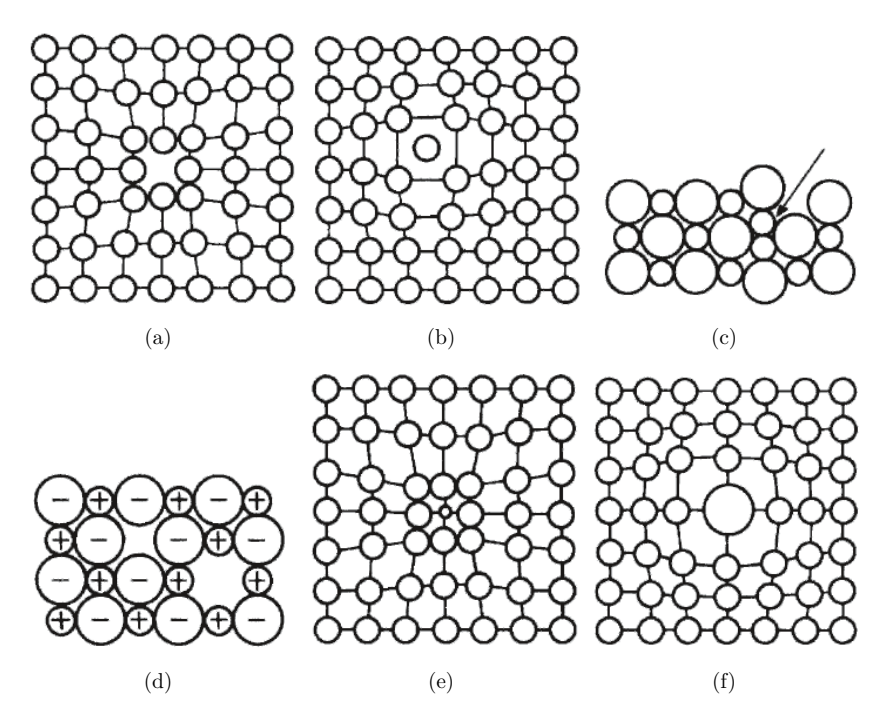


Figure 2.9: Overview of point defects: (a) vacancy defect, (b) interstitial defect, (c) Frenkel pair, (d) Schottky defect, (e) small impurity atom, (f) large impurity atom [58].

In consideration of the laws of thermodynamics the concentration of point defects can be determined.

The following applies for the calculations of the concentration c_L^a of vacancy defects in metals:

$$c_L^a = \exp\left(\frac{S_v^L}{k}\right) \exp\left(-\frac{H_B^L}{kT}\right) \tag{2.1}$$

 S_v^L describes oscillation entropy, $k\approx 1.38\cdot 10^{-23}~\frac{J}{K}$ is the Boltzmann constant, H_B^L describes the enthalpy of formation and T is the temperature. Independent of the material the concentration c_L^a of vacancy defects is in the magnitude of 10^{-4} and basically depends on enthalpy of formation.

2.4.2 1-dimensional Lattice Defects

Defects along a line are called dislocations and can be distinguish in edge dislocations and screw dislocations. The difference between these types is the displacement along a slip plane. In case of an edge dislocation the lattice is dislocated perpendicular to the slip plane (cf. figure 2.10a). This results in additional atomic layers depending on the size of displacement (cf. figure 2.10b). In case of screw dislocations the lattice is dislocated parallel to the slip plane so that a helical arrangement of different lattice planes arises (cf. figure 2.11a and b).



Figure 2.10: (a) Edge dislocation EF in a slip plane ABCD caused by perpendicular displacement regarding to the slip plane [59]. (b) Structure of an edge dislocation with additional atomic layer (red atoms) [58].

(a) (b)

Figure 2.11: (a) Screw dislocation. The part ABEF of the slip plane ABCD is parallelly dislocated [59]. (b) Top view of the screw dislocation [59].

Dislocations are characterised by the line element \vec{s} and the Burgers vector \vec{b} . The line element is the unit vector tangential to the dislocation line and is location-dependent in case of a combination of both dislocation types. An example for a combined dislocation is given in figure 2.12. The Burgers vector is defined due to the Burgers circulation. Figure 2.13 shows the determination of the Burgers vector for an edge dislocation (cf. figure 2.13a) and a screw dislocation (cf. figure 2.13b). A closed clockwise circulation in a disordered crystal is marked. In this case starting point and terminus are in the same place. The same closed clockwise circulation is marked in an ideal crystal. In this case starting point and terminus are not at the same position. The differences between the circulation in a disordered and the ideal crystal is the so-called Burgers vector. The Burgers vector and the dislocation line are perpendicular in case of an edge dislocation and parallel in case of a screw dislocation.

Figure 2.12: Combined dislocation and location-dependent dislocation line [58].

(a)

(b)

Figure 2.13: Circulation in a disordered crystal (left) and circulation of the same size in an ideal crystal with Burgers vector (right) for (a) an edge dislocation and (b) a screw dislocation. [60].

Plastic deformation causes movement of dislocations. The movement occurs along the slip plane if the movement is not stopped by e.g. particles. Screw dislocations do not have a defined slip plane and can change the slip plane by cross-slipping. In contrast to that edge dislocations have a defined slip plane and are able to leave them due to the accumulation of vacancy defects. The movement process will be discussed in more detail in section 2.5.

2.4.3 2-dimensional Lattice Defects

Grain boundaries are planar defects and identify the boundary between two crystal areas with the same structure but different orientation. Boundaries between two areas with small orientation differences are called low-angle grain boundaries (LAGBs), areas with high difference in orientation are called high-angle grain boundaries (HAGBs). LAGBs are formed by dislocations and are distinguished in symmetric and antisymmetric tilt boundaries.

Symmetric tilt boundaries are formed by a unique band of edge dislocations with Burgers vector \vec{b} . Figure 2.14a shows a schematic illustration of a symmetric tilt boundary. The distance d of the dislocation depends on the tilt angle Θ (cf. figure 2.14b). For antisymmetric tilt boundaries at least two bands of screw dislocations are necessary with the Burgers vectors perpendicular to each other (cf. figure 2.14c). The following applies for the dependence of the dislocation distance:

$$\frac{|b|}{d} = 2\sin\left(\frac{\Theta}{2}\right) \approx \Theta \tag{2.2}$$



(c)

Figure 2.14: (a) Schematic illustration of a symmetric tilt boundary [58]. (b) Dependence of dislocation distance on tilt angle between grains [58]. (c) Schematic illustration of an antisymmetric tilt boundary [58].

The classification in LAGB and HAGB follows the size of the tilt angle Θ (cf. equation 2.2). For $\Theta < 15^{\circ}$ the boundaries are LAGB, which is validated due to the specific energy of grain boundaries. In case of $\Theta > 15^{\circ}$ the energy remains constant. Thus grain boundaries with an angle $> 15^{\circ}$ are classified as HAGB.

In case of HAGBs the orientation differences between two grains are larger than in case of LAGBs. Figure 2.15 shows schematically the deformation of the lattice in the area of a HAGB which results in an increase of the grain boundary energy. This increase can be reduced due to grain growth. The influence of an additional driving force results in a displacement of the grain boundary and thus replacement of atoms from one grain to another grain. Sufficient temperatures influence as well the growth whereby grains with low dislocation density grow at the expense of grains with a higher dislocation density. Additionally the deformation provides the accumulation of impurity atoms or precipitations and increases the diffusion rate at the boundary.

Figure 2.15: Schematic illustration of lattice deformation at a HAGB [61].

Boundaries between areas of different orientation, lattice structure and chemical composition are called phase boundaries. These boundaries are distinguished in coherent, semi coherent and incoherent. In case of a coherent boundary the lattice structures of both areas are acclimatized (cf. figure 2.16 a). If the adaptation of both areas is achieved by dislocations in a sufficient distance the boundary is semi coherent (cf. figure 2.16b). In case of no adaptation of the lattice structures the boundary is incoherent (cf. figure 2.16c). Differences in the lattice structures are always energetically unfavourable, but cannot always be prevented. An example of a coherent boundary in several metals is the twin boundary (cf. figure 2.16d). In this case the lattices of both grains are mirrored at the boundary.

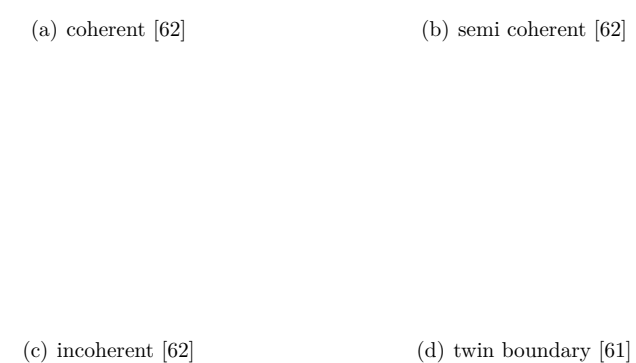


Figure 2.16: Different types of phase boundaries.

Stacking faults are additional 2-dimensional lattice defects. The lattice structure is built by a specific order of lattice planes, e.g. in case of a cubic close-packed structure the order is ABCABC. If the order is disrupted as in ABCAC the stacking fault lies between the 4th and 5th plane (cf. figure 2.17). The defects generate additional energy, which is called stacking fault energy, compared to thermal equilibrium. This energy depends on the area of the stacking fault.

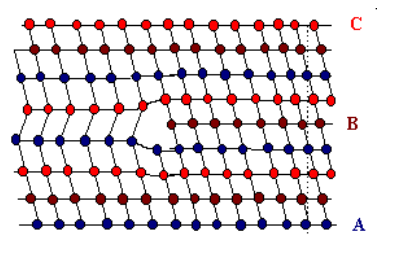


Figure 2.17: Stacking fault of a cubic close-packed structure with structure order ABCABC [63].

Literature used in section 2.4: [58,59,61]

2.5 Ageing Processes in Solids

Ageing processes include all time-dependent changes in microstructure and particle development during external influences like temperature and/or mechanical stress. Thus these processes can be thermally and/or mechanically activated and induce different mechanisms.

2.5.1 Diffusion

Diffusion is a thermally activated process and an essential mechanism for changes in solids. It is essentially connected with lattice defects like dislocations and grain boundary areas and describes the change in position of e.g. vacancies, impurity atoms and alloying elements.

The diffusion constant D is defined due to the 1st Fick's law:

$$J = -D\frac{dc}{dx} \tag{2.3}$$

J describes the matter flux or more precisely the number of atoms which pass a unit area per time unit and the term $\frac{dc}{dx}$ is the concentration gradient. The minus sign indicates the direction of diffusion flow, which is directed from areas of high to areas of low concentration.

The temperature dependence of D can be described as follows:

$$D = D_0 \exp\left(\frac{Q}{kT}\right) \tag{2.4}$$

 D_0 is a time-independent, but material-dependent factor. Q is the activation energy and depends on the type of diffusion (lattice and particle type) and the melting point.

2.5.2 Precipitation

Nucleation

The nucleation of particles and/or phases is subject to specific conditions. For successful nucleation the change in total free enthalpy ΔG_{total} has to be negative. ΔG_{total} is given by the following equation:

$$\Delta G_{total} = \Delta G_V + \Delta G_{Ph} + \Delta G_m + \Delta G_{Def}$$
 (2.5)

 ΔG_V is called free volume enthalpy and is the key driver for the nucleation process, because this term considers the oversaturation in solid solutions. Increasing oversaturation affects the decrease of ΔG_V .

 ΔG_{Ph} is the free enthalpy of the phase boundary between precipitate and matrix. This term is always positive and depends on lattice structure similarities. Coherent phase boundaries are energetically more favourable than incoherent (cf. section 2.4).

 ΔG_m defines the free lattice deformation enthalpy. In real crystals the boundaries between precipitate and matrix always involve deformation. Thus ΔG_m considers the mechanical energy of the atoms regarding the displacement from the neutral position. This term is always positive.

 ΔG_{Def} is a negative term and describes the saving of free enthalpy due to nucleation at lattice defects. This term as well gives the difference between ideal homogeneous nucleation and real heterogeneous nucleation. Homogeneous particles nucleate at random positions, while heterogeneous particles use the deformation of defects for an energetically favourable position.

The evolution of enthalpy regarding the precipitate radius r is given in figure 2.18.

Figure 2.18: Changes of free enthalpy regarding to the precipitation radius r of globular particles [64].

Figure 2.18 shows the critical radius r^* and free activation enthalpy ΔG^* . Above these values the nucleation of stable particles is possible.

Ostwald Ripening

Coarsening of big particles at the expense of smaller particles is called Ostwald ripening. The reasons for this are on the one hand the formation of a diffusion gradient, which promotes diffusion. In the area around small particles the concentration of dissolved elements is higher than around bigger particles, whereby the atoms diffuse from the smaller to the bigger particles. In this case the slowest element is decisive for the speed of diffusion. On the other hand the total free enthalpy of the phase boundary between precipitate and matrix is minimized in case of bigger particles.

The law for diffusion controlled particle coarsening in fluids [65,66] is also valid in metals. The following applies for globular particles without considering elastic deformation:

$$r_T^3 - r_{T_0}^3 = k_c \cdot t \tag{2.6}$$

 $r_{T_0}^3$ is the initial mean particle radius, r_T^3 is the mean particle radius after time t and $k_c \sim D\gamma_{Ph}c_0$ describes the coarsening constant.

The coarsening constant depends on the diffusion constant D, the specific enthalpy of the phase boundary between precipitate and matrix γ_{Ph} , as mentioned before, and the saturation concentration c_0 . In this case coarsening can be reduced by elements with low solubility.

2.5.3 Structural Ageing

Dislocation Movement

As mentioned in section 2.4.2 dislocations are able to move along slip planes. For the movement a force/shear stress is needed to overcome the lattice friction. Figure 2.19 shows the movement of a dislocation induced by shear stress. The minimum shear stress, which is needed for the movement, is the so-called Peierls-Nabarro stress τ_P and is defined as follows:

$$\tau_P = \frac{2G}{(1-\nu)} \exp\left(-\frac{2\pi}{(1-\nu)} \frac{d_s}{|\vec{b}|}\right) \tag{2.7}$$

G is the shear modulus, d_s defines the distance between the slip planes and ν is the Poisson's ratio (ratio of the modulus of elasticity E and the shear modulus G).

Figure 2.19: Schematic illustration of dislocation movement under the influence of a shear stress, which moves the crystal rightwards [59].

The movement or sliding of dislocations is preferred along close-packed planes, because in this planes the Peierls-Nabarro stress is lower than in other slip planes.

Dislocations possess fields of tension which can interact with other fields of tension of other dislocations. The interaction of two dislocations is described by the Peach-Koehler equation:

$$\vec{K}_{12} = \left(\vec{\sigma}_1 \vec{b}_2\right) \times \vec{s}_2 \tag{2.8}$$

 \vec{K}_{12} is the force, that dislocation 1 exerts on dislocation 2, $\vec{\sigma}_1$ describes the field of tension of dislocation 1, \vec{b}_2 and \vec{s}_2 are the Burgers vector and line element of dislocation 2.

Due to the movement on different slip planes an intersection of dislocations is possible and thus the formation of kinks (cf. figure 2.20). Kinks in the slip plane can be resolved by further sliding of the dislocation (cf. figure 2.20a). In case of kinks beyond the slip plane and further movement dislocation dipoles remain (cf. figure 2.20b and c).

Intersection of dislocations is not always the result of the convergence of dislocations. In case of antiparallel dislocations the movement results in annihilation of these dislocations (cf. figure 2.21a). The arrangement of parallel dislocations is the reason for the formation of LAGBs and thus a sub-grain structure (cf. figure 2.21b).

(a)

(b) (c)

Figure 2.20: Formation of kinks during intersection of dislocations (a) in the slip plane and (b) beyond the slip plane with (c) remaining dipole [58].

(a)

(b)

Figure 2.21: Example of dislocation movement: (a) Annihilation of dislocations and (b) sub-grain formation [67].

The probability for annihilation and the formation of LAGBs increases if dislocations leave their main slip plane. Change of planes occurs e.g. if dislocations avoid obstacles like particles. In case of screw dislocations this can be reached due to cross-slipping. Screw dislocations do not have a defined slip plane and thus the movement along parallel slip planes, where the direction of the Burgers vector does not change, is possible. The mechanism of slip plane change in case of edge dislocations is called dislocation climb. Edge dislocations have defined slip planes. Due to the accumulation of impurity atoms (negative climb) or vacancies (positive climb) at the dislocation line the edge dislocation can change the slip plane. This mechanism is diffusion controlled and proceeds continuously at higher temperatures (cf. equation 2.1 and 2.3).

If dislocations cannot avoid an obstacle the dislocation has two possibilities, cutting the obstacle (Friedel effect) or bypassing it (Orowan mechanism). Figure 2.22 shows both mechanisms schematically.



Figure 2.22: (a) Cutting of a particle (Friedel effect) and (b) bypassing of the particle (Orowan mechanism) [58].

In case of cutting, the upper part of the particle with regard to the dislocation slip plane is displaced. The displacement is of the length of a Burgers vector and thus the phase boundary area is increased which results in an increase of the critical shear stress. Cutting only occurs in case of coherent and semi coherent phase boundaries because here the slip plane of the dislocation does not change due to the equal lattice structure (cf. section 2.4.3).

At incoherent phase boundaries between particle and matrix the dislocation bypasses the particle because of the differences in lattice structure (cf. section 2.4.3). This is

called the Orowan mechanism. The boundary forms an obstacle for the dislocation. This results in bending around the particle until connection and recombination of two anti-parallel dislocation parts behind the particle. A dislocation loop, called Orowan loop, remains after bypassing and affects the formation of other dislocations in other slip planes due to the field of tension.

Both possibilities do not depend on the external stress σ_a , but on the particle radius r_T . Figure 2.23 shows the development of the stress σ_S during the cutting process and the Orowan stress σ_{OR} . The radius r_{T_0} is the ideal radius, where the cutting process and the Orowan mechanism have the same process stress, and thus the maximum strength is reached. Below r_{T_0} the particles are cut and above the radius the Orowan mechanism is more suitable, because in any case the energetically most favourable way is chosen. In cases where the stress is not high enough the dislocations avoid the particles due to diffusion controlled climb. The ideal radius is given as follows:

$$r_{T_0} = \frac{Gb^2}{\gamma} \sqrt[3]{3} \tag{2.9}$$

 γ describes the effective boundary energy.

Figure 2.23: Development of the stress during particle cutting $\sigma_S \approx \sqrt{r_T}$ and the Orowan stress $\sigma_{OR} \approx -\frac{1}{r_T}$. The ideal particle radius r_{T_0} is reached where the process stresses are equal and the maximum material strength is reached.

2.6 Phase Diagrams

Phase transitions and transformations during time dependent thermal processes can be represented in phase diagrams, which are useful tools for goal orientated alloy design. Most available thermodynamic modelling tools for the establishment of phase diagrams, e.g. Thermocalc use the Calphad method (Calculation of Phase Diagrams). For accurate predictions using the Calphad method, experimental data have to be provided in advance. The method calculates thermodynamic equilibrium phases in multicomponent systems by means of molar Gibbs free energy G_m minimisation. In cases of impossible minimisation of the energy the phase is rated as a metastable one.

The total Gibbs free energy used in the Calphad method is given as follows by:

$$G_m = \sum_{i} x_i G_i^0 + RT \sum_{i} x_i \ln(x_i) + \sum_{i} \sum_{j>i} x_i x_j \sum_{\nu} L_{ij}^{(\nu)} (x_i - x_j)^{\nu}$$
 (2.10)

The first term describes the reference condition, where x_i is the molar fraction of the component i and G_i^0 is the Gibbs free energy of the pure phase of component i. The second term of equation 2.10 describes the free energy change due to mixing in an ideal solid solution, where R is the ideal gas constant ($\approx 8.314~\mathrm{Jmol^{-1}K^{-1}}$) and T the temperature of the system. The last term (excess energy term) describes the interaction of neighbouring atoms in a solid. The part $\sum_{\nu} L_{ij}^{(\nu)} \left(x_i - x_j\right)^{\nu}$ is the so called Redlich-Kister polynom. A detailed derivation of equation 2.10 can be found for example in [69].

2.7 Mechanical Properties

Mechanical properties provide information about the reaction of a material to external mechanical influences like stress or strain. Based on this information the place of action can be determined and/or optimisation approaches can be developed.

Creep

Time dependent plastic deformation of a material under constant stress is called creep. This process is continuous and runs slowly until material failure. The ideal course of the time-dependent strain ε during creep is given in figure 2.24. Total strain ε_t comprises the time-independent strain ε_0 and the time-dependent strain ε_f which increases during the whole creep process until rupture. The following applies:

$$\varepsilon_t = \varepsilon_0 + \varepsilon_f = \varepsilon_e + \varepsilon_i + \varepsilon_f \tag{2.11}$$

 ε_e is the elastic part of ε_0 and ε_i describes the time-independent, plastic initial strain.

Literature used in section 2.6: [69–72]

Figure 2.24: Schematic illustration of a physical creep curve ($\sigma = \text{const.}$) and technical creep curve (F = const.) [64].

Creep curves can be distinguished in physical and technical creep curves depending on the testing conditions. Physical creep curves consider the reduction in cross section during the test and thus the stress remains constant ($\sigma = \text{const.}$). In case of technical creep curves the load remains constant (F = const.), which results in rising stress during the test caused by the reduction in cross section. For that reason the curve in a technical test is steeper and rupture is reached earlier. The feasibility of tests with constant load are easier and furthermore technically more relevant. Therefore these tests are mostly performed under laboratory conditions.

Nevertheless the three stages of a creep curve can be observed in both cases. The offset at t = 0 is the elastic part ($\sigma <$ yield strength) of the strain ε_e as mentioned before.

Primary creep or initial stage (I.):

In the primary stage the creep rate $\dot{\epsilon}$ (slope of curve $\dot{\epsilon} = \frac{d\epsilon}{dt}$) decreases constantly until the minimum $\dot{\epsilon}_{min}$. The reason for this is that the external stress triggers plastic deformation and thus new dislocations are generated, which results in a mutual obstruction of dislocation movement and thus continuous hardening.

Secondary creep or steady-state creep (II.):

In the secondary stage the creep rate $\dot{\epsilon}_S$ stays minimal and remains constant. This is the result of a dynamic balance between the decrease and the increase of dislocation density $(\rho^-$ and $\rho^+)$ and thus between softening r and hardening h. The following applies:

$$\dot{\varepsilon}_S = \frac{\left|\frac{d\rho^-}{dt}\right|}{\frac{d\rho^+}{d\varepsilon}} = \frac{r}{h} = const. \tag{2.12}$$

Due to the persistent plastic deformation of the material cracks and pores occur and the next stage of the creep curve is initiated.

Tertiary creep (III.):

In the tertiary stage material damage caused by e.g. grain boundary sliding increase the creep rate. At a random weak position the material necks until rupture.

2.8 Transmission Electron Microscopy (TEM)

During the 1930s the use of electrons instead of light gave the opportunity to overcome the limited image resolution of light microscopes, which is imposed by the wavelength of visible light. The idea is based on the research of E. Ruska and M. Knoll [73]. In 1986 E. Ruska received the Nobel Prize in physics and was honoured for the progress in electron microscopy history.

The transmission electron microscope (TEM) is used in various fields of science, e.g. in biology for high resolution images of cell structures, viruses or DNA components. Another field is materials science where the TEM is utilized for analyses of composite materials, microstructure and dislocations in metals or crystal lattice structures.

For analysis the electrons pass through the sample. Magnifications up to 500,000 times and a resolution of 0.2 nm are possible. In comparison the resolution of an optical microscope is 200 nm.

2.8.1 Fundamental Principles

The resolution g of a TEM depends on the wavelength λ and can be calculated with the equation of Abbe:

$$g = 0.61 \frac{\lambda}{n \sin(\alpha)} \tag{2.13}$$

n indicates the refractive index of a material ($n \approx 1$, air) and α indicates the aperture (half the field angle of the objective, for the TEM $\alpha \approx 0.3$).

The term $n \sin(\alpha)$ is called numerical aperture and describes the maximal light beam a lens can collect. For calculation of the wavelength the equation of De Broglie can be used. This equation considers the wave character of particles. The following applies:

$$\lambda = \frac{h}{mv} = \frac{h_p}{p} \tag{2.14}$$

Where $h_p \approx 6,626 \cdot 10^{-34}$ Js is the Planck's constant, m is the mass, v is the velocity and p is the momentum of a particle.

For electrons with an acceleration voltage of U_A the relativistic conservation of energy

 E_r is given by:

$$E_r = \sqrt{p^2 c^2 + m_0^2 c^4} = m_0^2 c^2 e U_A \quad \to p = \sqrt{2m_0 e U_A \left(1 + \frac{e U_A}{2m_0 c^2}\right)}$$
 (2.15)

 m_0 is the rest mass of an electron, c is the speed of light in vacuum, m_0c^2 describes the rest energy of an electron and e is the elementary charge.

Combining equations 2.14 and 2.15 the relation for the wavelength regarding the acceleration voltage of an electron is given by:

$$\lambda = \frac{h}{\sqrt{2m_0eU_A\left(1 + \frac{eU_A}{2m_0c^2}\right)}} \tag{2.16}$$

Besides resolution limitations caused by particle wavelength the resolution is limited by aberrations of the objective lens as well. Spherical and chromatic aberrations are limiting the resolution to approximately 0.1 nm to 0.2 nm and depend on lens aperture. Spherical aberration d_S describes the defocussing of outer beam electrons to the focal point, thus these electrons are more deflected. The following applies:

$$d_S = \frac{1}{2}C_S\alpha^3 \tag{2.17}$$

 $C_{\rm S}$ marks the spherical aberration coefficient and depends on the acceleration voltage and the focal length of the lens. To improve spherical aberration an aperture can be used to shield outer beam electrons.

Aberrations caused by electrons with different wavelengths or rather different velocities are called chromatic aberrations. This error only occurs at lenses and results in focusing of electrons at different points of the optical axis. For the chromatic aberration d_c follows:

$$d_c = \frac{\delta E}{E} C_c \alpha \tag{2.18}$$

 $\frac{\delta E}{E}$ describes the beam voltage difference and C_c is the so-called chromatic aberration coefficient which depends on the focal length of the lens.

2.8.2 Architecture

The general principle of a TEM is similar to the principle of an optical microscope (cf. figure 2.25), but in case of the TEM magnetic lenses instead of optical lenses made of glass are used. These magnetic lenses are controlled by the coil current and thus the focal length can be varied. Magnetic fields up to two Tesla can be generated in the pole shoe gap of the magnetic lenses. Another difference between the microscopes is the "light source ". Due to thermionic emission or field emission in the electron source, electrons are emitted.

Figure 2.25: Schematic architecture and beam path of a TEM (left) and of an optical microscope (right) [74].

In the condenser lens system the electron beam is amplified. Figure 2.25 shows a schematic architecture of a TEM. In general a TEM possesses two condenser lenses. The first lens with a high magnetic field, but limited configuration options and fixed current reduces the beam diameter from approximately 50 μ m down to approximately 1 μ m. The second lens has a weaker magnetic field, but variable configuration options. By means of this lens the beam diameter can be varied from 1 μ m to 10 μ m and therefore influences the quality of the image. Furthermore the condenser lenses are equipped with aperture diaphragms, which shield the sample from scattered electrons and thus defines the aperture angles. A small aperture decreases the angle of beam convergence and therefore makes the beam more parallel.

After the condenser lens system the beam reaches the sample. By the sample holder, which is inserted sideways into the TEM, the sample can be moved in all three dimensions and tilted laterally.

The objective lens is the most important lens in a TEM. This lens is responsible for the first magnification of the sample image. Lens aberrations of the objective lens have a significant influence on image quality.

The intermediate lens is located below the objective lens. Due to changes of the current the lens can be focussed to the focal plane or image plane of the objective lens. The last lens of the system is the projection lens, which projects the image onto the fluorescent screen.

2.8.3 Imaging

The imaging of a sample is influenced by several interactions of the electrons with the sample like absorption, diffraction, elastic scattering and inelastic scattering.

Absorption

Absorption provides only an insignificant part to the image contrast, but produces artefacts in the images. High absorption in an image is caused by contamination or an accumulation of heavy elements.

Inelastic scattering

In case of inelastic scattering the beam electrons interact with the sample electrons. In general inelastic scattering transfers energy to the sample, but there is no simple relationship between this loss of energy and the scattering angle. The scattering can be separated into different processes, where X-rays or secondary electrons are generated and collective interactions with several atoms or electrons occur. By means of these processes different image types can be generated or rather information about chemical composition and electronic structure can be obtained.

Elastic scattering and diffraction

Interactions of beam electrons and the Coulomb potential of the atomic nuclei are called elastic scattering. During these interactions no energy is transferred from the scatted electron to the sample atoms due to the large difference in mass between the electron and nuclei. Elastically scattered electrons influence the diffraction contrast of the image amongst others issues.

The scattering of these electrons in crystalline samples can be described by the Bragg condition:

$$n\lambda = 2d_{hkl}\sin\left(\Theta\right) \tag{2.19}$$

Where λ is the wavelength, $2d_{hkl}$ describes the lattice spacing, the subscript hkl indicates the Miller indices and Θ describes the diffraction angle. Hence, constructive interference or rather scattering at a lattice plane occurs only in case of multiple n of the wavelength (cf. figure 2.26).

The Bragg condition for diffraction is $\vec{G}_{hkl} = \vec{k}_0 - \vec{k}$. With this condition the Ewald construction (cf. figure 2.27) for the reciprocal lattice describes the possibility for reflection. These reflections are visible in the TEM.

Figure 2.26: Bragg condition: The path difference of beams is $2d_{hkl} \sin(\Theta)$ [75].

Figure 2.27: Illustration of the condition $\vec{G}_{hkl} = \vec{k}_0 - \vec{k}$, a visible reflection occurs, if \vec{G} ends on the Ewald sphere [75].

Dark field and bright field

The TEM allows imaging in two different modes, the so-called dark field (DF) and bright field (BF) modes. The main difference is the used optical path, which is adjusted by the position of the objective lens and thus different electrons are detected. The schematic optical path of both modes is given in figure 2.28.

Figure 2.28: Optical path of bright field (left) [76] and dark field mode (right) [77].

In case of the dark field mode (cf. figure 2.28, right) only the diffracted beam is allowed to pass, more precisely the elastically scattered electrons. Although the image is dark the contrast in this mode is very high, e.g. stacking faults and particles appear brighter. In contrast to the dark field mode areas of heavy atoms or thick sample areas appear dark in the bright field mode (cf. figure 2.28, left). In this mode only the electrons of the zero order (direct beam) are detected.

2.8.4 General Sample Preparation

As previously described the image quality depends strongly on lens aberrations. However this is not the only limiting factor. Mistakes during sample preparation or incorrect preparation lead to poor results. In general it is necessary to prevent thermal and mechanical modifications of the sample during preparation, e.g. cold deformation. Furthermore the samples have to be very thin to ensure the transparency for electrons. Depending on the analyses of the sample various preparation methods are suitable.

Thin foils and electrolytic polishing

For the preparation of metallic foils by electrolytic polishing the following steps are necessary: First the material has to be cut in slides of approximately 1 mm thickness. After that grinding of both sides with different sandpaper (P240 to P1200) to a thickness of 50 to 100 μ m ensures the removal of modifications caused by sawing. Prior to the actual polishing the foil has to be punched in discs of 3 mm in diameter. The punch is constructed taking into account that the middle of the disc is stress-free. For polishing the discs are fixed between two nozzles and blasted from both sides with

electrolytes. Therefore an electric circuit is established with a DC-power supply, where a cathode is placed in the electrolyte and the sample acts as an anode. In case of a closed circuit, material will be electrolytically removed from the sample disc. The aim is to polish a v-shaped hole into the disc. Due to the potential difference between the sample and the cathode where the electrolytes are located, the sample is polished until a hole occurs (cf. fig. 2.29a). The hole is detected by an infrared detector, which automatically stops the polishing process. The edges of the hole are thin enough to be permeable for electrons and enable TEM analysis (cf. fig. 2.29b).

(a) (b)

Figure 2.29: (a) Sample and (b) magnification of the hole after electrolytic polishing.

Replicas

The preparation of so called particle replicas requires thin foils as well. In contrast to electrolytic polishing the prepared foils can be slightly thicker. Both sides of the foils are coated with carbon. This carbon coating ensures that the particles are fixed after dissolving the alloy matrix. For better handling after dissolving the carbon coating is carved into squares. Dissolution of the matrix takes place in bromine with ethanol (10 %vol). The period of dissolution depends on sample thickness. After the dissolution only particles between the carbon film remain and are cleaned with ethanol. Last step of the preparation is the "fishing" of the carbon film with particles out of a mixture of distilled water and ethanol with the help of small grids made of copper. After drying, these grids with a diameter of 3 mm can be implemented into the TEM sample holder. The individual steps of preparation are depicted in figure 2.30.

Figure 2.30: Individual steps of replica preparation [78].

Focused Ion Beam (FIB)

The preparation by focused ion beam (FIB) allows the preparation of very fine lamellae (cf. fig. 2.31) by material removal. The size of the lamellae is approximately 10 x $10 \text{ }\mu\text{m}$ with a thickness of 150 nm. Besides material removal FIB also can be used for surface analysis.

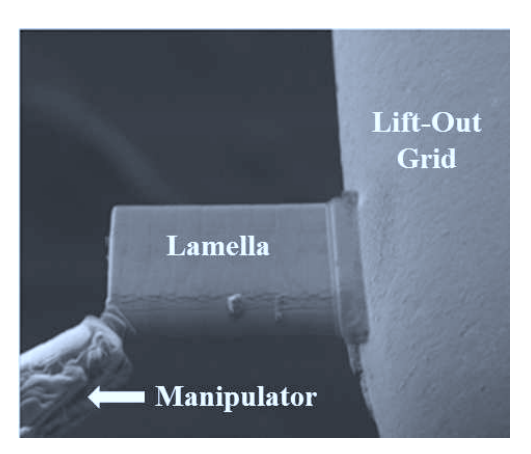


Figure 2.31: Imaging example of a FIB lamella [79].

The fundamental functionality is similar to the functionality of a scanning electron microscope, but instead of focussed electrons gallium ions are utilized. The ions are focussed by electrostatic lenses. A deflection system is used, so that the sample can be scanned line-by-line. By scanning of the sample secondary electrons arise, which can be used for imaging. The gallium ions are generated with a liquid **metal ion sources** (LIMS). More precisely by means of a tungsten needle the gallium is heated up to its

melting point ($T_{Ga} = 29.7646$ °C [80]). Due to field emission an ion beam is produced with an ion acceleration voltage of up to 50 kV. The current of the beam is between 1 pA and 1.3 μ A and is controlled by apertures. Depending on this current a coarse material removal or refined thinning is achievable. After cutting the lamella is mounted on a so-called lift-out grid (cf. figure 2.32a) with a diameter of 3 mm. This grid can be installed in the TEM holder (cf. figure 2.32b).

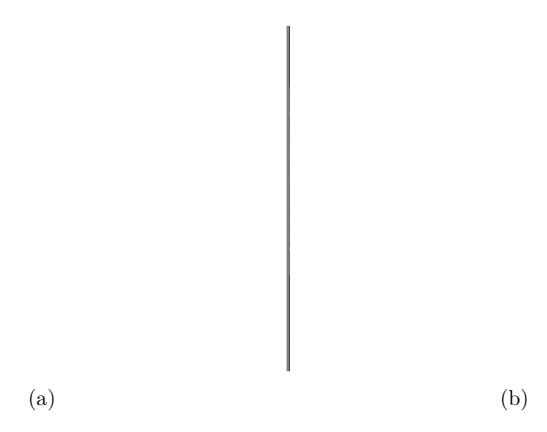


Figure 2.32: (a) Lift-out grid with FIB lamella (red arrow) and (b) lift-out grid installed in a TEM holder.

2.9 Scanning Electron Microscopy (SEM)

In contrast to TEM the electrons do not irradiate the sample during scanning electron microscopy (SEM). The electrons are focussed by means of a condenser and objective lens to the surface of the sample. Due to deflection coils the electron beam scans the sample in a defined raster. The electrons of the beam interact with electrons close to the surface and produce secondary electrons (SEs) with an energy up to 50 eV. Due to the low exit depth (few nanometres), a resolution of 1-10 nm can be achieved. The interaction region of the beam electrons depends on the acceleration voltage (approximately 20 V - 30 kV [85], cf. figure 2.33) and the density of the sample. The SEs are collected by a detector and converted into a specific voltage, which results in a specific intensity. Elevations of the surface occur brighter than indentations caused by the different amounts of SEs. SE images typically show topography contrasts. In contrast to surface morphology imaging with SEs the imaging with backscatter

Literature used in section 2.8: [81–84]

electrons (BSEs) results in range images. The BSEs energy (up to 100 % of the primary electrons) is much higher than the energy of the SEs (up to 50 eV) so that the BSEs interact with sample electrons of deeper locations. The contrast of the image depends on the atomic number, more precisely this means that the brightness is higher at higher atomic number, because of higher probability of interaction. Due to the larger interaction area of the BSEs in comparison to the SEs the resolution is lower (approximately half exit depth of the primary electrons). The functionality of a SEM results in a less complicated sample preparation, because the samples do not need to be very thin.

For crystallographic analyses the electron backscattered diffraction (EBSD) pattern method is used. Inelastically scattered electrons interact with the lattice of the sample and produce a divergent source. Originating from this source elastic scattering at lattice planes with fulfilment of the Bragg condition is possible. Due to scattering close to the surface, electrons can leave the sample. Detection of these electrons results in the so-called Kikuchi pattern. The structure or orientation can be identified by means of these patterns, which are specific for different crystal structures and orientations. The TEM scanning mode (STEM mode) operates similar to a SEM, but an acceleration voltage of up to 200 kV [86] is used. This higher voltage and very thin samples result in higher magnifications.

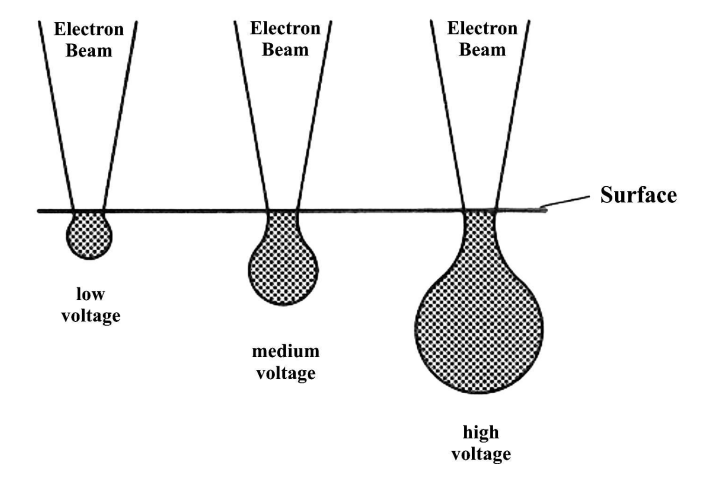


Figure 2.33: Dependence of acceleration voltage interaction [81].

Literature used in section 2.9: [81]

3 Experimental

3.1 Materials and Production

Three different trial alloys were investigated in this work. The chemical compositions of the trial alloys are given in table 3.1. The alloys 2.5W0.57Nb0Ti, 2.1W0.49Nb0Ti and 18Cr were produced in 10 kg ingots by vacuum melting at VDM Metals GmbH, annealed at 1080 °C for 2 h and subsequently hot-rolled into plates of 20 mm thickness at approximately 980 °C with final air-cooling to ambient temperature.

Table 3.1: Chemical compositions of trial alloys 2.5W0.57Nb0Ti, 2.1W0.49Nb0Ti and 18Cr (in wt.%).

	\mathbf{C}	N	\mathbf{Cr}	\mathbf{W}	Nb	Si	$\mathbf{M}\mathbf{n}$	La	Ti	Ni
2.5W0.57Nb0Ti	0.004	0.008	22.95	2.50	0.57	0.20	0.46	0.034	0.004	0.02
2.1W0.49Nb0Ti	0.002	0.004	23.08	2.10	0.49	0.24	0.45	0.12	0.003	0.02
18Cr	0.002	0.005	18.50	1.98	0.51	0.24	0.44	0.12	0.057	0.01

3.2 Annealing Experiments and Sample Preparation

Cubic specimens were cut from the as-received, hot-rolled plates with an edge length of approx. 5 mm and short-term furnace annealed (FA) for different times at 600 °C and 650 °C. Samples for long-term particle analysis were extracted from quasi stress-free head sections (cf. figure 3.1; position 1) taken from 600 °C and 650 °C creep specimens (CS) (cf. section 4.3.2). For particle evolution analysis under mechanical stress (cf. section 4.4.2) the samples were taken from gauge length sections without macroscopical deformation (cf. figure 3.1; position 2). The materials entered the annealing experiments and creep tests in the hot-rolled state without additional precipitation heat treatment. Table 3.2 gives an overview about the annealing time steps, temperatures and types of annealing (FA or CS).

Figure 3.1: Creep specimen: Before testing (bottom) and after rupture (top). The red rectangles indicate the positions where the samples were cut from: Position 1 shows the stress-free head section, position 2 the uniformly deformed gauge length section.

Table 3.2: Overview about the annealing time steps, temperatures and type of annealing of alloy (a) 2.5W0.57Nb0Ti, (b) 2.1W0.49Nb0Ti and (c) 18Cr (FA:= furnace annealing; CS:= Creep specimen; NA:= Not available for this time/temperature).

(a) 2.5W0.57Nb0Ti

	2 h	100 h	1,000 h	2,425 h	9,808 h	26,032 h	40,789
600 °C	FA	FA	FA	NA	NA	CS	CS
650 °C	FA	FA	FA	CS	CS	NA	NA

(b) 2.1W0.49Nb0Ti

	2 n	30 n	100 h	1,000 h	2,579 n	8,608 n	37,916
600 °C	FA	NA	FA	FA	NA	NA	CS
650 °C	FA	CS	FA	FA	CS	CS	NA

(c) 18Cr

	2 h	100 h	1,000 h	$2,500 \mathrm{\ h}$	6,662 h	29,395 h
600 °C	FA	FA	FA	NA	NA	CS
650 °C	FA	FA	FA	FA	CS	NA

All samples for microstructural investigation were embedded in epoxy resin for metallographic preparation, ground (P800 to P2500) and polished (6 μ m, 3 μ m, 1 μ m) for 1-2 h per step to a sub-micron finish for EBSD analysis. For the analysis of particle evolution the samples were subsequently polished with Al₂O₃ in dilute KOH solution for approx. 4 h and electrolytically etched at 1.5 V in 5% H₂SO₄ to enhance the contrast between particles and matrix.

3.3 Microstructural Analysis

3.3.1 HR-FESEM and Image Analysis

A Zeiss Merlin SEM was applied for the investigation of particle size evolution of alloy 2.5 W 0.57 Nb 0 Ti, 2.1 W 0.49 Nb 0 Ti and 18 Cr. Therefore high resolution field emission scanning electron microscopy (HR-FESEM) images (2.5 k- and 10 k- fold magnification, 6144×4608 pixels, 7.44 nm per pixel in 2.5 k / 1.86 nm per pixel in 10 k magnification, back scattered electrons) were taken.

The images were processed and analysed by means of the commercial software package AnalysisPro ®. Figure 3.2a displays an example of an HR-FESEM image. The post-processing included filtering to reduce statistical noise, shading correction to balance inequalities of the background as well as optimisation of contrast and intensity (cf. figure 3.2b). Particles for size evolution analyses were detected and analysed after image post-processing and binarizing the raw image. An example for a binarized HR-FESEM image is given in figure 3.2c.

The 2D analyses of 3D structures always comprises difficulties like the shape and position of non-globular particles or the presence of sub-grain structures. Particle shape and position cause size differences with regard to the cut plane and thus differences of the detected area (cf. figure 3.3). In some cases sub-grain structures are detected as particles. Comparison of the sub-grain structure in the original HR-FESEM image (figure 3.2a) and the binarized image (figure 3.2c) illustrate this. A more detailed illustration is given in figure 3.4a and b.

Further difficulties emerge from small "close vicinity" and "sub surface" particles. "Close vicinity" particles cannot always be detected separately, because of their close proximity to each other (cf. figure 3.4c and d). "Sub surface" particles located close to the surface are imaged without sharp contours, but nevertheless are detected by the software (cf. figure 3.4e and f). To improve the comparability of the particle evolution results, sub-grain structures and particles > 35 pixels of the character described beforehand are removed manually after detection. Particles below 10 nm were excluded from the examination, because of insufficient resolution of the raw SEM images. Furthermore large particles, which occur on occasion and are clearly identified as primary carbides and/or nitrides, were excluded.

(a)

(b)

(c)

Figure 3.2: Example of an HR-FESEM image (a) original [87] (left) with a magnification of the selected area (right). (b) HR-FESEM image after post-processing (left) with a magnification of the same selected area (right) and (c) after binarizing (left) and magnification of the same selected area (right) (alloy 2.5W0.57Nb0Ti after 1,000 h at 600 °C).

Figure 3.3: Schematic illustration of the size differences of the detected area regarding to the cut plane.



Figure 3.4: Examples of "misdetected" particles: Sub-grain boundary (a) detected as a particle after post-processing and (b) after detection (greatly enlarged). "Close vicinity" particles (c) after post-processing and (d) after detection (greatly enlarged). "Sub surface" particle (e) after post-processing and (f) after detection (greatly enlarged).

For the classification of Laves phase particles and other existing phase structures in case of alloys 2.5W0.57Nb0Ti, 2.1W0.49Nb0Ti and 18Cr (cf. section 4.3.4) the EBSD technique (AZtec, Oxford Instruments; NORD LYS 2 camera) was utilised. This technique was utilised as well for investigations of sub-grain boundary formation and dislocation behaviour in alloy 2.5W0.57Nb0Ti (cf. section 4.6). Furthermore band contrast

images, orientation and misorientation mappings were taken for investigation of dislocations and grain boundary formation. Band contrast images are an image quality factor derived from the EBSD pattern. They display the average intensity of the Kikuchi bands with regard to the overall intensity. Darker grey indicates poorer pattern quality. Therefore grain boundaries are displayed as dark grey lines due to their poor pattern quality. Furthermore differences in the orientation (misorientation) from one point to another can be measured and depicted as high and low angle boundaries. In the orientation images the absolute orientation of the grains based on the measured Kikuchi pattern are described, while in case of misorientation mappings only the differences in orientation are displayed (cf. section 4.6).

3.3.2 STEM

For the chemical composition analyses (cf. section 4.3.3) of the Laves phase particles and the alloy matrices of alloys 2.5W0.57Nb0Ti, 2.1W0.49Nb0Ti and 18Cr energy dispersive X-ray (EDX) spectroscopy (X-Max 80, Oxford Instruments) was utilised. Images of particles and dislocations in alloy 2.5W0.57Nb0Ti, 2.1W0.49Nb0Ti and 18Cr were taken in scanning transmission electron microscope mode (STEM) utilizing a high angle annular dark field (HAADF) detector. The applied microscope was a Zeiss Libra 200 TEM with an acceleration voltage of 200 kV.

For the analyses all samples were prepared utilizing Ga-ions in a Zeiss Auriga cross beam focused ion beam (FIB) facility. The thickness of the cut lamellae was approx. 200 nm with a size of $10\times10~\mu m$.

3.4 Thermodynamic Modelling of Phase Diagrams

To accomplish thermodynamic modelling of alloy 2.5W0.57Nb0Ti, 2.1W0.49Nb0Ti and 18Cr the software Thermocalc[®] (database TCFE6.2) was applied. The software uses the Calphad method (cf. section 2.6) to calculate thermodynamic equilibrium phases. For simplification of the calculations only the alloying elements Cr, Nb, W, Si, Fe, Mn and Ti (cf. table 3.1) were considered.

4 Results and Discussion

4.1 Previous Studies

Previous studies concentrated on the creep behaviour of trial alloys on the technological base of the commercial Crofer® 22 H grade [1] (cf. section 2.2). Figure 4.1 shows 600 °C and 650 °C creep curves of several trial alloys, which were analysed in more detail in this work, in comparison to the ferritic-martensitic steel P92 at 100 and 81 MPa at 600 °C and 650 °C (cf. section 2.1). P92 creep specimens were taken from a pipe section, perpendicular to the pipe extrusion direction. The creep test specimens of alloy 2.5W0.57Nb0Ti, 2.1W0.49Nb0Ti and 18Cr were taken from the trial alloys in a corresponding manner perpendicular to the rolling direction. The trial alloys were tested at different stress levels equal or higher than 120 MPa at 600 °C and equal or higher than 70 MPa at 650 °C. For the 18Cr alloy only a 120 MPa test at 600 °C and a 70 MPa test at 650 °C were performed. The specimen ruptured after 29,399 h at an elongation of 15.6 % at 600 °C/120 MPa and after 6,622 h (elongation: 20.3 %) at 650 °C/70 MPa.

The comparison of stress rupture properties of all the alloys in comparison to P92 is given in figure 4.2. Here the dotted lines describe the P92 specification limits (\pm 20 % of the mean specification). The mean value is calculated by several tests and P92 batches and published by the European Creep Collaborative Committee (ECCC) [88]. Differences between the specification values for P92 and the creep performance of the P92 trial batch, which lies in general above the specification or at the upper limit can be explained by the fact that the specification is based on several test and thus a single test is compared with a mean. The chemical composition of the P92 trial batch is given in [35], where the batch was analysed at 600 °C in more detail.

In case of alloy 2.5W0.57Nb0Ti and 2.1W0.49Nb0Ti the creep performance is considerably better compared to 18Cr. Material 2.1W0.49Nb0Ti at 120 MPa ruptured after 39,781 h at 600 °C (elongation: 19.1 %). The 2.5W0.57Nb0Ti material exhibited superior creep behaviour, but unfortunately the specimen was lost after 40,789 h at 120 MPa. Due to a malfunction of the temperature controller the specimen was mechanically overloaded at low temperature. At this time the specimen was still in the secondary creep regime (cf. figure 4.1a). At 650 °C/70 MPa the 2.5W0.57Nb0Ti material is the most creep resistant alloy in comparison to the 2.1W0.49Nb0Ti and 18Cr materials, too. The specimen ruptured after 9.808 h (elongation: 10.6 %), while alloy

2.1W0.49Nb0Ti ruptured after 8,608 h with an elongation of 21.3 %. At high stress (145 MPa, 600 °C) alloys 2.5W0.57Nb0Ti and 2.1W0.49Nb0Ti furthermore achieved rupture times approaching P92. The alloys ruptured after 14,267 h and 12,086 h (elongations: 10.9 % and 12.2 %). This can also be observed at the higher stress level (100 MPa) at 650 °C. Here the 2.5W0.57Nb0Ti material failed after 2,425 h and the 2.1W0.49Nb0Ti material after 2,579 h (elongations: 14.2 % and 41.1 %). The strength of this kind of material is influenced by the initial dislocation density and the chemical composition depending. At high stress levels the strength of the alloys is stronger influenced by the initial dislocation density, while at low stress levels the chemical composition is dominant for material strength. More detailed description of the mechanical properties of the tested alloys at 600 °C and other trial steels is given in [1].

(a)

(b)

Figure 4.1: Creep curves of the 2.5W0.57Nb0Ti, 2.1W0.49Nb0Ti and 18Cr alloys with stress levels at (a) 600 °C (based on [1]) in comparison to P92 (1,040 °C - 1,070 °C, 2 h/ 730 °C - 800 °C, 2 h) [35] at 100 MPa and (b) at 650 °C in comparison to P92 (1,065 °C - 1,070 °C, 2 h/ 770 °C - 775 °C, 2 h) at 81 MPa.

(a)

(b)

Figure 4.2: Comparison of the stress rupture properties of the 2.5W0.57Nb0Ti, 2.1W0.49Nb0Ti and 18Cr trial alloys and the AFM steel P92 specification (dotted lines [88]) and a P92 trial batch at (a) 600 °C [35] and (b) 650 °C.

4.2 Selection of Sample Preparation

As mentioned in section 3.3.2 FIB lamellae were prepared for TEM analyses. This method was chosen due to the ferro-magnetic properties and the high particle density in the material. The classical preparation methods like electrolytic polishing and replicas (cf. section 2.8.4) are unsuitable. In case of electrolytic polishing two effects occur: First, the magnetisation of the sample along the magnetic field of the TEM lenses and thus an amplification of this field. This complicates the control of the electron beam and focusing on the sample. Magnetisation of the sample also occurs in case of FIB

lamellae, but here much less material is magnetised. For comparison, a lamella with a thickness of approx. 0.2 μm and a size of $10 \times 10~\mu m$ has a volume of $V \approx 20~\mu m^3$, while an electrolytic polished sample with a disc diameter of 3 mm and thickness of approx. 100 μm has a volume of $V \approx 7 \cdot 10^8~\mu m^3$. Therefore the magnetisation of a lamella and the resulting amplification of the magnetic field can be controlled sufficiently.

The second effect is a generated counter magnetic field caused by the sample geometry, which results in an induced current $I_{\rm ind}$ according to Lenz's law. The induced current is triggered by the impinged electron beam. The counter magnetic field acts against the electron beam. Figure 4.3a shows this effect schematically. In case of replicas the large number of particles in the alloys inevitably leads to overlapping of individual particles. This reduces the precision of results evaluated from extraction replicas (cf. figure 4.3b)

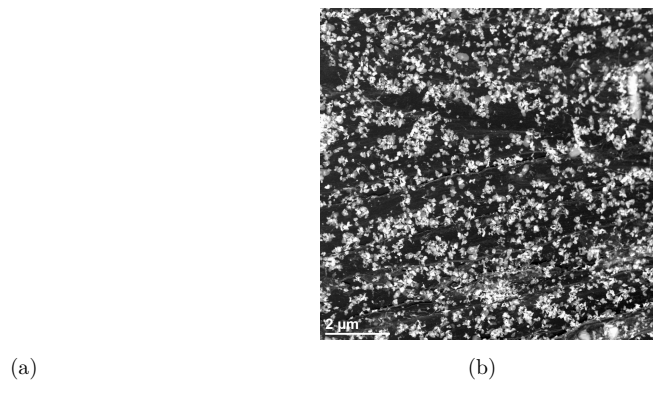


Figure 4.3: (a) Schematic illustration of the generation of a counter magnetic field in case of electrolytically polished sample. The field acts against the electron beam. (b) TEM image of a trial alloy prepared with the replica method. Caused by the high particle density and thus overlapping, the particles cannot be analysed individually (alloy 2.1W0.49Nb0Ti, solution annealed, precipitation annealed at 600 °C after 1,000 h).

4.3 Thermodynamic Modelling and Verification by Electron Microscopy Examination

4.3.1 Thermodynamic Modelling

The software Thermocalc (TC, database TCFE6.2) was applied to accomplish thermodynamic modelling for alloy 2.5W0.57Nb0Ti, 2.1W0.49Nb0Ti and 18Cr. For simplification only the alloying elements Cr, Nb, W, Si, Fe, Mn and Ti were regarded in the calculations. By means of these selected alloys several effects of alloying elements

like chromium and the Laves phase forming elements tungsten, silicon and niobium can be demonstrated. The modelling results are given in figure 4.4.

(a)

(b)

Figure 4.4: Mass fractions of (a) Laves phases (partly replotted from [1]) and (b) σ-phase of alloy 2.5W0.57Nb0Ti, 2.1W0.49Nb0Ti and 18Cr [37].

Calculations of Thermocalc® show the presence of two different C14 Laves phases (cf. figure 4.4a, section 2.3.2). The first one is stable in a comparatively small region at low temperatures (approx. 550 °C to 650 °C) and therefore called "low temperature" (LT) Laves phase for practical reasons in the following. The second Laves phase, which is stable up to approx. 1,000 °C, is called "high temperature" (HT) Laves phase hereafter.

At 600 °C the presence of both phases is calculated in case of alloy 2.1W0.49Nb0Ti and 18Cr. The modelled dissolution temperature of the LT Laves phase in alloy 2.1W0.49Nb0Ti is 608 °C, while in case of 18Cr the temperature is 664 °C. The

predicted dissolution temperature of the HT Laves phase in alloy 2.1 W 0.49 Nb 0 Ti is 957 °C and 956 °C for alloy 18Cr. In the intended application temperature range from 600 °C to 650 °C the modelling predicts only the HT Laves phase in case of alloy 2.5 W 0.57 Nb 0 Ti. The dissolution temperature of the LT phase in the 2.5 W 0.57 Nb 0 Ti material is 560 °C, for the HT phase it is 987 °C. Hence, only in case of the 18Cr both Laves phases are present at 650 °C.

Modelling results clarify the influence of the elements Cr, W, Nb and Si on phase formation: The 18Cr material substantially differs from the 2.1W0.49Nb0Ti material by a decreased chromium content. This results in a shift of the LT phase to higher temperatures. The effect of Nb, W and Si become more obvious by consideration of alloy 2.5W0.57Nb0Ti in comparison to 2.1W0.49Nb0Ti and 18Cr. Alloy 2.5W0.57Nb0Ti exhibits higher W and Nb contents in combination with lower Si content than the other two alloys, which results in an increase of the HT phase fraction. Segregation of the precise impact of the individual species on phase stability would require in-depth parameter variation and should be analysed in future investigations, but is not part of this work.

Besides the effect on the LT phase, chromium obviously promotes the formation of the unfavourable, potentially embrittling (Fe,Cr)- σ -phase (cf. section 2.3.3). Figure 4.4b shows the mass fractions of (Fe,Cr)- σ -phase in alloys 2.5W0.57Nb0Ti, 2.1W0.49Nb0Ti and 18Cr. So far, alloy 2.5W0.57Nb0Ti is the most creep resistant alloy of these three trial alloys (cf. section 4.1), but it features a comparatively high chromium content (22.95 wt.%). In this case and in case of alloy 2.1W0.49Nb0Ti (23.08 wt.%) the high chromium content favours the formation of the (Fe,Cr)- σ -phase in the application temperature range of 600 °C to 650 °C. A decrease of the chromium content ensures a reduction of (Fe,Cr)- σ -phase fraction in that temperature range (cf. figure 4.4b, red dotted curve of alloy 18Cr) [37,89].

4.3.2 STEM Examination at 600 °C and 650 °C

By TEM examination in scanning mode (HAADF detector) the existence of two different Laves phases was successfully verified. After mid-term annealing (1,000 h) at 600 °C and 650 °C both phases preferably appear at the grain boundaries. The phases occur in the shape of dual phase particles with an HT-shell and an LT-core in case of alloy 2.1W0.49Nb0Ti and 18Cr. These results are in good agreement with the modelling results in terms of the 18Cr material for both temperatures (after 1,000 h at 600 °C and at 650 °C). As mentioned in section 4.3.1 only at 600 °C both phases are predicted to be present in case of the 2.1W0.49Nb0Ti material. However, the TEM measurement also indicated the presence of dual phase particles in the 2.1W0.49Nb0Ti material at 650 °C after 1,000 h. The dual phase particles in alloy 18Cr and 2.1W0.49Nb0Ti after 1,000 h of annealing at 600 °C and 650 °C are depicted in figure 4.5.

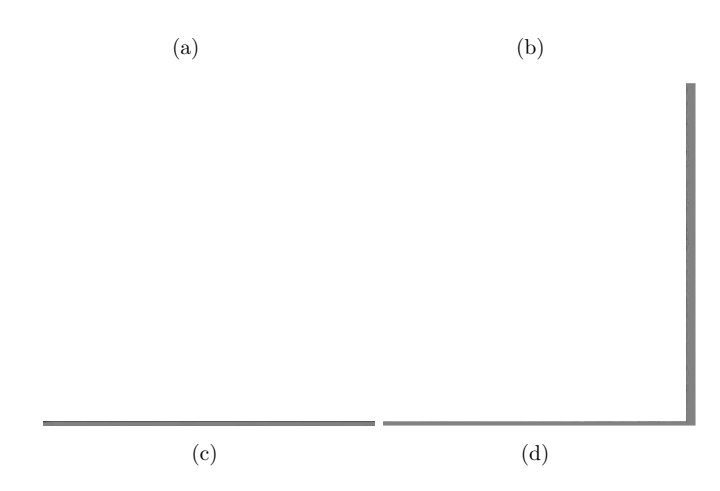


Figure 4.5: Dual phase particles at the grain boundaries with HT-shell and LT-core after 1,000 h at 600 °C in alloy (a) 18Cr and (b) 2.1W0.49Nb0Ti. Similar particles with dual phase character after 1,000 h at 650 °C in materials (c) 18Cr and (d) 2.1W0.49Nb0Ti.

Element mappings of the dual phase particles prove the HT-shell to be rich in tungsten and the LT-core having a comparatively high niobium content. The distributions of W and Nb in the dual phase particles for the 2.1W0.49Nb0Ti and 18Cr materials at 600 °C and 650 °C are given in figures 4.6 and 4.7. These particles were sufficiently big for precise analyses of the chemical compositions by TEM. The classification of LT and HT as the core and shell phase is determined by precise analyses of the chemical composition (cf. section 4.3.3). These analyses also show that only the LT phase contains a small amount of Si, which will be discussed in more detail in section 4.3.3.

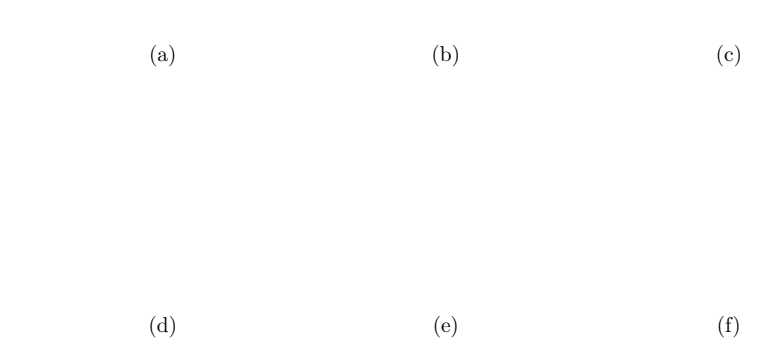


Figure 4.6: Element mappings of dual phase particles at 600 °C after 1,000 h in alloy 18Cr (upper row) and 2.1W0.49Nb0Ti (lower row): (a)+(d) STEM-HAADF image at 200 kV, (b)+(e) Nb and (c)+(f) W mappings.

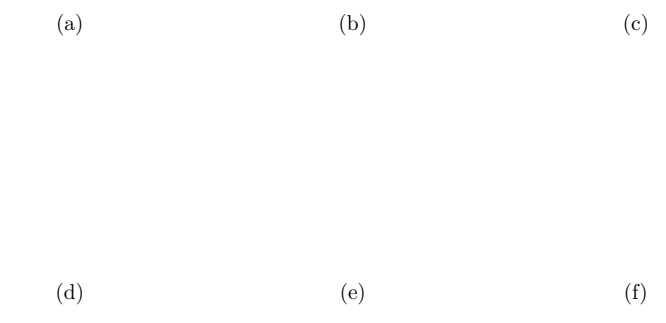


Figure 4.7: Element mappings of dual phase particles at 650 °C after 1,000 h in alloy 18Cr (upper row) and 2.1W0.49Nb0Ti (lower row): (a)+(d) STEM-HAADF image at 200 kV, (b)+(e) Nb and (c)+(f) W mappings.

Analysis of the particles in alloy 2.5W0.57Nb0Ti also indicates the presence of dual phase particles as described above, while the modelling only predicted the presence of the HT Laves phase in this alloy in the temperature range from 600 °C to 650 °C (cf. section 4.3.1). Potentially dual phase particles in alloy 2.5W0.57Nb0Ti after 1,000 h at 600 °C and 650 °C are depicted in figure 4.8. Because of the small size of these dual phase particles at 600 °C and of the LT-core at 650 °C after 1,000 h of annealing detailed analysis of the chemical compositions of the shell and core regions failed to date, but element mappings of W and Nb for the particles confirm the presence of dual phase particles (cf. figure 4.9). In case of the 2.5W0.57Nb0Ti material the dual phase particles preferentially occur at the grain boundaries, too.

(a)

(b)

Figure 4.8: Potentially dual phase particles at the grain boundaries with HT-shell and LT-core after 1,000 h in alloy 2.5W0.57Nb0Ti (a) at 600 $^{\circ}$ C and (b) 650 $^{\circ}$ C.

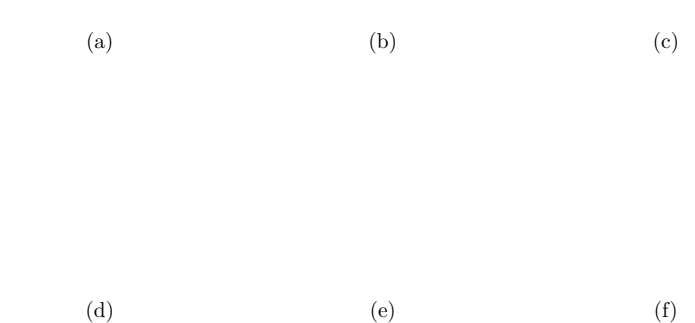


Figure 4.9: Element mappings of dual phase particles in alloy 2.5 W 0.57 Nb 0 Ti after 1,000 h at 600 °C (upper row) and 650 °C (lower row): (a)+(d) STEM-HAADF image at 200 kV, (b)+(e) Nb and (c)+(f) W mappings.

Intragranular particles preferably show single phase character. Particles after 1,000 h of annealing at 600 °C and 650 °C in alloy 2.5W0.57Nb0Ti, 2.1W0.49Nb0Ti and 18Cr are given in figure 4.10. In direct comparison to particles on the grain boundaries, grain interior particles are smaller (e.g. figure 4.10b) and partially overlap (e.g. figure 4.10a), which make precise chemical analyses impossible. Comparisons of the chemical mappings of particles in figures 4.6, 4.7 and 4.9 show, that the intragranular particles contain the same amounts of W and Nb contrary to the dual phase particles.

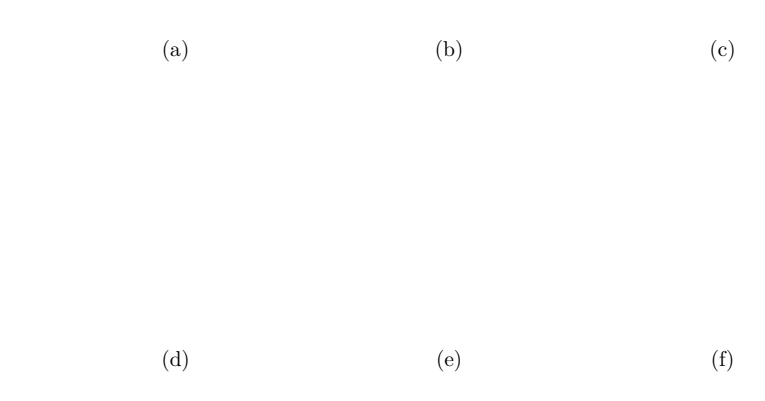


Figure 4.10: Single phase particles in the grain interiors after 1,000 h at 600 °C (upper row) and 650 °C (lower row): (a)+(d) 2.5W0.57Nb0Ti, (b)+(e) 2.1W0.49Nb0Ti (c)+(f) 18Cr.

For in-depth information about the formation and kinetics of the dual phase particles samples were analysed by STEM-HAADF after 10 h of annealing at 650 °C, but detailed analysis of the chemical compositions of the particles failed due to the small particle size in all three alloys. For alloy 2.5W0.57Nb0Ti, as the most creep resistant alloy, analyses at 600 °C were attempted as well, but failed for the same reason. In case of small particles the problem of TEM analysis is related to the ratio of lamella thickness to particle size. If the particle is much smaller than the thickness of the lamella parts of the alloy matrix are analysed during measurement of chemical composition. That means, the smaller the particles, the thinner the lamella has to be. For this reason only element mappings were performed. The element mappings after 10 h of annealing of alloy 2.5W0.57Nb0Ti at 600 °C as well as the mappings done at 650 °C samples for all three alloys are shown in figure 4.11. At 600 °C the measurements show the presence of only one kind of Laves phase in alloy 2.5W0.57Nb0Ti after 10 h of annealing (cf. figure 4.11a-c), which have the same distribution of Nb and W without a formation of a core and shell structure. Due to accelerated kinetics at 650 °C the dual phase particles with a W-rich shell and a core rich in Nb are detected in all alloys after 10 h of annealing (cf. figure 4.11d-l). Thus the formation time of dual phase particles can be reduced to less than 10 h at 650 °C and more than 10 h at 600 °C.

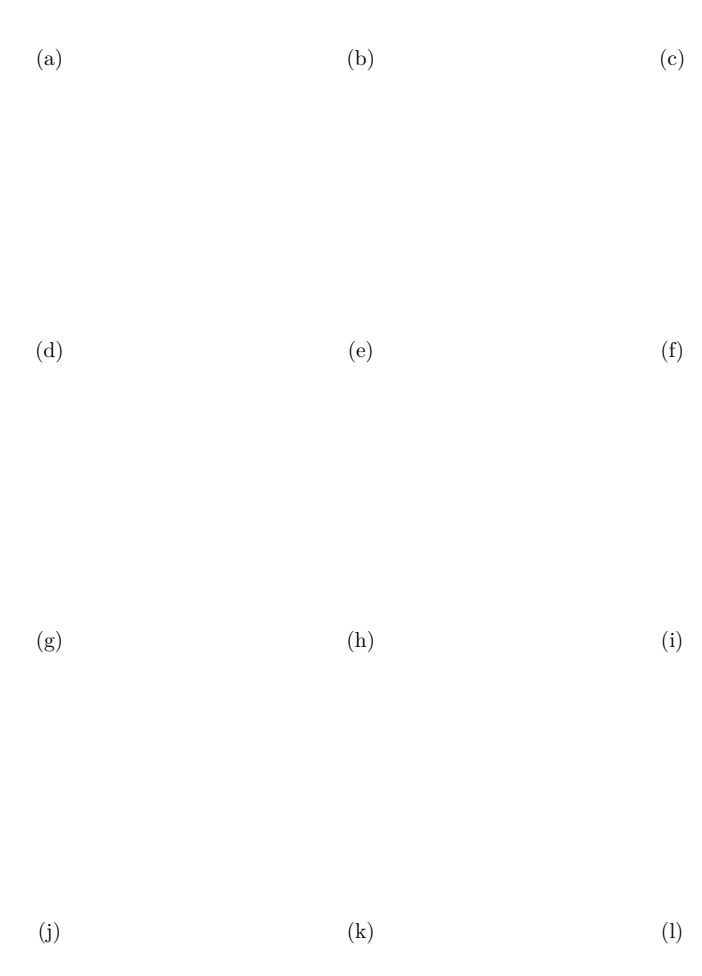


Figure 4.11: Element mappings after 10 h of annealing: Particles in alloy 2.5W0.57Nb0Ti at 600 °C (first row): (a) STEM-HAADF image at 200 kV, (b) mapping of Nb and (c) mapping of W. Mapping at 650 °C after 10 h of annealing: 2.5W0.57Nb0Ti (second row) (d) STEM-HAADF image at 200 kV, (e) Nb and (f) W mappings, 2.1W0.49Nb0Ti (fourth row) (g) STEM-HAADF image at 200 kV, (h) Nb and (i) W mappings and 18Cr (third row) (j) STEM-HAADF image at 200 kV, (k) Nb and (l) W mappings.

After long-term annealing (29,395 h in case of the 18Cr alloy, 37,916 h in case of 2.1W0.49Nb0Ti and 40,789 h for 2.5W0.57Nb0Ti, at 600 °C) no dual phase, but single phase particles were observed. Here an equilibrium state can be assumed. The TEM images of particles found in stress-free head sections of creep specimens are given in figure 4.12. These single phase particles contain W and Nb. Furthermore the absence of LT particles after long-term annealing may indicate ongoing balancing of W between the LT and HT areas in the dual phase particles and the surrounding matrix, which finally may result in particles of an HT-like chemical composition. A representative element mapping for long-term single phase particles at 600 °C is depicted in figure 4.13 (alloy 2.5W0.57Nb0Ti after 40,789 h).

(a) (b)

(c)

Figure 4.12: Single phase particles at the grain boundaries at 600 °C (a) 18Cr (29,395 h) (b) 2.1W0.49Nb0Ti (37,916 h) (c) 2.5W0.57Nb0Ti (40,789 h).

(a) (b) (c)

Figure 4.13: Representative element mappings of single phase particles at the grain boundaries after long-term annealing at 600 °C of alloy 2.5W0.57Nb0Ti: (a) STEM-HAADF image at 200 kV after 40,789 h, (b) mapping of Nb and (c) W.

At the upper limit of the envisaged application temperature range (650 °C) particles from quasi stress-free head sections of creep specimens as well as particles from the stressed gauge length (cf figure 3.1, section 3.2) were analysed and classified. So far, the maximum available long-term annealing times at 650 °C are 6,662 h in case of 18Cr, 8,608 h for the 2.1W0.49Nb0Ti material and 9,808 h for alloy 2.5W0.57Nb0Ti. In case of the 2.5W0.57Nb0Ti an intermediate state after 2,425 h was analysed, too. The images of particles of the quasi stress-free head sections and stressed gauge length sections at 650 °C are depicted in figure 4.14 and 4.15.

In case of 18Cr (cf. figure 4.14a and 4.15a) two different phases were found in the head section. Because of the size of the LT phase no detailed chemical analyses can be performed, but the element mappings confirm the presence of two phases. The element mappings of the particles are shown in figure A.1.1 in the appendix A.1. The presence of two different types of Laves phases agrees with the results by thermodynamic modelling (cf. section 4.3.1). In the gauge length of the 18Cr material the presence of only one phase can be proven. The reason for this may be accelerated balancing caused by lattice deformation of the stressed gauge length. For the 2.1W0.49Nb0Ti material (cf. figure 4.14b and 4.15b), where the modelling predicted only one phase at 650 °C, both phases were found in the head and gauge length sections. After 9,808 h in case of alloy 2.5W0.57Nb0Ti only one phase was found in the head section, while two phases were verified in the gauge length (cf. figure 4.14d and 4.15d). An explanation for this may be the limited size of the lamella and the ongoing balancing between HT and LT phase areas, which reduces the appearance of LT phase areas, whereby the LT is only a minor phase after long-term annealing. After 2,425 h annealing the reverse case can be observed (cf. figure 4.14c and 4.15c). Here both phases were verified in the head section, while only one phase can be found in the gauge length. Therefore the absence of both phases after 9,808 h in the head section in case of alloy 2.5W0.57Nb0Ti cannot be certainly confirmed. The validation of the particles by element mappings for allow 2.1W0.49Nb0Ti and 2.5W0.57Nb0Ti is given in the appendix (cf. section A.1, figures A.1.2, A.1.3 and A.1.4).



Figure 4.14: Particles of the quasi stress-free head sections at 650 °C of (a) 18Cr after 6,622 h, (b) 2.1W0.49Nb0Ti after 8,608 h, (c) 2.5W0.57Nb0Ti after 2,425 h and (d) after 9,808 h.



Figure 4.15: Particles of the stressed gauge length sections at 650 °C of (a) 18Cr after 6,622 h, (b) 2.1W0.49Nb0Ti after 8,608 h, (c) 2.5W0.57Nb0Ti after 2,425 h and (d) after 9,808 h.

All dual-phase particles at 650 °C after long-term annealing as well as the intermediate annealing step after 2,425 h in case of alloy 2.5W0.57Nb0Ti do not show the same pronounced shape with HT-shell and LT-core like the dual-phase particles after 1,000 h of annealing at 600 °C and 650 °C (compare figures 4.5, 4.8, 4.14 and 4.15). This and the absence of an LT phase after long-term annealing at 600 °C indicate ongoing balancing of HT and LT phase areas in the dual particles and the surrounding matrix, which finally may result in particles of an HT-near chemical composition. The results of long-term annealing at 650 °C indicate that an equilibrium state is not yet reached after the maximum available annealing time of 9,808 h (2.5W0.57Nb0Ti), 8,608 h for the 2.1W0.49Nb0Ti and 6,622 h in the 18Cr material and the balancing is not completed. In consideration of solubility of the Laves phase forming elements W,

Nb and Si an explanation for this may be the combination of low solubility of Nb in the ferritic matrix, especially in comparison to W [54, 90–92] and the promoting effect of silicon on the formation of Laves phase particles. This effect was also found relating to (Fe,Cr)₂Mo and Fe₂Nb Laves phase particles [17,93] and suggests that in case of (Fe,Cr,Si)₂(Nb,W) particles, silicon promotes the formation of the Laves phase particles, too. Due to high oversaturation and comparatively fast diffusion of niobium $(D=4.05 \cdot 10^{-20} \text{ m}^2/\text{s} \text{ at } 600 \text{ }^{\circ}\text{C} \text{ and } D=5.04 \cdot 10^{-19} \text{ m}^2/\text{s} \text{ at } 650 \text{ }^{\circ}\text{C} \text{ [94]}) \text{ combined with }$ accelerated diffusion of silicon (D=1.1515 \cdot 10⁻¹⁸ $^{\text{m}^2}/_s$ at 600 °C and D=5.602 \cdot 10⁻¹⁸ $^{\text{m}^2}/_s$ at 650 °C, calculated with thermodynamic database TCFE7) the formation of Nbrich, Si-containing LT particles may be kinetically favoured. In comparison tungsten exhibits low oversaturation and slow diffusion in ferrite (D=1.86 \cdot 10⁻²⁰ m²/_s at 600 °C and D= $2.13 \cdot 10^{-19}$ m²/s at 650 °C [95]), which may result in a prolonged incubation period in case of the precipitation of W-rich HT phase particles. Thus LT particles may already be in the growth regime, while HT particles nucleate. In this case two different, time-shifted growth curves may exist. Hence, the LT Laves phase may be considered to be a metastable phase, which is kinetically preferred at short annealing times. As a result the representation of the LT phase as an equilibrium phase in the recent thermodynamic databases may be deficient. Further in-depth analysis should concentrate on the investigation of very small particles (<10 h of annealing, cf. figure 4.11) and their evolution to finally proof this theory.

The verification of the modelling results by the above presented TEM phase analyses shows a principal agreement regarding phase partitioning. Disagreements between measurements and TC predictions may be explained by the fact that the software is designed for commercial steels and calculates equilibrium phase states of these, where the Laves phase mostly is a minor phase. Nevertheless, the software is considered suitable to generate general information about the effect of particular alloying elements on potential phase formation [37,89]. Optimization of data bases for thermodynamic modelling of Laves phase containing ferritic steels are described in detail in [71].

4.3.3 Chemical Composition at 600 $^{\circ}$ C and 650 $^{\circ}$ C

For detailed chemical composition analyses only particles at the grain boundaries after 1,000 h of annealing at 600 °C and 650 °C were measured. Such particles were sufficiently big in size for chemical analysis by EDX, while most particles in the grain interiors or below 1,000 h remained too small for this purpose (cf. section 4.3.2). As previously mentioned, the analyses confirm the HT-shells to be rich in W and low in Nb content and that the Si content of the HT phase is below the detection limit. In contrast the LT-cores exhibit high Nb and low W contents together with undoubted amounts of silicon. The fact that the tungsten M_{α} -line (1.774 keV) and the K_{α} -line (1.739 keV) of silicon are located closely to each other results in line overlays of the spectra in TEM/EDX analyses, which made the experimental proof of silicon complex in all cases. An example of an element spectrum of an HT and LT phase measurement

to illustrate this problem is given in figure 4.16, where the marked area shows the overlay in the LT phase measurement (cf. figure 4.16 (b)).

(a)

(b)

Figure 4.16: Element spectrum of (a) HT phase and (b) LT phase. The marked area shows the line overlay of the tungsten M_{α} -line and the silicon K_{α} -line (alloy 2.1W0.49Nb0Ti; 600 °C; 1,000 h).

The chemical compositions measured (mean of min. two measurements, where phase area size was sufficient) after different annealing steps were compared with the equilibrium compositions predicted by TC. A comparison of the measured particle and matrix compositions of alloy 18Cr and 2.1W0.49Nb0Ti at 600 °C with the modelling results is given in figure 4.17.



Figure 4.17: Chemical composition at 600 °C after different annealing steps in comparison with calculated (TC) equilibrium compositions: (a) LT, HT phase and (b) matrix of alloy 18Cr (29,395 h; head section). (c) LT, HT phase and (d) matrix of alloy 2.1W0.49Nb0Ti (37,916 h; head section).

Regarding phase partitioning at 600 °C the chemical composition of both phases is in fundamental agreement with the calculated results. Also a W- and Nb-rich phase, which contains Si as well is predicted. The predicted chemical composition could be connected to temperature ranges of stability (cf. figure 4.4a) and are therefore declared as HT and LT phase for technical reasons. Differences between the software predictions and the measured values after mid-term annealing (1,000 h) in case of 2.1W0.49Nb0Ti and 18Cr are not unexpected and may be explained by not reaching the equilibrium state in case of the LT phase in the test alloys, while modelling provides equilibrium compositions. After 1,000 h the values of the HT phase calculation differ significantly from the measurements, what most probably is the result of ongoing balancing between LT phase and HT phase within a dual phase particle (cf. figure 4.17a and c). Especially, the significant differences in Cr and Nb content become obvious. These two elements are particularly misjudged if LT and HT phase are present. After long-term annealing

only the presence of HT Laves phase particles was proven. The chemical composition of the HT phases agrees better with the predicted chemical composition after long-term annealing (29,395 h in case of 18Cr and 37,916 h for alloy 2.1W0.49Nb0Ti). Because of the small deviations from the modelled compositions after long-term annealing concerning the measured results of chromium and niobium, a quasi equilibrium state can be assumed. In case of the 2.1W0.49Nb0Ti material the deviations between measurement and prediction are higher than in case of the 18Cr material, especially in case of Cr. This also can be observed concerning matrix compositions. The evolution of the measured chemical composition of the matrix after mid-term (1,000 h) annealing and long-term annealing (29,395 h in case of 18Cr and 37,916 h for alloy 2.1W0.49Nb0Ti) does not show major changes between the annealing steps (cf. figure 4.17b and d). Because of the low particle size after 1,000 h of annealing at 600 °C the analyses of chemical composition could not be performed in case of alloy 2.5W0.57Nb0Ti (cf. figure 4.8a). The chemical composition of the HT phase after 40,789 h and of the matrix after 1,000 h and 40,789 h are depicted in figure 4.18.

Figure 4.18: Chemical composition of HT phase and matrix at 600 °C after different times of annealing in comparison with TC equilibrium compositions in alloy 2.5W0.57Nb0Ti (head section).

The comparison shows that in case of alloy 2.5W0.57Nb0Ti the composition of the HT Laves phase is in fundamental agreement with the modelled composition with regard to phase partitioning. Like the HT phase in alloys 18Cr and 2.1W0.49Nb0Ti the particles in alloy 2.5W0.57Nb0Ti contain high W and low Nb content (approximately six times larger). In addition the comparison of the HT phase shows discrepancies concerning the niobium and tungsten contents, as well as the chromium content, which is larger in comparison to alloys 2.1W0.49Nb0Ti and 18Cr. The latter even becomes more obvious

comparing the modelling and measured results of the matrix.

At 650 °C the behaviour regarding to phase partitioning persists. Figure 4.19 shows the composition of the head section (HS) particles depicted in figure 4.14 in comparison to gauge length (GL) particles in figure 4.15. In case of HT phase and matrix the compositions only show small variance unlike in case of the LT phase in alloy 2.1W0.49Nb0Ti. The reason for this most probably is accelerated diffusion caused by lattice deformation. Therefore the comparisons between modelling and measurement were performed at the stress-free particle compositions to avoid potential influences of lattice deformation and to enable comparison to mid-term furnace annealed samples. Nevertheless in case of lattice deformation the LT phase shows the aforementioned chemical composition (high Nb and low W content).



Figure 4.19: Comparison of chemical composition at 650 °C of head section and gauge length of alloy (a) 18Cr (6,622 h), (b) 2.1W0.49Nb0Ti (8,608 h), (c) 2.5W0.57Nb0Ti after 2,425 h and (d) 9,808 h.

The chemical composition after mid-term annealing (1,000 h) and of long-term annealed head section particles in comparison to modelled results for all three alloys are given in figure 4.20.

In case of alloy 2.5W0.57Nb0Ti and 2.1W0.49Nb0Ti (cf. figure 4.20c and e) a comparison of the LT phase composition with modelled results is not possible. As mentioned before the predicted dissolution temperature of the LT phase in this alloys lies below 650 °C and thus chemical compositions at 650 °C do not exist in modelling (cf. section 4.3.1). According to previous results the analyses after mid-term annealing and long-term annealing (8,608 h for the 2.1W0.49Nb0Ti material) as well as after the intermediate annealing step of 2,425 h in case of alloy 2.5W0.57Nb0Ti show a silicon containing LT phase rich in niobium. The 2.1W0.49Nb0Ti material shows a significant increase of the Nb content in the LT phase between mid-term and long-term annealing. This can be explained by the fact that in alloy 2.1W0.49Nb0Ti single LT phase particles appear, while in alloy 2.5W0.57Nb0Ti and 18Cr dual phase particles with LT-core and HT-shell character prevail (cf. figure 4.14b), while e.g. the LT phase in allow 2.5W0.57Nb0Ti after the intermediate annealing step of 2.425 h is surrounded by an HT phase shell (cf. figure 4.14c). Therefore the balancing between LT and HT phase may be delayed in case of alloy 2.1W0.49Nb0Ti. For alloy 18Cr chemical analyses of the LT phase could not be performed after long-term annealing (6,622 h), because of the small size of the particle area (cf. figure 4.14a). In consideration of the results after 1,000 h of annealing at 600 °C the composition after 1,000 h at 650 °C regarding LT phase composition do not deviate strongly to the modelled results (compare figure 4.17a and figure 4.20a). This can also be observed in case of the HT phase. Allow 2.5W0.57Nb0Ti is an exception here (cf. figure 4.20c). After 1,000 h and 2,425 h allow 2.5W0.57Nb0Ti exhibits the biggest differences between measurement and modelling. Furthermore an increase in niobium and a decrease in tungsten content becomes obvious comparing the different annealing steps (1,000 h, 2,425 h and 9,808 h), what most probably is the result of progressive balancing between LT phase and HT phase. In all cases the evolution of the matrix composition from mid-term to long-term annealing does not show great changes and better agreement to the modelled results than at 600 °C.

For straight forward description of the differences between predicted and measured chemical compositions, the differences of the LT, HT phases and the matrix are visualised in figure 4.21. Values above zero indicate a value measured higher than modelled. Overestimation by modelling is indicated by values below zero.

The drawback in the modelling obviously is the correct assessment of the role of the Laves phase forming elements Nb and W. In case of the 18Cr batch the Nb and W contents are overestimated by the software at 600 °C and after 1,000 h annealing at 650 °C for the LT phase, while for the HT phase only Nb is overestimated, but W underestimated. The latter can also be observed in case of alloy 2.1W0.49Nb0Ti and 2.5W0.57Nb0Ti. The misassessment is more pronounced in case of Nb, than in case of W. Misassesment after 1,000 h is not unexpected and can be explained by not reaching

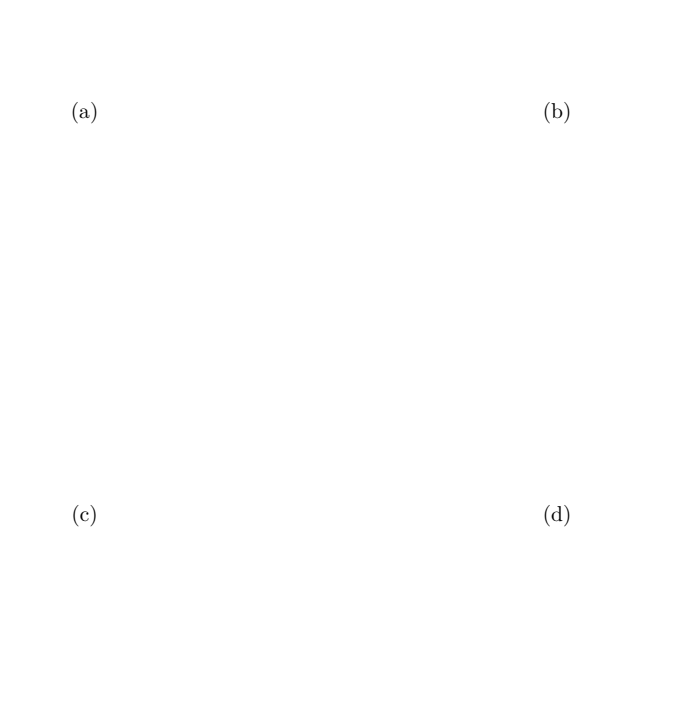


Figure 4.20: Chemical composition at 650 °C after different annealing steps in comparison with TC equilibrium compositions: (a) HT, LT phase and (b) matrix of alloy 18Cr. (c) HT, LT phase and (d) matrix of alloy 2.1W0.49Nb0Ti. (e) HT, LT phase and (e) matrix of alloy 2.5W0.57Nb0Ti.

(f)

(e)

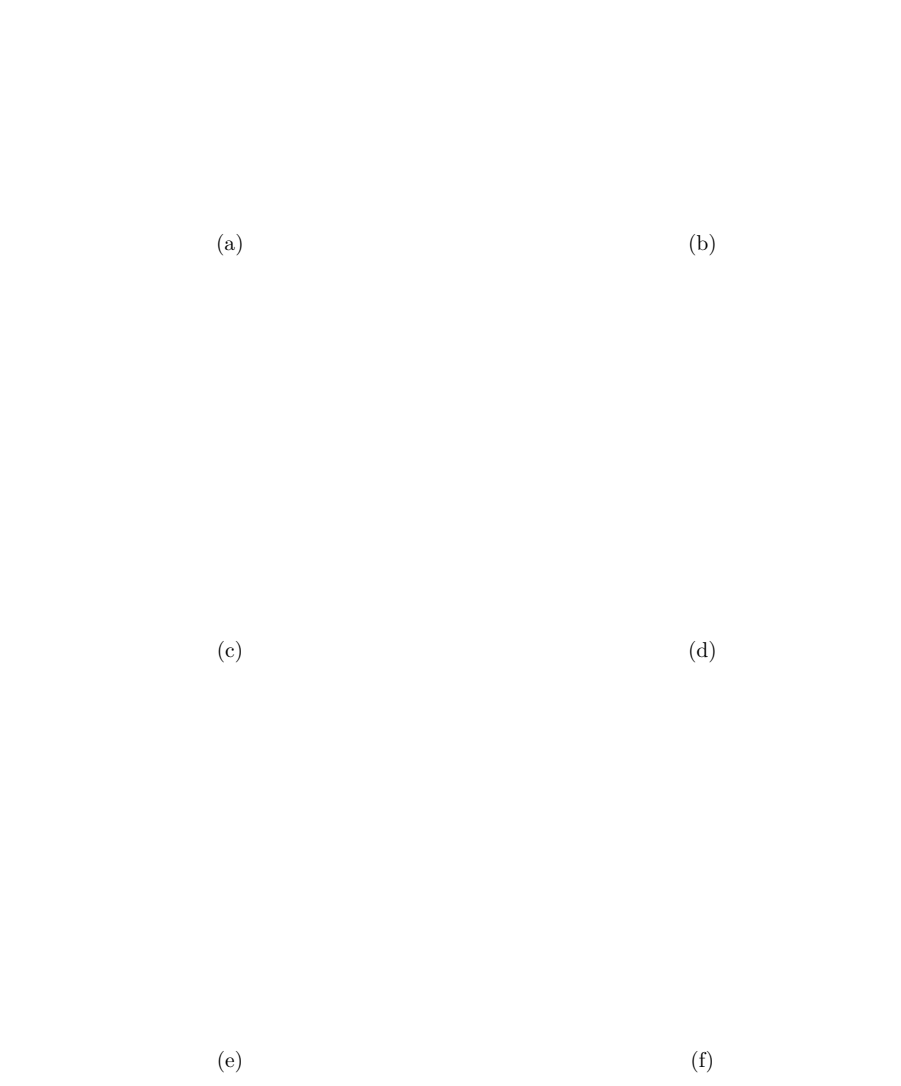
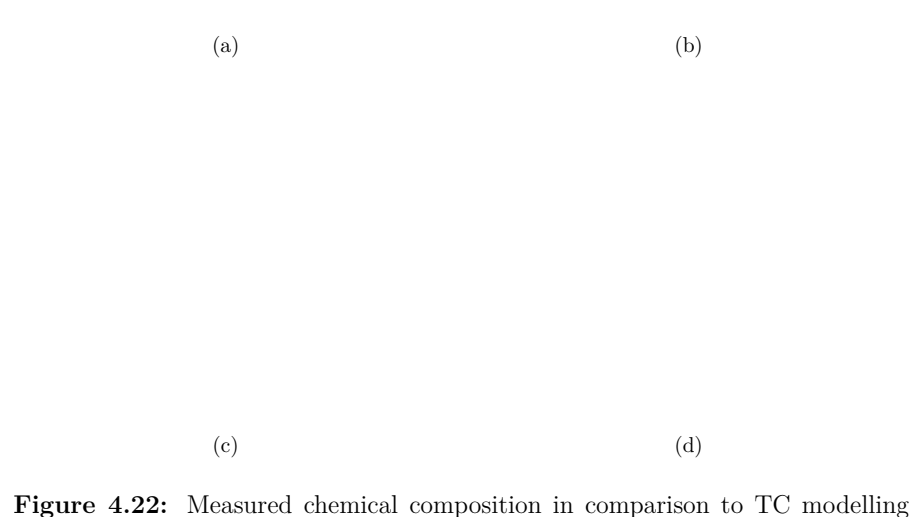


Figure 4.21: Differences in modelled and measured chemical compositions at 600 °C and 650 °C after different annealing steps: (a) HT, LT phase and (b) matrix of alloy 18Cr (head section). (c) HT, LT phase and (d) matrix of alloy 2.1W0.49Nb0Ti (head section). (e) HT phase and (f) matrix of alloy 2.5W0.57Nb0Ti (head section).

equilibrium conditions. Furthermore the chromium content is generally misestimated. Especially at 600 °C the Cr content is underestimated in the phases and in the matrix for all alloys. In case of the matrix the differences are comparatively small and restricted to the underestimation of chromium, to a smaller extent of tungsten and an overestimation of iron. In case of alloy 2.1W0.49Nb0Ti and 2.5W0.57Nb0Ti the deviations are more pronounced than in case of 18Cr steel, especially concerning chromium. Particularly noticeable are misassessments if LT and HT phase both are present. A reason for the misinterpretation of chromium content in the calculations and better agreement in alloy 18Cr may be the presence of the (Fe.Cr)-σ-phase and its varying percentage. The chemical composition of the (Fe,Cr)-σ-phase in alloy 2.1W0.49Nb0Ti and 2.5W0.57Nb0Ti of head section samples annealed at 600 °C and 650 °C is presented in figure 4.22 with the differences between predicted and measured results. In contrast to the calculations (cf. figure 4.4b), the (Fe,Cr)- σ -phase could not be proven in the head section of alloy 18Cr after annealing at 600 °C. Exemplary forescattered electron images of long-term head section samples of alloy 18Cr (29.395 h), 2.1W0.49Nb0Ti (37.916 h) and 2.5W0.57Nb0Ti (40.789 h) at 600 °C are depicted in figure 4.23.

Regarding the (Fe,Cr)-σ-phase the comparison shows a significant misassessment of the chromium and tungsten contents, especially in case of the 2.5W0.57Nb0Ti alloy (compare figure 4.22b and d). A reason for this may be the general misassessment of phase formation: In case of the (Fe,Cr)-σ-phase the software overestimates the amount of chromium at both temperatures and alloys (2.5W0.57Nb0Ti and 2.1W0.49Nb0Ti). This explains the previous results regarding Laves phase and matrix compositions with greatly underestimated chromium contents. In case of tungsten the software underestimates the content in both alloys, which can be also observed in the comparisons of HT and matrix compositions (cf. figure 4.21). Furthermore the (Fe,Cr)-σ-phase consumes a considerable content of W after long-term annealing (approximately 2-4 wt.%, cf. 4.22a and c), which is not available for the formation of Laves phase particles or solid-solution strengthening in the matrix. Further studies should focus on this issue and appropriate optimisation of the chemical alloy composition to minimise (Fe,Cr)-σ-phase formation and thus achieve full exploitation of W.

The outlined differences in the measured and calculated chemical composition, especially in case of the Laves phase forming elements W, Nb and Si demonstrate the demand of more accurate databases. Paired with the misinterpretation of the chemical composition of the (Fe,Cr)- σ -phase, caused by the misassessment of Cr content in this phase as well as in the Laves phase particles and matrix limits the application of the software as a tool for goal orientated, in-depth material development of fully ferritic steels, where accuracy plays a major role. Results of this work could form a basis for new and improved databases.



(a) (b) (c) Figure 4.23: Exemplary forescattered electron images of long-term head section samples at $600~^{\circ}\text{C}$ (a) 18Cr (29,395 h), (b) 2.1W0.49Nb0Ti (37,916 h) and

of alloy (a) 2.5W0.57Nb0Ti and (c) 2.1W0.49Nb0Ti and their differences for (b) 2.5W0.57Nb0Ti and (d) 2.1W0.49Nb0Ti (600 °C; 650 °C; head section).

(c) 2.5W0.57Nb0Ti (40,789 h).

4.3.4 Examination of Phase Structure

Additionally to the analysis of chemical composition described in section 4.3.3, crystal structure analyses by EBSD were performed. The predicted C14 Laves phase structure as the main phase was confirmed. However, besides the Laves phase particles, another phase rich in niobium was detected. This minor phase exhibits a cubic Fe_3Nb_3N structure (SG: Fd3m; No. 227) and contains nitrogen. So far, this phase was only found at the grain boundaries of the long-term creep specimens. Figure 4.24 shows an EBSD phase map superimposed with a band contrast image obtained from alloy 2.5W0.57Nb0Ti after 40,789 h of annealing at 600 °C (head section). The associated element mappings of Nb, W and N are given in figure 4.25.

Figure 4.24: EBSD phase map (superimposed with band contrast image) of alloy 2.5W0.57Nb0Ti after 40,789 h at 600 °C.



Figure 4.25: Element mappings after 40,789 h at 600 °C in alloy 2.5W0.57Nb0Ti: (a) Nb, (b) W and (c) N.

The element mappings confirm that only in the areas designated as Fe_3Nb_3N phase nitrogen was detected (compare figure 4.24 and 4.25c). Also in these areas the greatest amount of niobium was found.

Due to the similarity to the cubic C15 Laves phase (also SG: Fd3m; No. 227; cf. section 2.3.2) it is difficult to distinguish between the Fe_3Nb_3N and C15 Laves phase structure. In border regions of the cubic phase with and without nitrogen reliable distinction cannot be assured. An example from alloy 2.1W0.49Nb0Ti after 8,608 h at 650 °C is given in figure 4.26 (associated element mappings of Nb, W and N in figure 4.27). Here the high niobium containing area is bigger than the nitrogen containing area (compare figure 4.27a and c). Nevertheless the whole high niobium containing area has a cubic crystal structure, which makes it more complicated to distinguish between Fe_3Nb_3N and C15 Laves phase structure.

Figure 4.26: EBSD phase map (superimposed with band contrast image) of alloy 2.1W0.49Nb0Ti at 650 °C after 8,608 h.

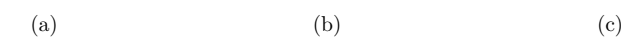


Figure 4.27: Element mappings after 8,608 h at 650 °C from alloy 2.1W0.49Nb0Ti: (a) Nb, (b) W and (c) N.

The Fe₃Nb₃N particles are structurally similar to the intermetallic Fe₂Nb₃ particles (also SG: Fd3m; No. 227) in an experimental steel with 19 wt.% of chromium [96]. This steel bases on the commercial ferritic stainless steel 1.4521 for applications above 950 °C and is strengthened by intergranular Fe₂Nb₃ compounds. The stability range of these compounds lies between 650 °C and 1050 °C.

As mentioned before the Fe_3Nb_3N particles are a minor phase only in these alloys and were not found in case of alloy 2.5W0.57Nb0Ti at 650 °C after 9,808 h, 2.1W0.49Nb0Ti at 600 °C after 37,916 h nor in case of alloy 18Cr at both temperatures after 29,395 h or 6,622 h. The EBSD phase maps are given in figure 4.28, the associated element mappings of Nb, W and N in figure 4.28 in appendix 4.28.

The influence of nitrides with Fe₂Nb₃ structure on strength properties is not in the focus of this work, but should be investigated in further studies. Additionally future investigations should focus on a potential influence on C14 Laves phase particle formation, because both particles types require Nb.

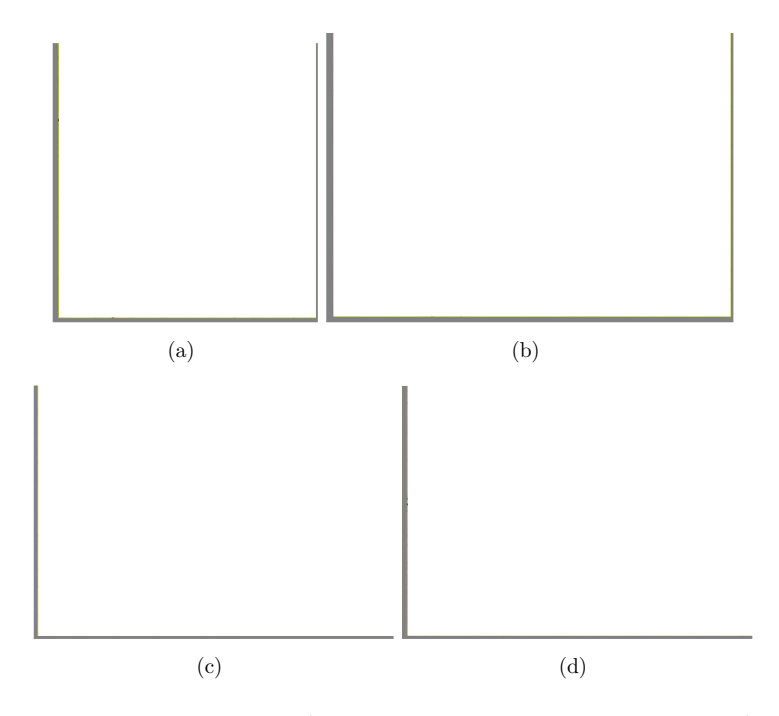


Figure 4.28: EBSD phase map (superimposed with band contrast image) of alloy (a) 2.5W0.57Nb0Ti at 650 °C (9,808 h), (b) 2.1W0.49Nb0Ti at 600 °C (37,916 h) and (c) 18Cr at 600 °C (29,395 h) and (d) at 650 °C (6,622 h).

In addition to EBSD analyses diffraction investigations regarding dual phase particle orientation were performed. The investigations under different sample tilting were done by the Department of Metallurgy and Ceramics Science of the Tokyo Institute of Technology in Japan. A Jeol 2010 microscope with an acceleration voltage of 200 kV (camera length: 80 cm) was used. The diffraction patterns for the Burgers vector direction $\vec{b} = (10\bar{1}0)$ of a dual phase particle in alloy 2.1W0.49Nb0Ti after 1,000 h of annealing at 650 °C are given in figure 4.29. Measurements were obtained from the HT-shell (cf. figure 4.29a) and the LT-core (cf. figure 4.29c). Both measurements

generate similar diffraction patterns without spreading diffraction reflexes (compare figure 4.29b and d). Furthermore all results show that the crystal orientations of the HT and LT phases are equal with a coherent intermediate phase boundary. Additional results of the measurements with Burgers vector direction $\vec{b} = (11\bar{2}0)$ are given in figure A.2.9 in appendix A.2.2.

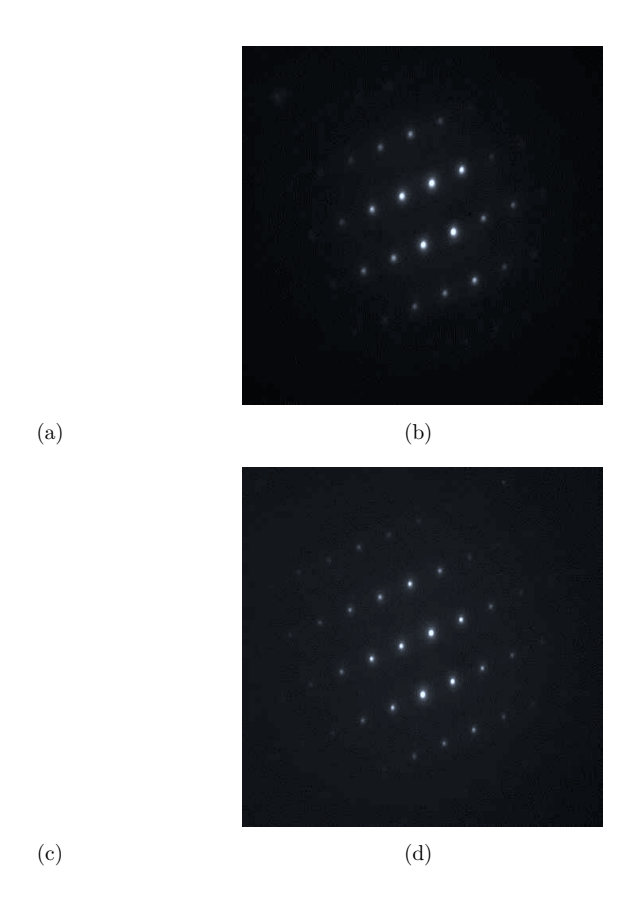
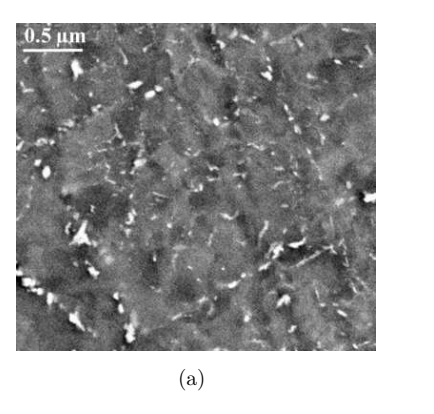


Figure 4.29: Selected area diffraction investigations in alloy 2.1W0.49Nb0Ti after 1,000 h of annealing at 650 °C: (a) TEM image taken at 200 kV with HT-shell and (b) diffraction pattern of the selected area. (c) TEM image taken at 200 kV with LT-core and (b) diffraction pattern of the selected area ($\vec{b} = (10\bar{1}0)$).

4.4 Particle Evolution at 600 °C and 650 °C

Analysis of the particle diameter evolution gives an estimation of the stability of the strengthening Laves phase particles during service. Therefore HR-SEM images, which were partially examined in the context of other studies [87,97], were processed and

analysed (cf. section 3.3.1). Only intragranular particles were taken into account for the evolution of the median particle diameter (cf. section 4.4.1) as well as the particle size distribution (cf. section 4.4.2). Grain boundary particles as investigated for chemical analysis exhibit progressed coarsening and are therefore not representative for particle size evolution. Initial investigations of the particle evolution up to 1,000 h were presented in [97], but had to be optimized regarding particle evaluation criteria (cf. section 3.3.1) and appropriated selection of image magnification. Figure 4.30a and b show extracts of an HR-SEM image of 2.5k-fold magnification and particle detection in this area by means of AnalysisPro ®, while 4.30c and d show the same sample area with 10k-fold magnification. The colours of the detected particles stand for the size class of the particles: red=10-30 nm, green=30-50 nm, blue=30-70 nm and yellow=70-100 nm.



(b)

(c) (d)

Figure 4.30: HR-SEM image extract of the same area: (a) 2.5k-fold magnification (original image) and (b) after processing and particle detection. (c) 10k-fold magnification (original image) and (d) after processing and particle detection (alloy 18Cr, $600\,^{\circ}\text{C}$, 2 h).

Direct comparison of the detected particles in figures 4.30b and d elucidate the differences caused by the magnification: Strong differences become obvious by the comparison of the size classes 10-30 nm and 30-50 nm (red and green). In case of the lower magnification less particles were detected and the particles were detected to be smaller. This also can be observed in the size class 30-70 nm (blue). The class 70-100 nm (yellow) does not indicate strong differences. Therefore 10k-fold magnification was used in order to better resolve particles in the size range from 10 to 70 nm to ensure more accurate evaluation of very small particles, that are usually found in the very short-term annealing samples (up to 30 h). In general less particles were taken into account in case of the higher magnification for the classification, caused by the smaller extract of the image. However, these particles were detected with a higher precision in the smaller size classes. The number of particles which were considered for the evaluation of particle size evolution are given in table B.1 and B.2 in appendix B.

4.4.1 Particle Diameter Evolution

To reveal the particle evolution the median was chosen, because it takes the size distribution of the particles into account. The median considers that in general the alloys contain more smaller than bigger particles, which would be underrepresented if the mean diameter was chosen. Table 4.1 and 4.2 give an overview of the median particle diameter evolutions in the 2.5 W 0.57 Nb 0 Ti, 2.1 W 0.49 Nb 0 Ti and 18 Cr trial alloys at 600~C and 650~C.

Table 4.1: Median and variance of the particle diameters (in nm) in the 2.5W0.57Nb0Ti, 2.1W0.49Nb0Ti and 18Cr alloys at 600 °C (NA:= Not available for this time).

	2.5 W0.57 Nb0 Ti	2.1 W0.49 Nb0 Ti	18Cr
2 h	30 ± 0.3	33 ± 0.5	31 ± 0.5
100 h	42±1.2	45±1.0	46±1.0
1,000 h	41 ± 1.0	41 ± 1.0	40 ± 0.8
26,032 h	53 ± 6.0	NA	NA
29,395 h	NA	NA	60 ± 8.0
37,916 h	NA	66±8.0	NA
40,789 h	60±11.0	NA	NA

Table 4.2: Median and variance of the particle diameters (in nm) in the 2.5W0.57Nb0Ti, 2.1W0.49Nb0Ti and 18Cr alloys at 650 °C (NA:= Not available for this time).

	2.5W0.57Nb0Ti	2.1W0.49Nb0Ti	18Cr
2 h	48±0.9	42±0.9	45±1.0
30 h	NA	31 ± 0.6	NA
100 h	45 ± 2.6	45 ± 2.3	56 ± 4.8
1,000 h	53 ± 2.1	49 ± 1.9	43 ± 1.6
2,425 h	62 ± 6.5	NA	NA
2,500 h	NA	NA	87 ± 9.2
2,579 h	NA	67 ± 6.4	NA
6,622 h	NA	NA	112±16.0
8,608 h	NA	85±12	NA
9,808 h	78±11.9	NA	NA

At 600 $^{\circ}$ C all alloys displayed rapid particle growth in the short-term (up to 100 h annealing). This diameter growth is followed by a kink in case of alloy 2.1W0.49Nb0Ti and

18Cr or a rather constant diameter in alloy 2.5W0.57Nb0Ti in the mid-term (1,000 h annealing). Besides expected, pronounced particle coarsening in comparison to 600 °C a similar behaviour can be observed at 650 °C, but the observed kink already appears in the very short-term. In case of alloy 2.5W0.57Nb0Ti it is noticeable after 100 h, in the 2.1W0.49Nb0Ti material after 30 h. In the 18Cr alloy the kink appears after 1,000 h. These observations support the consideration of two parallel, but time-shifted growth processes which were described in section 4.3.2. Due to shifted nucleation of small W-rich HT-phase particles the median diameter may decrease slightly or remain almost constant between 100 h and 1,000 h.

Regarding the particle diameter at 600 °C alloy 2.5W0.57Nb0Ti showed the most stable particles in the long-term, 53 ± 6.0 nm after 26,032 h and 60 ± 11.0 nm after 40,789 h, which is also apparent at 650 °C. Between intermediate (2,425 h) and long-term (9,808 h) annealing the change is comparatively small (62 ± 6.5 nm and 78 ± 11.9 nm), while in alloy 2.1W0.49Nb0Ti and 18Cr the changes are larger (67 ± 6.4 nm after 2,579 h and 85 ± 12 nm after 8,608 h in case of alloy 2.1W0.49Nb0Ti and 87 ± 9.2 nm after 2,500 h and 112 ± 16.0 nm after 6,622 h in case of alloy 18Cr). Within the range of scatter the particle size remains constant for times beyond 26,032 h (600 °C) or 2,425 h (650 °C) respectively, what either indicates slow coarsening of existing particles or subsequent dynamic nucleation of new particles over time.

Especially the comparison of alloys 2.5 W 0.57 Nb 0 Ti and 18 Cr indicates favourable particle stability in alloy 2.5 W 0.57 Nb 0 Ti. While the median particle diameter in alloy 18 Cr is 60 ± 8.0 nm after 29,395 h (rupture time of the respective creep specimen was 29,399 h, cf. section 4.1), particles in the same size range are predominant in alloy 2.5 W 0.57 Nb 0 Ti after approx. 10,000 h longer annealing at 600 °C (60 ± 11.0 nm after 40,789 h). This behaviour sustains at 650 °C. After 9,808 h in case of alloy 2.5 W 0.57 Nb 0 Ti the particles can be found to be in the range of 78 ± 11.9 nm while the particles in alloy 18 Cr are in the range of 112 ± 16.0 nm after approx. two thirds of the annealing time (6.622 h).

The median particle diameter of alloy 2.1W0.49Nb0Ti ranges at both temperatures slightly higher than in alloy 2.5W0.57Nb0Ti (66 ± 8.0 nm after 37,916 h at 600 °C and 85 ± 12 nm after 8,608 h at at 650 °C).

The aforementioned differences in diameter evolution may be partly attributed to the differences in the growth kinetics of the strengthening Laves phase particles and thus may explain the encountered differences in creep behaviour (for further discussion see section 4.4.2).

4.4.2 Evolution of Particle Size Distribution

To enable detailed quantitative statements on the stability of the Laves phase particles during service the equivalent circle diameter (ECD) size distribution of the precipitates at 600 $^{\circ}$ C and 650 $^{\circ}$ C after short-, mid- and long-term annealing was analysed. The annealing times for alloy 2.5W0.57Nb0Ti, 2.1W0.49Nb0Ti and 18Cr and the sample

sources are given in table 3.2, section 3.2. For direct comparison of all time steps samples were taken from the quasi stress-free head sections of creep specimens (cf. figure 3.1, position 1). The ECD size evolution of all three alloys at 600 °C and 650 °C is given in figure 4.31 (associated values are given in tables 4.3, 4.4 and 4.5). All plots show the size classification of the Laves phase particles in the grain interiors, relating the area occupied by Laves phase particles within the individual size classes to the overall area covered by all the Laves phase particles. The size classification is subclassified into nine classes: 10-30 nm, 30-50 nm, 50-70 nm, 70-100 nm, 100-150 nm, 150-200 nm, 200-300 nm, 300-500 nm and 500-1,000 nm. It should be borne in mind that every bar displays an aforementioned size range. For easier comparison between the temperatures cf. figure 4.32. In this presentation type every dot or square represents an aforementioned subclass. For plotting purposes the mean of every size class was taken. At 600 °C alloy 2.5W0.57Nb0Ti possesses reasonably more small particles than the 18Cr or 2.1W0.49Nb0Ti material after short-term annealing (2 h) with subsequent particle coarsening up to 1,000 h in all alloys. The particles mainly range around 60 nm in all the cases and show a relatively symmetric distribution around this peak after 100 h and 1,000 h. After 2 h in case of all alloys as well as after 30 h in the 2.1W0.49Nb0Ti material at 650 °C the particles show pronounced growth. Most of the particles can be found in the range of 30-70 nm at 650 °C, while after 2 h annealing most particles range between 10-50 nm at 600 °C (cf. figure 4.32). In case of alloy 2.5W0.57Nb0Ti and 2.1W0.49Nb0Ti the particle distributions show two main peaks with particles around 85 nm and 125 nm after 100 h, which remain after 1,000 h of annealing. In the 18Cr material the particles exhibit particularly pronounced coarsening and range around 125 nm after 100 h of annealing, while most particles range at around 85 nm after 1,000 h. This explains the strong increase after 100 h with subsequent decrease of the median in this alloy (cf. table 4.2). The behaviour of the particle size evolution up to 1,000 h may be interpreted as another indication for early nucleation and subsequent coarsening of the LT phase particles and delayed nucleation of HT particles. The differences in kinetics of these two processes may distort the particle diameter evolution, which results in kinks or rather constant diameter evolution during annealing up to 1,000 h (cf. section 4.4.1).

After 26,032 h at 600 °C (alloy 2.5W0.57Nb0Ti) the majority of the particles ranges around 125 nm, while alloy 18Cr shows more coarsened particles after 29,395 h (maximum peak at around 275 nm). Analysis of the long-term samples at 600 °C show that a particle size of around 250 nm is not reached before approx. 38,000 h in alloy 2.1W0.49Nb0Ti and 40,789 h in the 2.5W0.57Nb0Ti material.

This pronounced coarsening in case of alloy 18Cr can be observed at 650 °C as well. After the intermediate annealing step of 2,500 h most particles range around 250 nm in the 18Cr material. In comparison the majority of particles in alloy 2.5W0.57Nb0Ti and 2.1W0.49Nb0Ti can be found in the size range from 100 to 150 nm after approx. 2,500 h. Almost the same particle distribution like in alloy 18Cr after 2,500 h (cf. figure 4.32c, purple line) foremost after 8,608 h in case of alloy 2.1W0.49Nb0Ti or even

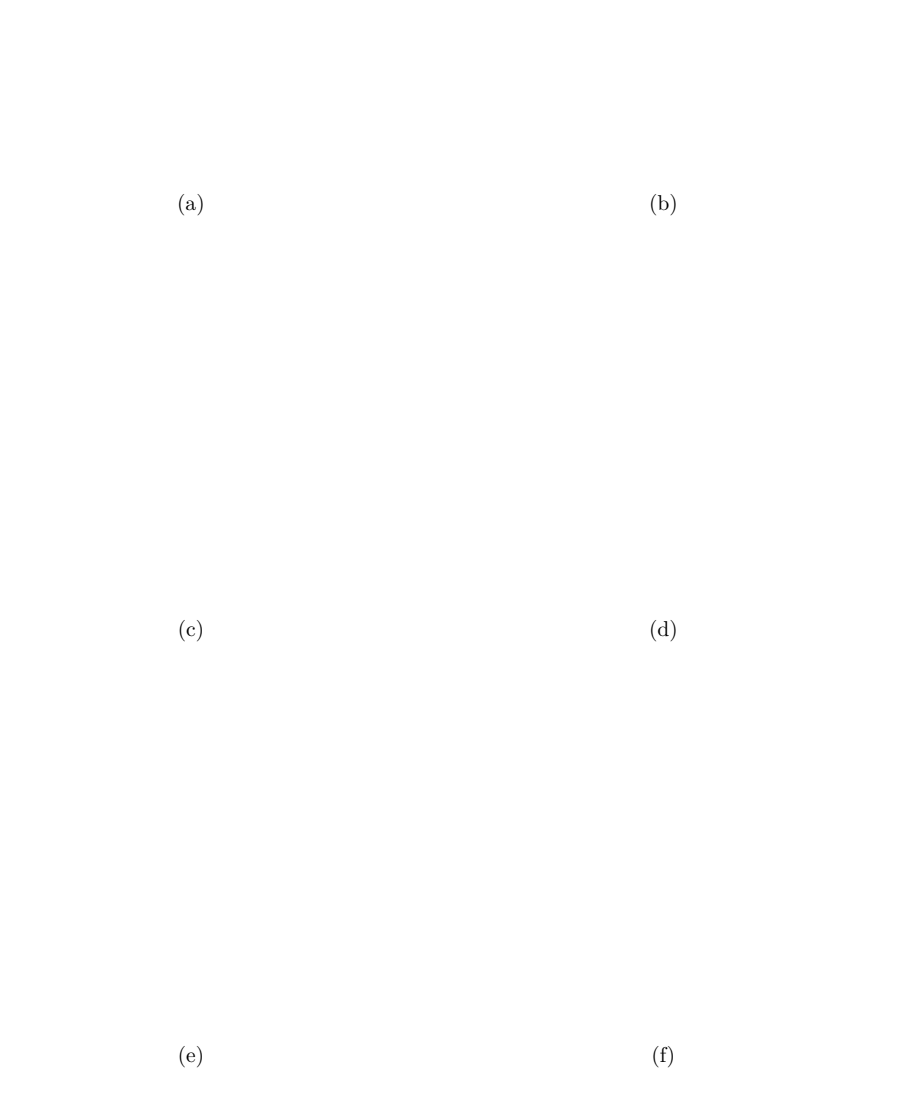


Figure 4.31: Development of particle size distribution in terms of equivalent circle diameter (ECD) at 600 °C (left column) and 650 °C (right column) for (a)+(b) 2.5W0.57Nb0Ti, (c)+(d) 2.1W0.49Nb0Ti and (e)+(f) 18Cr (based on [37,89]).

Table 4.3: Associated particle size distribution values of alloy 2.5 W 0.57 Nb 0 Ti at 600 °C and 650 °C after different annealing times and size classes in % (cf. figure 4.31a and b).

(a) 600 °C

	2 h	100 h	1,000 h	26,032 h	40,789
10-30 nm	42.94	9.99	10.29	2.36	1.59
30-50 nm	32.74	30.19	31.23	7.15	4.84
50-70 nm	4.65	34.43	32.06	9.68	6.63
70-100 nm	0.87	21.72	23.1	15.91	11.69
100-150 nm	0	3.44	3.32	26.3	20.97
150-200 nm	0	0.23	0	20.02	19.06
200-300 nm	0	0	0	15.28	26.72
300-500 nm	0	0	0	3.28	8.49
500-1,000 nm	0	0	0	0	

(b) 650 °C

	2 h	100 h	1,000 h	2,425 h	9,808 h
10-30 nm	7.27	5.07	3.95	1.55	0.71
30-50 nm	51.55	14.15	13.14	4.97	2.92
50-70 nm	41.13	17.82	18.33	7.28	5.09
70-100 nm	17.77	25.71	26.86	13.47	9.6
100-150 nm	1.08	24.78	29.41	23.56	19.42
150-200 nm	0	9.47	8.31	20.65	18.87
200-300 nm	0	2.14	0	19.79	21.98
300-500 nm	0	0.86	0	8.74	17.49
500-1,000 nm	0	0	0	0	3.92

9,808 h in the 2.5W0.57Nb0Ti material (cf. figure 4.32a+b, orange line). In direct comparison and in consideration of the particle diameter in the 18Cr steel the 2.5W0.57Nb0Ti material generally exhibits equal (1,000 h) or more small particles (10–50 nm) over the whole analysed duration at 600 °C. This can also be observed at 650 °C except of the time steps 2 h and 1,000 h. Here the 18Cr alloy exhibits more small particles than the 2.5W0.57Nb0Ti material. This different behaviour after 1,000 h may also be related to possible differences in kinetics of LT and HT phase, which have the greatest influence on the results after 100 h and 1,000 h, as mentioned beforehand. The trend of alloy 2.5W0.57Nb0Ti to obtain smaller particles over the whole duration, especially in the long-term, indicates improved particle stability and/or dynamic precipitation processes and can be considered to be the reason for the

superior creep performance (cf. section 4.1 and [1]) in comparison to alloy 18Cr. The difference in creep performance of the 2.5W0.57Nb0Ti and 2.1W0.49Nb0Ti material cannot be explained on the basis of particle evolution alone. In the long-term both alloys show similar distributions (cf. figure 4.32, orange lines). But in contrast to alloy 2.1W0.49Nb0Ti the 2.5W0.57Nb0Ti material exhibits lower primary creep strain (cf. figure 4.1). This might be considered to be the main reason for the superior creep behaviour of alloy 2.5W0.57Nb0Ti. To prove this further investigations of initial dislocation density should be performed in the future.

Table 4.4: Associated particle size distribution values of alloy 2.1W0.49Nb0Ti at 600 °C and 650 °C after different annealing times and size classes in % (cf. figure 4.31c and d).

(a) 600 °C

	2 h	100 h	1,000 h	37,916
10-30 nm	26.72	7.38	8.97	1.3
30-50 nm	51.27	28.12	24.73	4.35
50-70 nm	18.98	25.26	26.34	6.17
70-100 nm	3.03	23.62	25.62	11.52
100-150 nm	0	5.05	12.68	22.12
150-200 nm	0	0.47	1.66	19.33
200-300 nm	0	0	0	24.08
300-500 nm	0	0	0	9.64
500-1,000 nm	0	0	0	1.48

(b) 650 °C

	2 h	30 h	100 h	1,000 h	2,579 h	8,608 h
10-30 nm	12.83	15.91	5.7	4.72	1.28	0.56
30-50 nm	39.43	27.05	16.77	15.63	4.63	2.67
50-70 nm	37.73	28.92	19.99	20.19	7.46	4.92
70-100 nm	10.01	24.16	22.9	27.33	12.9	10.06
100-150 nm	0	3.96	21.18	25.62	26.25	20.87
150-200 nm	0	0	10.56	5.95	21.8	20.31
200-300 nm	0	0	2.89	0.56	19.83	25.47
300-500 nm	0	0	0	8.74	5.85	13.49
500-1,000 nm	0	0	0	0	0	1.65

(a)

(b)

(c)

Figure 4.32: Temperature comparison of particle size distribution in terms of equivalent circle diameter (ECD) at 600 °C (dashed lines) and 650 °C (solid lines) for (a) 2.5W0.57Nb0Ti, (b) 2.1W0.49Nb0Ti and (c) 18Cr (based on [37,89]).

Table 4.5: Associated particle size distribution values of alloy 18Cr at 600 $^{\circ}$ C and 650 $^{\circ}$ C after different annealing times and size classes in % (cf. figure 4.31e and f).

(a) 600 °C

	2 h	100 h	1,000 h	29,395
10-30 nm	33.17	7.84	11.02	1.72
30-50 nm	51.01	33.81	30.06	4.92
50-70 nm	13.12	36.2	29.07	7.23
70-100 nm	1.63	19.57	22.01	12.04
100-150 nm	1.07	2.58	7.84	21.45
150-200 nm	0	0.47	0	19.36
200-300 nm	0	0	0	23.41
300-500 nm	0	0	0	9.87
500-1,000 nm	0	0	0	0

(b) 650 °C

	2 h	100 h	1,000 h	2,500 h	6,622 h
10-30 nm	11.02	2.35	7.44	0.58	0.3
30-50 nm	39.81	6.87	21.82	2.48	1.07
50-70 nm	37.23	10.02	20.53	4.34	2.63
70-100 nm	10.29	16.45	26.79	9.84	6.3
100-150 nm	1.65	31.1	18.88	21.19	16.08
150-200 nm	0	21.93	2.41	22.17	19.64
200-300 nm	0	10.88	0.83	28.47	26.64
300-500 nm	0	0.4	1.30	10.92	15.87
500-1,000 nm	0	0	0	0	11.47

Additionally to time and temperature, mechanical stress might have a significant influence on the growth of strengthening precipitates [98]. In section 4.3.3 (cf. 4.19) it was mentioned that mechanical stress influences the composition of grain boundary particles, especially in case of the metastable LT phase. Therefore comparisons between stress-free head section particles and stressed gauge length particles in the grain interior were performed to rate this influence. The comparisons at 650 °C (upper limit of the envisaged application temperature) at different stress levels (70 MPa, 100 MPa and 145 MPa) are given in figure 4.33 and 4.34. For straight forward description of the stress influence on coarsening the visualization is shown in particle number fraction (relating all detected Laves phase particles). Like before every data point represents an aforementioned size class.

At the lower stress level (70 MPa) the comparisons of the number fraction between head section and gauge length particles of alloy 2.5W0.57Nb0Ti (9,808 h) and the 2.1W0.49Nb0Ti material (8,608 h) show a decrease of particles smaller than 50 nm (cf. figure 4.33a and b). The reason might be increased diffusion in the strained gauge section and thus accelerate coarsening of small particles. In case of the 18Cr material this phenomenon cannot be observed. Here no significant differences in the size class \leq 50 nm occur, which remains also in the larger size classes. This might be caused by the comparatively short duration of the creep test until rupture of this sample (6,622 h) and the fact, that the coarsening period might not even have been reached. In case of alloy 2.5W0.57Nb0Ti and 2.1W0.49Nb0Ti the variance between head section and gauge length particle number fraction is \leq 5%. The moderately pronounced coarsening, caused by increased diffusion in the strained gauge section indicates that the particles are stable under the influence of superimposed mechanical stress.

(a) (b)

(c)

Figure 4.33: Comparison of stress-free and stressed particle number fraction at 70 MPa: (a) 2.5W0.57Nb0Ti after 9,808 h, (b) 2.1W0.49Nb0Ti after 8,608 h and (c) 18Cr after 6,622 h (based on [89]).

In case of mid stress (100 MPa) creep tests for the 2.5W0.57Nb0Ti material and alloy 2.1W0.49Nb0Ti (cf. figure 4.34a and b) and a high stress (145 MPa) test for alloy 2.1W0.49Nb0Ti (cf. figure 4.34c) the variance between head section and gauge length particle number fraction is $\leq 2\%$. These samples ruptured after comparatively short times (approx. 2,500 h at 100 MPa and after 30 h at 145 MPa). Similar to the particles in the 18Cr sample at 70 MPa the particles in the aforementioned samples might mainly remain in state shortly after growth. Due to the short duration no significant coarsening is conspicuous.

(a) (b)

(c)

Figure 4.34: Comparison of particle number fraction in stress-free head sections and stressed gauge lengths at 100 MPa: (a) 2.5W0.57Nb0Ti after 2,425 h, (b) 2.1W0.49Nb0Ti after 2,579 h and (c) at 145 MPa, 2.1W0.49Nb0Ti after 30 h.

4.5 Summary and Conclusion: Particle Verification and Evolution

Investigation of Laves phase particles in various fully ferritic, high chromium steels shows that the results obtained from TEM investigations could only be verified partly by commercially available thermodynamic modelling software. The presence of an HT and LT Laves phase, which occur as dual phase particles at the grain boundaries, was in principle confirmed at the limits of the envisaged application temperature range of 600 °C to 650 °C for alloy 18Cr at short ageing durations up to 1,000 h as well as for alloy 2.1 W 0.49 Nb 0 Ti at $600 \,^{\circ}\text{C}$. In case of the 2.5 W 0.57 Nb 0 Ti material in general and alloy 2.1W0.49Nb0Ti at 650 °C the LT Laves phase was confirmed as well, but not assessed by modelling. TEM measurements show the presence of dual phase particles already after 10 h of annealing at 650 °C. Furthermore no orientation differences between both phases in dual phase particles were found. Comparisons of the modelled and the measured chemical compositions of particles of sufficient size (after 1,000 h of annealing) are in reasonable agreement regarding general phase composition of LT and HT phase. Composition differences can be explained by not reaching equilibrium conditions after short-term annealing. After long-term annealing at 600 °C (shortest annealing time approx. 30,000 h) only single phase particles with an HT like composition (e. g. 0.37 wt.% Si; 11.19 wt.% Cr; 37.01 wt.% Fe; 9.39 wt.% Nb; 41.67 wt.% W for alloy 2.1W0.49Nb0Ti after 37,916 h of annealing) were found, which agree better with the modelled compositions (0.27 wt.% Si; 6.71 wt.% Cr; 35.55 wt.% Fe; 13.85 wt.% Nb; 43.56 wt.% W). In this case conditions near the equilibrium can be assumed. At 650 °C (shortest annealing time approx. 6,600 h) both phases are still detectable in all alloys, but not mandatory as dual phase particles and only with unincisive LT phase areas. This shows the metastable nature of the LT Laves phase, which underlies specific mechanisms of formation and dissolution. All comparisons between the measured and modelled compositions of Laves phase particles as well as the (Fe,Cr)σ-phase show significant discrepancies especially in chromium, niobium and tungsten content. Therefore the suitability of recent thermodynamic modelling tools regarding goal oriented alloy optimization is doubtful and consequently show the demand of an advanced database for this kind of material. Furthermore the (Fe,Cr)-σ-phase consumes a considerable amount of W, which is not available for the formation of Laves phase particles or solid-solution strengthening in the matrix. Further studies should focus on minimisation of (Fe,Cr)-σ-phase formation and thus full exploitation of W. Structural analyses confirm the presence of Nb-rich nitrides beside the C14 Laves phase, which is difficult to distinguish from the cubic C15 Laves phase. This minor phase occurs preferentially at grain boundaries and possible implications for microstructural and mechanical stability should be focus of further investigations. Particle size evolution analyses show higher particle stabilities in the materials 2.5W0.57Nb0Ti and 2.1W0.49Nb0Ti, which explains the superior creep performance of these materials in

comparison to alloy 18Cr. Additionally the 2.5W0.57Nb0Ti material exhibit lower primary creep strain, which may be considered to be the main reason for its superior creep performance. Comparisons of stress-free head section and stressed gauge length particle evolution indicates that the particles are stable under the influence of superimposed mechanical stress.

4.6 Microstructure Evolution at 650 °C

Previous particle analyses indicate a likely reason for the different creep behaviour of the trial alloys, but did not provide information about potential failure mechanisms. Therefore detailed microstructural investigations were performed. The representative microstructural evolution after different annealing times of alloy 2.5W0.57Nb0Ti as the most creep resistant alloy is given in figure 4.35.

Besides expected particle coarsening, which was discussed in sections 4.4.1 and 4.4.2, the images show formation and dissolution of sub-grain structures as well as the formation of particle-free zones (PFZs).

4.6.1 Sub-Grain Structure Evolution

Observation after different annealing times show the formation of distinct sub-grain structures. These structures are the result of the preceding hot-rolling process. This is confirmed by figure 4.35a, which displays the as received state (0 h annealing) directly after the hot-rolling process. Here sub-grain structures and high-angle grain boundaries are occasionally decorated by precipitates. Up to 1,000 h of annealing (cf. figure 4.35b-d) both grain boundary types were increasingly occupied by precipitates. The coarsening of high-angle boundary particles remain after 2,425 h and 9,808 h in the head section samples as well as in the gauge length samples (cf. figure 4.35e-h). However, the sub-grain structure starts to disappear between 1,000 h and 2,425 h. Only rare remaining structures are still visible after 2,425 h, while after 9,808 h they are completely absent. Decomposition of the sub-grain structure mainly results from thermal recovery, what is proven by the small influence of additional stress. The comparison of the head and gauge length sections show similar microstructure after equal time of annealing (compare figure 4.35e with 4.35f after 2,425 h at 100 MPa and 4.35g with 4.35h after 9,808 h at 70 MPa).

4.6.2 Particle-Free Zone Evolution

Besides the formation and decomposition of sub-grain structures, the formation of particle-free zones can be observed (cf. figure 4.35). These preferentially form along high-angle grain boundaries and their width increases over time (compare figure 4.35 after different annealing times). Particles at high-angle boundaries coarsen at the expense of small, dissolving matrix particles close to the boundaries. Thus PFZ formation

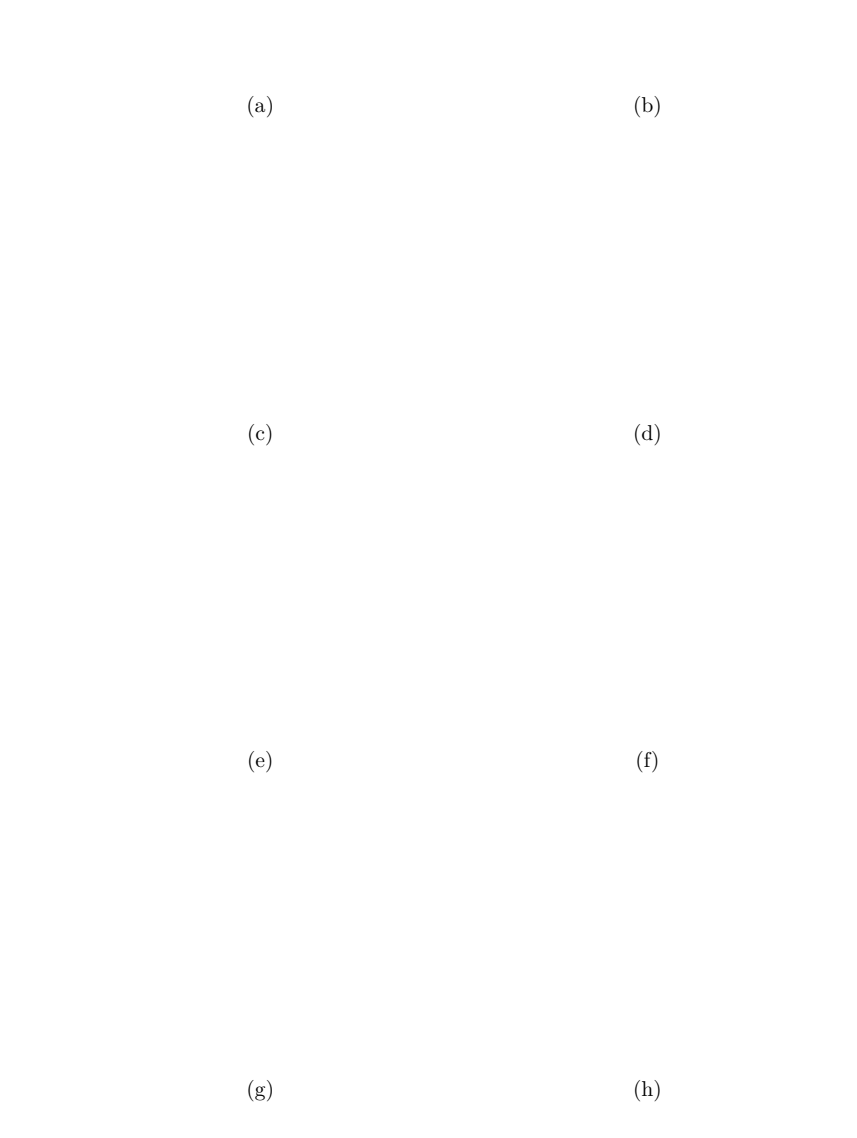


Figure 4.35: HR-FESEM images of alloy 2.5W0.57Nb0Ti at 650 °C after different annealing times: (a) 0 h (as received state), (b) 2 h, (c) 100 h, (d) 1,000 h, (e) 2,425 h (head section), (f) 2,425 h (gauge length), (g) 9,808 h (head section) and (h) 9,808 h (gauge length) [99].

and evolution is a consequence of Ostwald ripening of high-angle grain boundary particles (cf. section 2.5.2). Table 4.6 shows the mean width development and standard deviation of the PFZs after different annealing times. Mean and standard deviation are based on a min. of 11 measurements at different locations along high-angle grain boundaries.

Table 4.6: Mean width development and standard deviation of particle-free zones after different annealing times at 650 °C (in μ m).

2 h	100 h	1,000 h	$2,\!425~\mathrm{h}$	2,425 h	9,808 h	9,808 h
			(HS)	(GL)	(HS)	(GL)
0.45 ± 0.11	0.63 ± 0.18	0.87 ± 0.25	1.72 ± 0.38	1.58 ± 0.35	4.25 ± 0.63	2.74 ± 1.00

The analyses confirm the growth of PFZ width over time. Up to 2,425 h the zone width gradually increases $(0.45\pm0.11 \text{ after } 2 \text{ h} \text{ up to } 1.72\pm0.38 \text{ after } 2,425 \text{ h}$; head section) without strong variations between the measurements at different locations. In addition to increasing width, the analyses show variations between head and the gauge length sections. Direct comparison of the width display narrower zones in case of the gauge lengths $(1.72\pm0.38 \text{ (head section)} \text{ and } 1.58\pm0.35 \text{ (gauge length)} \text{ after } 2,425 \text{ h}$ or rather 4.25 ± 0.63 in case of head section and 2.74 ± 1.00 for the gauge length after 9,808 h). The reason for smaller PFZs width may be increased dislocation density because of strain localisation in these areas, which will be discussed hereafter by means of HR-TEM analyses. Moreover the gauge length zone widths vary stronger after longer annealing $(4.25\pm0.63 \text{ in case of the head section and } 2.74\pm1.00 \text{ for the gauge length after } 9,808 \text{ h annealing)}$.

As mentioned in section 2.2 the increased strength of Crofer® 22 H in comparison to its predecessor Crofer® APU is the result of additional hardening by Laves phase particles (also see [21, 22]). Thus the PFZ areas in alloy 2.5W0.57Nb0Ti may rather behave like a merely solid-solution strengthened material, because of lacking particle strengthening. This results in a drop of strength in areas close to the grain boundaries and is a potential reason for premature creep failure. Therefore in-depth analyses of the particle-free zones were performed by HR-FESEM using EBSD technique for crystal orientation mappings as well as HR-TEM for calculation of dislocation densities and investigation of dislocation motion. Band contrast images indicating grain boundaries, a misorientation mapping as well as crystal orientation after 2,425 h are shown in figure 4.36 from the head section and in figure 4.37 from the gauge length. Similar images of the head section and gauge length after 9,808 h are given in appendix C.1, Figure C.1.1 and C.1.2.

Band contrast images of the quasi stress-free head section and the stressed gauge length section show distinct formation of LAGBs in the PFZ areas in both cases (cf. Figure

4.36a and Figure 4.37a). However, the formed LAGBs in the gauge length samples show prevailing orientation perpendicular to the HAGBs, while LAGBs in the head section do not show this behaviour. Mainly perpendicular orientation in case of the gauge length can as well be observed after 9,808 h (cf. Figure C.1.1 and C.1.2; appendix C.1).

Misorientation mappings (cf. Figure 4.36b and Figure 4.37b) show orientation differences. Changes of crystallographic lattice orientation depicted in the figure 4.36e-g and figure 4.37c-e are visible as misorientations of around 1° indicated as green lines in figure 4.36b and figure 4.37b. However, most of the observed areas (bcc matrix) do not show strong misorientations (indicated in blue, cf. Figure 4.36b and Figure 4.37b). Here the misorientations are nearly 0°. Additionally greater scopes of misorientation in areas occupied by particles can be derived by the misorientation images in case of head section as well as gauge length in comparison to the PFZs. In the PFZs orientation differences can be observed as well, but these differences are only marginal. Investigation of the as received state (after hot-rolling, cf. Figure 4.38) prove that misorientations of around 1° already exist in the whole sample without the additional influence of particles. These misorientations are only caused by the preceding hot-rolling process. Furthermore a direct comparison of the mappings indicates crystal lattice relaxation processes within the PFZs (cf. Figure 4.36b, 4.37b and 4.38b), which were only reduced by particles in the samples after 2,425 h annealing. Strong misorientations are caused by particles and thus deformation of the lattice might be enhanced by the presence of dislocations. Dislocations pin at these particles and trigger stronger misorientations in these areas (cf. section 2.5.3).

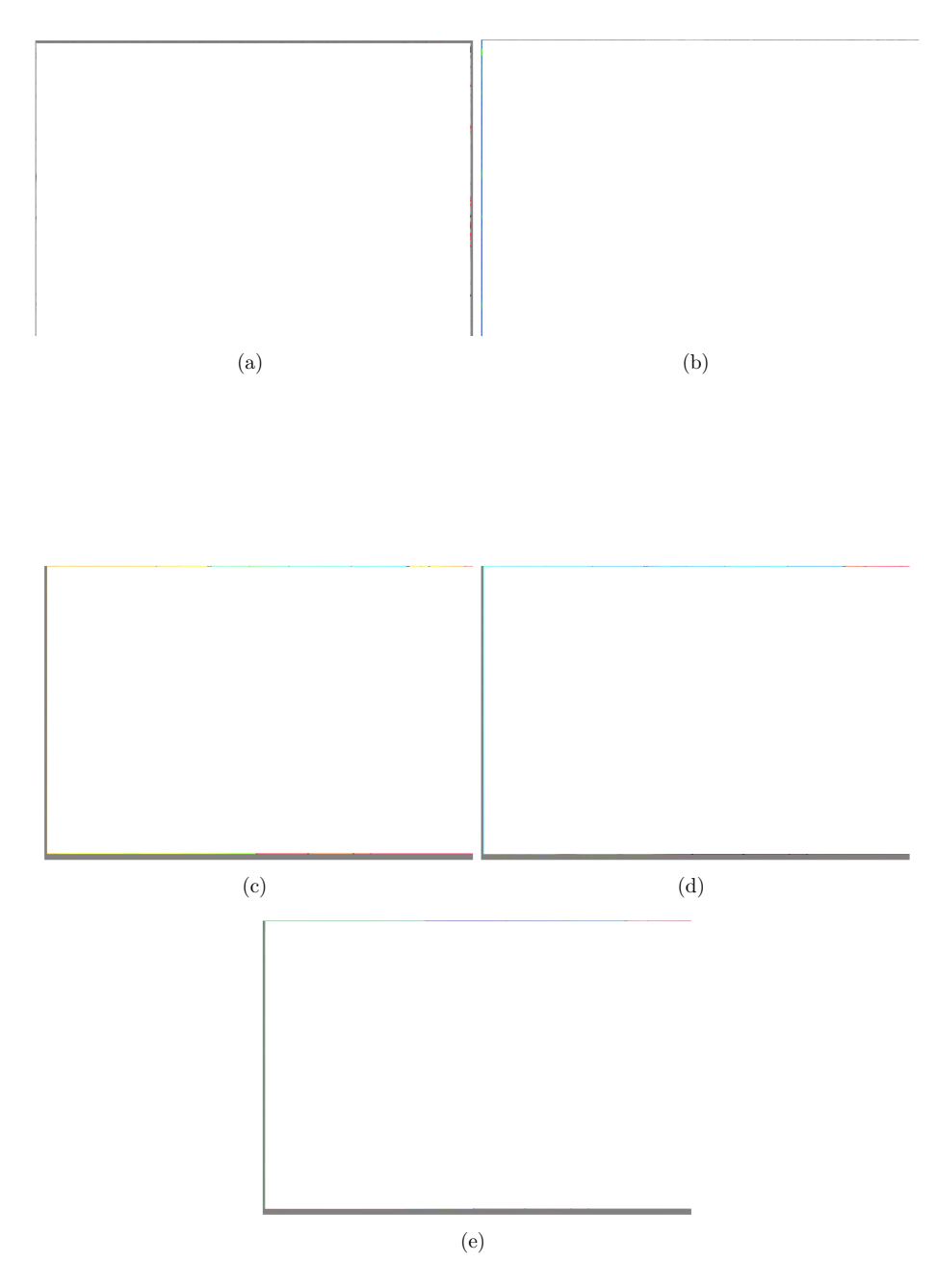


Figure 4.36: Alloy 2.5W0.57Nb0Ti at 650 °C after 2,425 h (head section): (a) Grain boundaries in band contrast images (black: high-angle, red: low-angle), (b) Misorientation mapping and crystal orientation in (c) x-direction, (d) y-direction and (e) z-direction (loading direction).

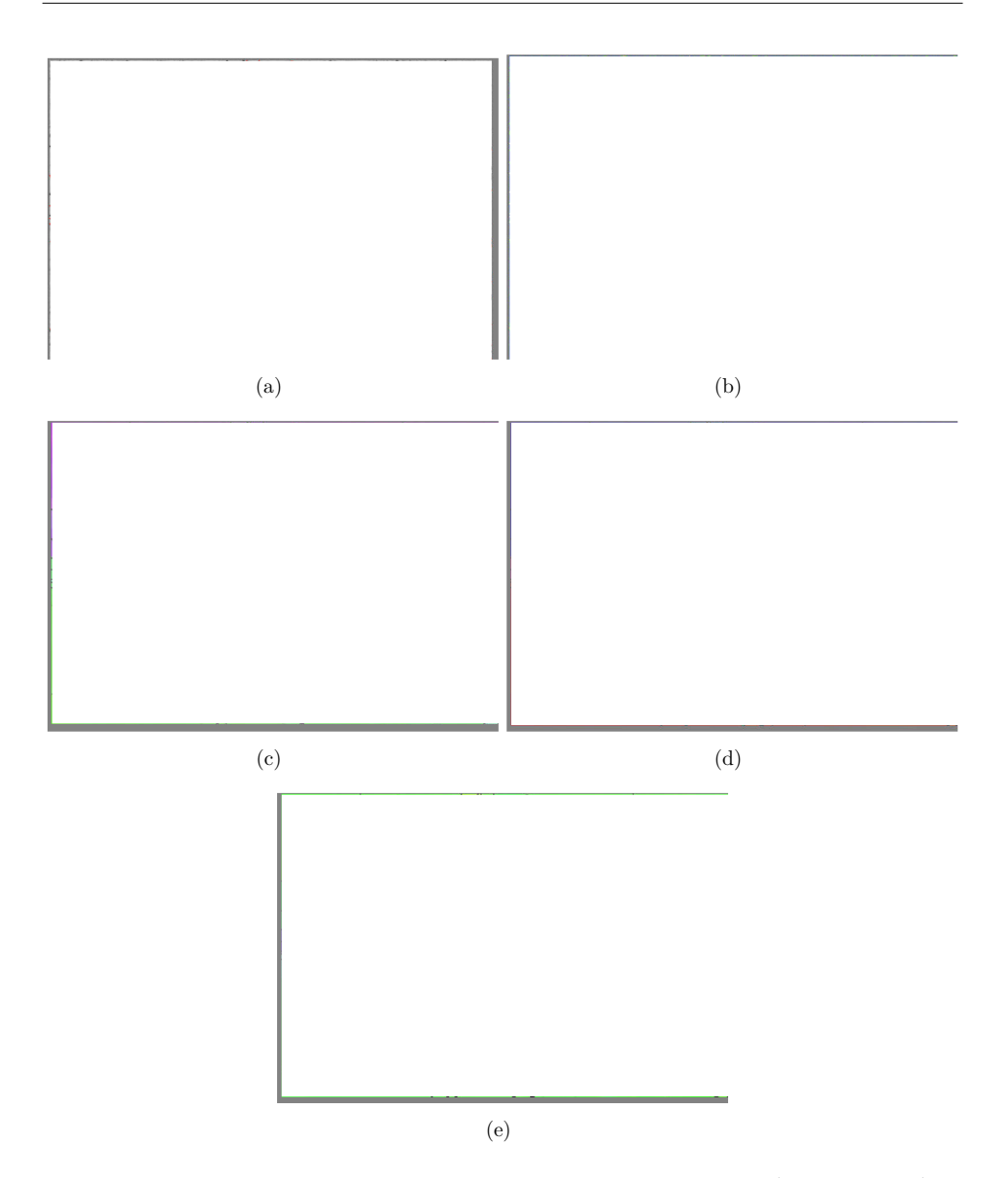


Figure 4.37: Alloy 2.5W0.57Nb0Ti at 650 °C after 2,425 h (gauge length): (a) Grain boundaries in band contrast images (black: high-angle, red: low-angle), (b) Misorientation mapping and crystal orientation in (c) x-direction, (d) y-direction and (e) z-direction (load direction).

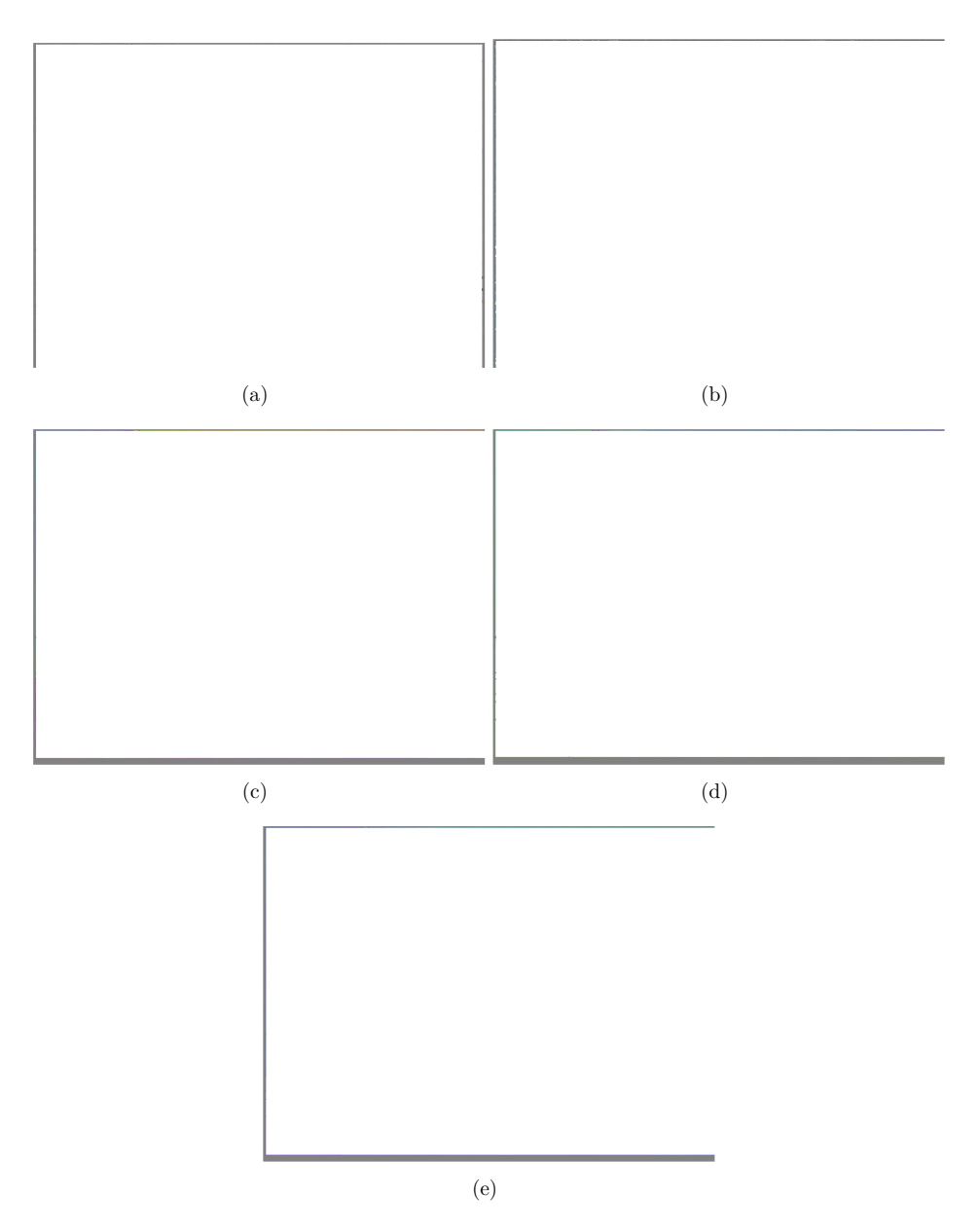


Figure 4.38: Alloy 2.5W0.57Nb0Ti after hot-rolling: (a) Grain boundaries in band contrast images (black: high-angle, red: low-angle), (b) Misorientation mapping and crystal orientation in (c) x-direction, (d) y-direction and (e) z-direction (load direction).

Further investigation of the PFZs was performed by TEM and provided additional detail information about the behaviour of dislocations in PFZs. An overview of TEM lamellae cut from the stress-free HS and the stressed GL after 2,425 h at 100 MPa and after 9,808 h at 70 MPa is given in Figure 4.39 and Figure 4.40 (white lines indicate the edges of the PFZs). Magnifications marked with "I" are given in the right column. Additional magnifications are given in appendix C.1, Figures C.1.3 to C.1.5. Areas in the right column marked by dashed lines represent the areas where the dislocation densities in the PFZs were calculated.

In all images PFZs are visible and show dependencies on time and stress. Obviously the PFZs become more pronounced with time (compare Figure 4.35c, d, e, g and the corresponding width in Table 4.6). In the presence of stress the PFZs become less pronounced (compare Figure 4.35e and f or rather Figure 4.35g and h, cf. Table 4.6). The corresponding dislocation density evolution is given in Table 4.7. The densities show the evolution of the areas marked by white dashed lines of the right column in Figure 4.39 and 4.40. For the calculation freely moveable and solitary dislocations were taken into account. Dislocations arranged in dislocation structures were neglected.

Table 4.7: Dislocation densities evaluated in the PFZs of stress-free head sections and the stressed gauge lengths after 2,425 h at 100 MPa and 9,808 h at 70 MPa (in 10^{12} m⁻²).

2,425 h (HS)	2,425 h (GL)	9,808 h (HS)	9,808 h (GL)
≈ 11.94	≈ 34.72	≈ 10.66	≈ 53.00

Regardless of annealing time both head section samples exhibit similar dislocation densities. This indicates a stable state after comparatively short time (2,425 h) in the absence of stress, while the influence of stress results in an increase of the dislocation densities. In direct comparison to the head section specimens the density increases by approx. five times in case of the 70 MPa specimen after 9,808 h and by approx. three times in case of the 100 MPa (2,425 h). Apparently the densities show an inverse dependency on the stress level and direct proportionality to the width of PFZs (compare Table 4.6 to Table 4.7)

Observation of the dislocations clearly shows a preferable orientation parallel to the grain boundaries in case of the stressed samples. This may support the accumulation of dislocations at the boundaries and thus benefit crack initiation [58] and rather cause premature failure. In addition preferable dislocation core diffusion caused by the parallel orientation decreases diffusion towards grain boundaries and thus grain boundary particle growth might be decelerated. Measurements by EDX exhibits tungsten contents of approx. 1.9 wt.% in the PFZs in case of the 100 MPa sample after 2,425 h and approx. 0.65 wt.% in case of the 70 MPa sample after 9,808 h. Thus only a third of the tungsten content remains in the PFZ matrix in case of the enhanced dislocation

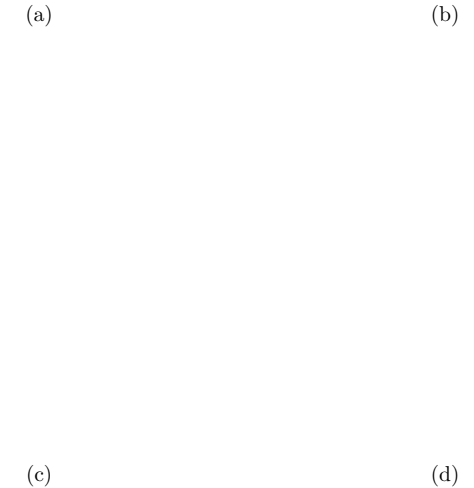


Figure 4.39: Overview TEM images (left column) and magnifications of the areas marked in red (right column) after 2,425 h at 100 MPa: a+b head section and c+d gauge length. Dashed lines of the right column indicate the areas, where dislocation densities were calculated (cf. Table 4.7) [99]. White lines in the left column indicate the edges of PFZs.

density areas of the 70 MPa sample. This might explain the increased deformation after long-term creep (9,808 h) due to lower solid solution strengthening in these areas, which also influences the nucleation of Laves phase particles. Nucleation of the particles is strongly propagated by increased dislocation density [8,100]. The reason for smaller width of the PFZs in the gauge length samples is proposed to be a combination of preferable dislocation orientation and the influence on particle nucleation and growth caused by the enhanced dislocation density and thus potentially decelerated diffusion towards boundaries. Due to insufficient available data and therefore inade-

(a)

(c)

quate statistical coverage so far, final conclusions on the relation between PFZ width, dislocation density, damage and failure cannot be drawn yet. Provision of sufficient data, optimization of chemical composition and heat treatment to minimize PFZ formation should be in the focus of further studies.



(b)

(d)

Figure 4.40: Overview TEM images (left column) and magnifications of the areas marked in red (right column) after 9,808 h at 70 MPa: a+b head section and c+d gauge length. Dashed lines of the right column indicate the areas, where dislocation densities were calculated (cf. Table 4.7) [99]. White lines in the left column indicate the edges of PFZs.

Additional to dislocation investigation within PFZs, dislocations in particle occupied areas were analysed. The overviews of TEM lamellae of the stress-free HS and the

stressed GL after 2,425 h at 100 MPa and after 9,808 h at 70 MPa are given in the left column of Figure 4.41 and Figure 4.42. The right column shows an exemplary magnification, which is marked with "I" in the left column images. Similar to the PFZs, arrangements of dislocation structures can be found, but in case of particle occupied areas the dislocation structures arrange between particles (e.g. Figure 4.41d). In general the dislocations do not show preferable orientation like the dislocations in the PFZs do. Distribution of particles is arbitrary (e.g. Figure 4.42b) and as expected the particles act as obstacles for the dislocations (e.g. Figure 4.41b). This explains the larger misorientation in these areas (e.g. see Figure 4.36), which is induced on the one hand by general lattice deformation caused by the particles itself and on the other hand by increased accumulation of dislocations at particles.



(c) (d)

Figure 4.41: Overview TEM images (left column) and magnifications of the areas marked in red indicated by "I" (right column) after 2,425 h at 100 MPa: a+b head section and c+d gauge length.



(b)

(d)

Figure 4.42: Overview TEM images (left column) and magnifications of the areas marked in red indicated by "I" (right column) after 9,808 h at 70 MPa: a+b head section and c+d gauge length.

4.7 Summary and Conclusion: Microstructure Evolution

(c)

(a)

Alloy 2.5W0.57Nb0Ti as the most creep resistant of a row of trial materials was analysed concerning sub-grain and dislocation density evolution. Visible sub-grain structures develop during short-term annealing (up to 1,000 h), because small precipitates gradually occupy sub-grain boundaries. These structures are the result of the preceding hot-rolling process, where unoccupied sub-grain structures already exist. After 1,000 h the sub-grain structures decompose continuously until disappearance by recov-

ery. Direct comparison of stress-free head section samples and stressed gauge length samples after 2,425 h at 100 MPa and after 9,808 h at 70 MPa do not show significant differences with regard to the sub-grain structure evolution. Therefore the additional influence of stress can be rated as rather small.

Apart from sub-grain structure formation, the formation of particle-free zones along high-angle grain boundaries was observed. In these zones the material acts like a solely solid-solution hardened material and thus a drop in strength is likely. Therefore the zones are suspected to have significant influence on creep damage and failure. In-depth analyses of the PFZ widths show an increase with time, but a decrease with stress. Detailed analyses by TEM show an increased number of dislocations in the particlefree zones as well as a preferred orientation parallel to the grain boundaries. This may support the accumulation of dislocations at the boundaries and thus benefits crack initiation. On the other hand the preferred orientation may decrease the diffusion towards grain boundaries and thus grain boundary particle growth might be decelerated. Comparison of the tungsten contents in the PFZs of the 70 MPa and the 100 MPa sample show strong variations depending on dislocation density. Therefore changes in solid-solution strengthening in the PFZs by tungsten can be assumed. Due to these changes in solid-solution strengthening as well as changes in dislocation density and diffusion rates the PFZs are supposed to be a main reason for material damage and failure. In areas occupied by particles the dislocations do not show preferable orientation and arrange between particles. The particles act as obstacles for the dislocations in these areas, which explains the large misorientation. Heretofore final conclusions on the relations between PFZ width, dislocation density, damage and failure cannot be drawn, because of the insufficient amount of available data and should be focus of future studies.

5 Overall Conclusion and Outlook

Transmission electron microscopy particle analyses of different fully ferritic, high chromium trial steels (18 wt.% - 23 wt.%) were performed regarding Laves phase formation and chemical particle composition at 600 °C and 650 °C. Results obtained from commercially available thermodynamic modelling software could only be proven partly regarding phase partitioning by these analyses. Also comparisons of measured and modelled chemical compositions show strong discrepancies, especially in case of the Laves phase forming elements chromium, tungsten and niobium. For further goal orientated alloy optimization of fully ferritic steels the suitability of available modelling tools is doubtful and therefore improved material databases are strongly demanded. The provided chemical compositions of this work could form the fundamental for rather advanced databases. However, this requires additional investigation of very small particles, which could not be analysed by TEM due to insufficient particle size. Further studies should focus on the investigation of very small Laves phase particles using Atom Probe Tomography (ATP). This would provide information about chemical composition and thus about kinetics in the very early stages (up to 10 h of annealing). Differing kinetics of the two individual Laves phases, which were found to be rich in niobium or rather rich in tungsten are made responsible for the variations in particle size evolution what in turn is suspected to be the reason for the encountered differences in long-term creep behaviour. Additionally the particle evolution shows improved particle stability and/or dynamic precipitation processes in one of the trial alloys, which was suspected to be the reason for its superior creep performance.

Furthermore the most creep resistant trial alloy was analysed regarding sub-grain and dislocation density evolution at 650 °C. Sub-grain structures form during short-term annealing (up to 1,000 h of annealing), but dissolve continuously until disappearance by recovery. Besides sub-grain formation, the formation of particle-free zones (PFZ) was observed. These zones form preferentially along high-angle grain boundaries and are held responsible for premature material failure due to missing particle strengthening in these areas. The zones become more pronounced with time, but less pronounced in case of superimposed mechanical stress. Dependencies of the zone width on associated dislocation density become obvious. Investigations apparently show an inverse dependency of dislocation density on the mechanical stress level and direct proportionality to the width of PFZs. Due to the orientation of the dislocations, diffusion towards grain boundaries might be decelerated. Furthermore EDX measurements confirm dif-

ferences in the remaining tungsten content of the alloy matrix and thus differences in solid-solution strengthening depending on the stress level. Additional investigation of the PFZs by ATP technique might clarify the influence of dislocation arrangements on diffusion processes and thus to the differences in solid-solution strengthening. In this case accumulation of tungsten at dislocations can be analysed atom by atom. Furthermore more analyses are needed for adequate statistical coverage to conclude the relation between PFZ width, dislocation density, damage and failure. In addition supplementary optimization should focus on minimizing PFZ width by stabilising grain boundary near particle population.

A Appendix: Thermodynamic Modelling and Verification by Electron Microscopy Examination

A.1 STEM Examination at 600 $^{\circ}$ C and 650 $^{\circ}$ C

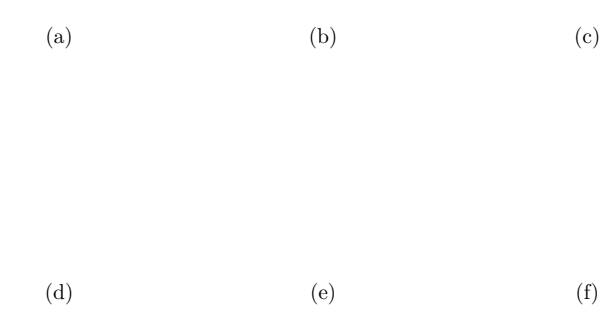


Figure A.1.1: Element mappings of dual phase particles in the head section (first row) and single-phase particles in the gauge length (second row) at 650 $^{\circ}$ C after 6,622 h in alloy 18Cr: (a)+(d) STEM-HAADF image at 200 kV, (b)+(e) mapping of Nb and (c)+(f) W.

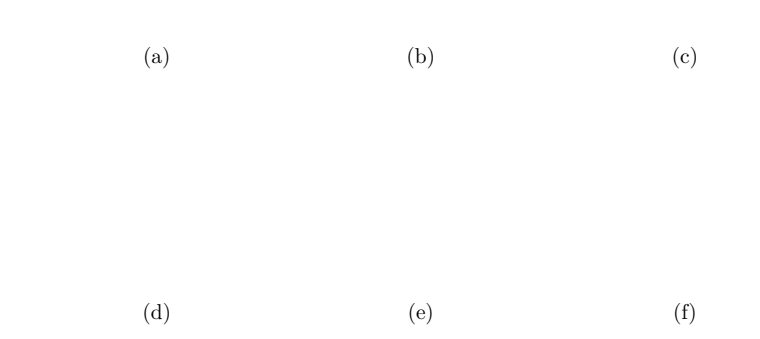


Figure A.1.2: Element mappings of dual phase particles in the head section (first row) and in the gauge length (second row) at 650 $^{\circ}$ C after 8,608 h in alloy 2.1W0.49Nb0Ti: (a)+(d) STEM-HAADF image at 200 kV, (b)+(e) mapping of Nb and (c)+(f) W.

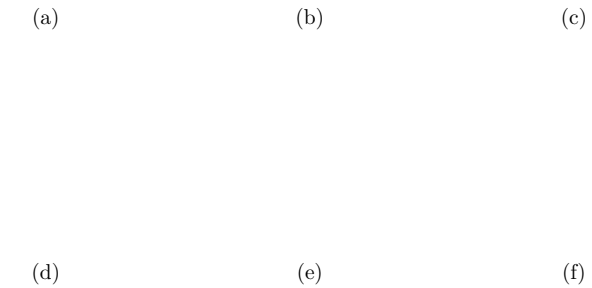


Figure A.1.3: Element mappings of dual phase particles in the head section (first row) and single-phase particles in the gauge length (second row) at 650 °C after 2,425 h in alloy 2.5W0.57Nb0Ti: (a)+(d) STEM-HAADF image at 200 kV, (b)+(e) mapping of Nb and (c)+(f) W.

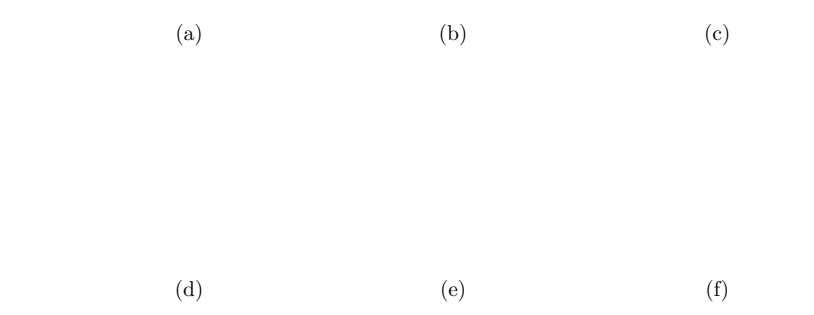


Figure A.1.4: Element mappings of single-phase particles in the head section (first row) and dual phase particles in the gauge length (second row) at 650 °C after 9,808 h in alloy 2.5W0.57Nb0Ti: (a)+(d) STEM-HAADF image at 200 kV, (b)+(e) mapping of Nb and (c)+(f) W.

A.2 Phase Distinction

A.2.1 EDX measurement

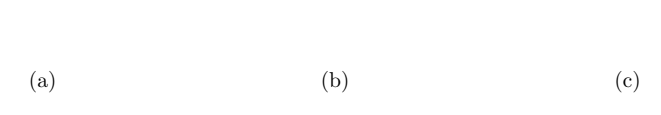
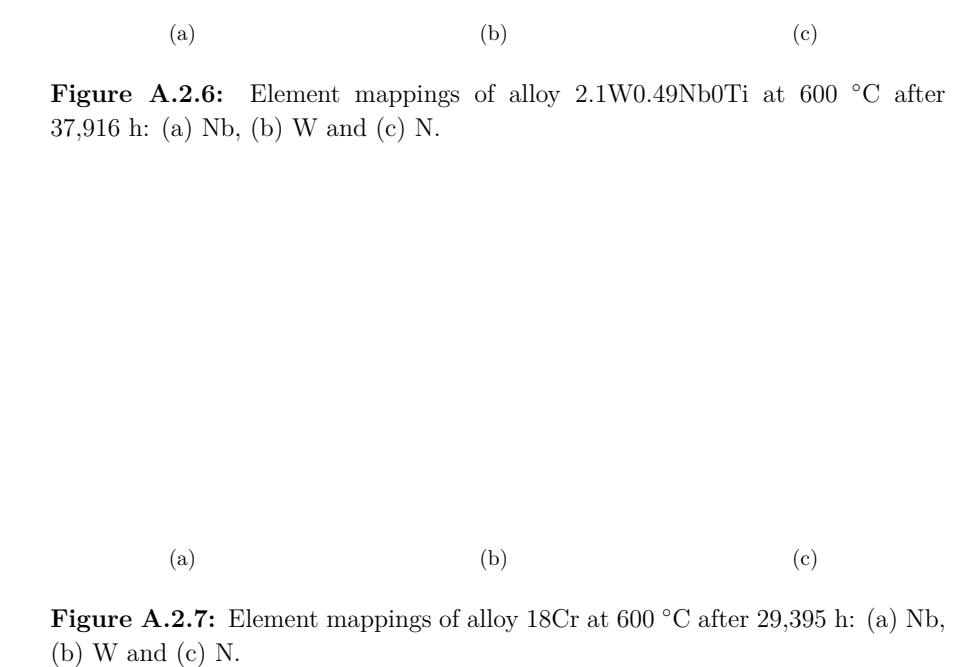


Figure A.2.5: Element mappings of alloy 2.5W0.57Nb0Ti at 650 °C after 9,808 h: (a) Nb, (b) W and (c) N.



(a) (b) (c)

Figure A.2.8: Element mappings of alloy 18Cr at 650 °C after 6,622 h: (a) Nb, (b) W and (c) N.

A.2.2 Diffraction measurement

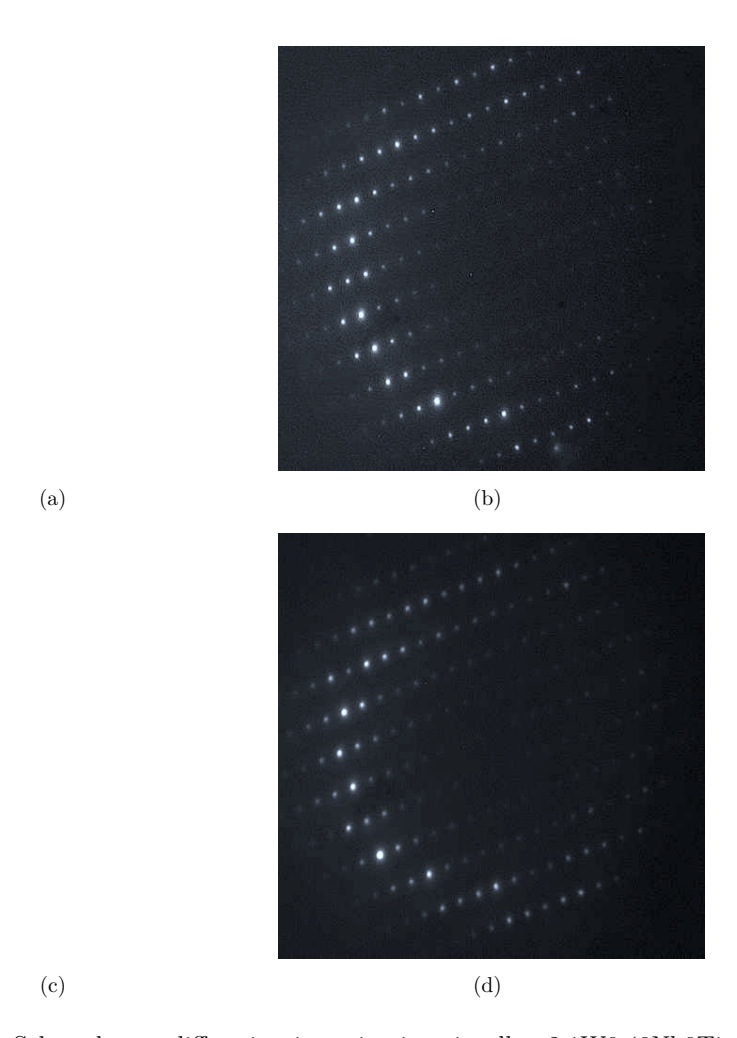


Figure A.2.9: Selected area diffraction investigations in alloy 2.1W0.49Nb0Ti after 1,000 h at 650 °C (performed by the Department of Metallurgy and Ceramics Science of the Tokyo Institute of Technology in Japan): (a) TEM image at 200 kV with HT-shell as the selected area and (b) diffraction pattern of the selected area. (c) TEM image at 200 kV with LT-core as the selected area and (b) diffraction pattern of the selected area ($\vec{b} = (11\bar{2}0)$).



B Particle Evolution

Table B.1: Considered number of particles for particle size evolution analyses in alloy 2.5W0.57Nb0Ti, 2.1W0.49Nb0Ti and 18Cr at 600 °C (NA:= Not available for this time).

	2.5W0.57Nb0Ti	2.1W0.49Nb0Ti	18Cr
2 h	971	1,557	1,293
100 h	5,395	3,253	3,315
1,000 h	3,236	3,499	3,517
26,032 h	4,707	NA	NA
29,395 h	NA	NA	2,877
37,916 h	NA	4,215	NA
40,789 h	4,075	NA	NA

Table B.2: Considered number of particles for particle size evolution analyses in alloy 2.5W0.57Nb0Ti, 2.1W0.49Nb0Ti and 18Cr at 650 °C (NA:= Not available for this time; HS:= Head section; GL:= Gauge length).

	$2.5 \mathrm{W} 0.57 \mathrm{Nb} 0 \mathrm{Ti}$	2.1 W0.49 Nb0 Ti	18Cr
2 h	1,129	769	1,345
30 h	NA	3,650 (HS)/2,121 (GL)	NA
100 h	6,399	3,454	4,296
1,000 h	2,950	20,499	3,178
2,425 h	4,243 (HS)/5,063 (GL)	NA	NA
2,500 h	NA	NA	3,840
2,579 h	NA	3,878 (HS)/3,633 (GL)	NA
6,622 h	NA	NA	2,568 (HS)/1,824 (GL)
8,608 h	NA	7,039 (HS)/3,525 (GL)	NA
9,808 h	3238 (HS)/4,582 (GL)	NA	NA

C Microstructure Evolution

C.1 Particle-Free Zone Evolution

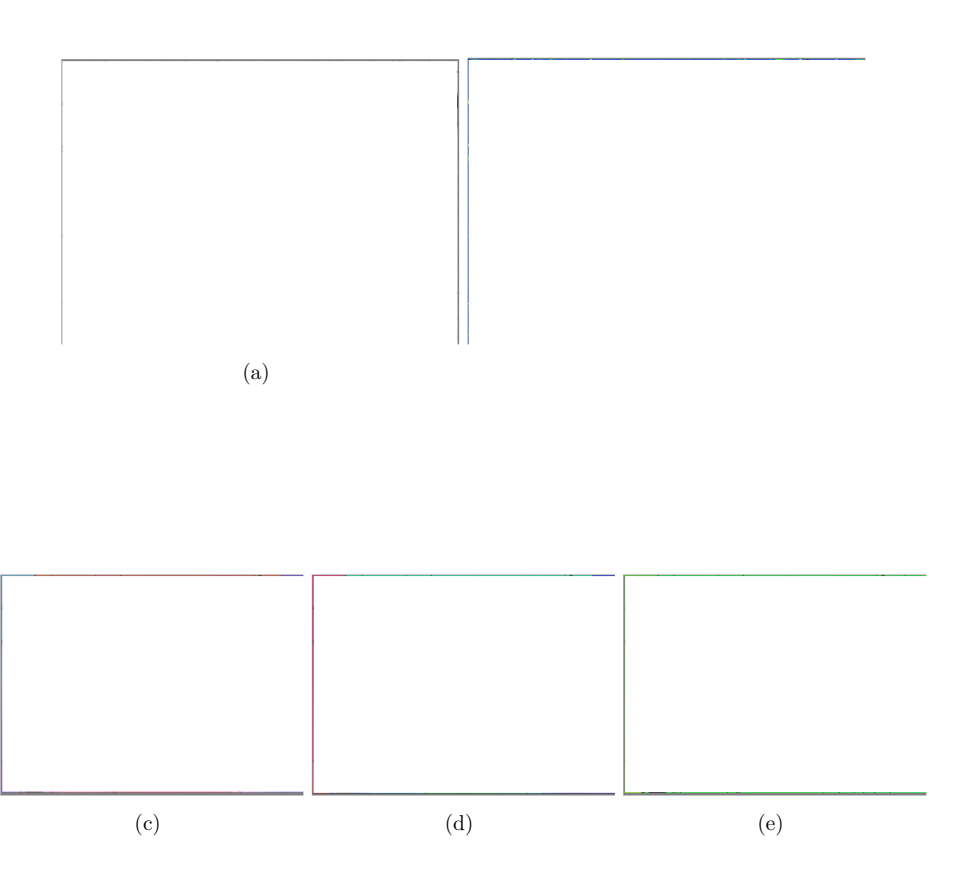


Figure C.1.1: Alloy 2.5W0.57Nb0Ti at 650 °C after 9,808 h (head section): (a) Grain boundaries in band contrast images (black: high-angle, red: low-angle), (b) Misorientation mapping and crystal orientation in (c) x-direction, (d) y-direction and (e) z-direction (loading direction).

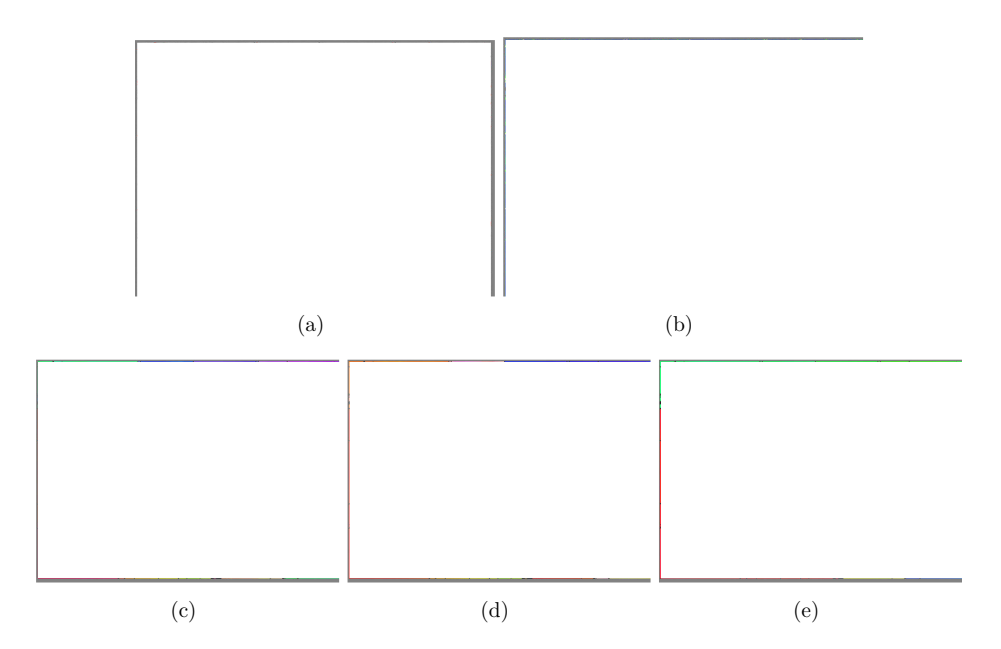


Figure C.1.2: Alloy 2.5W0.57Nb0Ti at 650 °C after 9,808 h (gauge length): (a) Grain boundaries in band contrast images (black: high-angle, red: low-angle), (b) Misorientation mapping and crystal orientation in (c) x-direction, (d) y-direction and (e) z-direction (loading direction). For colour coding of misorientation mapping and crystal orientations see figure C.1.1.

Figure C.1.3: Additional magnification of the red marked areas indicated by II of Figure 4.39 a (alloy 2.5W0.57Nb0Ti at 650 °C after 2,425 h; head section).

(a) (b)

Figure C.1.4: Additional magnifications of the red marked areas indicated by a) II and b) III of Figure 4.39 c (alloy 2.5W0.57Nb0Ti at 650 °C after 2,425 h; gauge length).

Figure C.1.5: Additional magnification of the red marked areas indicated by II of Figure 4.40 c (alloy 2.5W0.57Nb0Ti at 650 °C after 9,808 h; gauge length).

Bibliography

- [1] B. Kuhn, M. Talík et al.; Development of high chromium ferritic steels strengthened by intermetallic phases; *Materials Science and Engineering A, 594* pp. 372–380 (2014); doi: 10.1016/j.msea.2013.11.048; http://www.sciencedirect.com/science/article/pii/S0921509313012768. (citations on pages: IX, XI, 3, 8, 10, 45, 46, 49, and 81)
- [2] I. G. Wright, R. B. Dooley; A review of the oxidation behaviour of structural alloys in steam; *International Materials Reviews* 55 (3) 129–167 (2010). (citations on pages: IX, XI, 1, and 7)
- [3] W. J. Quadakkers, J. Zurek; Oxidation in steam and steam/hydrogen environments; *Shreir's Corrosion* 1 407–456 (2010). (citations on pages: IX, XI, 1, and 7)
- [4] H. K. Danielsen, J. Hald et al.; On the crystal structure of Z-phase Cr (V, Nb) N; Metallurgical and Materials Transactions A 37 (9) 2633–2640 (2006). (citations on pages: IX, XI, 1, 7, 11, and 12)
- [5] M. Schlesinger, D. Lindenberger et al.; Development of Energy Markets Energy Reference Forecast; Technical report Prognos AG, EWI Institute of Energy Economics at the University of Cologne Universität and GWS Gesellschaft für wirtschaftliche Strukturforschung (June 2014); Project No. 57/12: Study commissioned by the German Federal Ministry of Economics and Technology, Berlin. (citations on pages: 1 and 2)
- [6] Bundesministerium für Wirtschaft und Technologie; Energiekonzept für eine umweltschonende, zuverlässige und bezahlbare Energieversorgung; Technical report (September 2010). (citation on page: 1)
- [7] U.S. Energy Information Administration; The International Energy Outlook 2016; Technical report U.S. Department of Energy (May 2016); www.eia.gov/forecasts/ieo. (citations on pages: 1 and 2)
- [8] B. Kuhn, M. Talík et al.; Development Status of High performance Ferritic (HiperFer) steels; In Proc.: 8th International Conference on Advances in Materials Technology for Fossil Power Plants pp. 1019–1028 (10th 14th October 2016); ISBN-13: 978-1-62708-131-3. (citations on pages: 3 and 95)

- [9] B. Kuhn, M. Talík et al.; Ferritische Hochleistungsstähle (HiperFer) Ein Entwicklungsstatus; In 38. Vortragsveranstaltung zum "Langzeitverhalten warmfester Stähle und Hochtemperaturlegierungen" at VdeH, Düsseldorf (November 2015). (citation on page: 3)
- [10] G. Eggeler, N. Nilsvang et al.; Microstructural changes in a 12% chromium steel during creep; *Steel Res.* 58 (2) 97–103 (1987). (citation on page: 5)
- [11] K. Maruyama, K. Sawada et al.; Strengthening mechanisms of creep resistant tempered martensitic steel; *ISIJ international* 41 (6) 641–653 (2001). (citations on pages: 5, 7, and 9)
- [12] F. Abe, T.-U. Kern et al.; Creep-resistant steels; Woodhead Publishing Limited, Cambridge, England pp. 15–77 (2008). (citation on page: 5)
- [13] F. Masuyama; History of power plants and progress in heat resistant steels; *ISIJ* international 41 (6) 612–625 (2001). (citations on pages: 5 and 6)
- [14] R. Viswanathan, W. Bakker; Materials for ultrasupercritical coal power plants—Boiler materials: Part 1; *Journal of Materials Engineering and Performance* 10 (1) 81–95 (2001). (citations on pages: 5, 6, 7, and 9)
- [15] ECCC Datasheets; Steel ASTM Grade 92 (2005). (citation on page: 6)
- [16] J. Hald; Microstructure and long-term creep properties of 9–12% Cr steels; International Journal of Pressure Vessels and Piping 85 30–37 (2008). (citations on pages: 7, 8, 9, and 10)
- [17] Y. Hosoi, N. Wade et al.; Precipitation behaviour of Laves phase and it's effect on toughness of 10Cr–2Mo ferritic-martensitic steel; *Journal of Nuclear Materials* 141-143 461–467 (1986). (citations on pages: 7, 10, and 60)
- [18] J. Hald; Metallurgy and creep properties of new 9-12%Cr steels; *Steel Research* 67 (9) 369–374 (September 1996). (citations on pages: 7 and 10)
- [19] V. Metals; Werkstoffblatt Nr. 4146 (Januar 2010); http://www.vdm-metals.com/fileadmin/user_upload/Downloads/Data_Sheets/Datenblatt_VDM_ Crofer_22_APU.pdf. (citations on pages: 7 and 8)
- [20] V. Metals; Werkstoffblatt Nr. 4050 (Juni 2010); http://www.vdm-metals.com/fileadmin/user_upload/Downloads/Data_Sheets/Data_Sheet_VDM_Crofer_ 22_H.pdf. (citations on pages: 7 and 8)
- [21] J. Froitzheim, G. Meier et al.; Development of high strength ferritic steel for interconnect application in SOFCs; *Journal of Power Sources* 178 (1) 163–173 (2008). (citations on pages: 8 and 89)

- [22] B. Kuhn, C. Asensio Jimenez et al.; Effect of Laves phase strengthening on the mechanical properties of high Cr ferritic steels for solid oxide fuel cell interconnect application; *Materials Science and Engineering: A* 528 (18) 5888–5899 (2011). (citations on pages: 8, 10, and 89)
- [23] A. Christensen; Temperature factor parameters of some transition-metal carbides and nitrides by single-crystal x-ray and neutron-diffraction (1978). (citation on page: 8)
- [24] H. Goldschmidt; The Structure of Carbides in Alloy Steels; *Journal of The Iron* and Steel Institute 160 (4) 345–362 (1948). (citation on page: 8)
- [25] T. Sourmail; Precipitation in creep resistant austenitic stainless steels; *Materials science and technology* 17 (1) 1–14 (2001). (citations on pages: 9, 10, and 11)
- [26] F. Abe; Precipitate design for creep strengthening of 9% Cr tempered martensitic steel for ultra-supercritical power plants; Science and Technology of Advanced Materials (2008). (citation on page: 9)
- [27] Thermodynamics: Multicomponent Systems (22.03.2016); http://www.ualberta.ca/~ccwj/teaching/crystallography/NbC/index.html. (citation on page: 9)
- [28] Thermodynamics: Multicomponent Systems (22.03.2016); http://www.ualberta.ca/~ccwj/teaching/thermo/multicomp/. (citation on page: 9)
- [29] R. Trojko, Ž. Blažna et al.; The effect of silicon, aluminium and germanium on the stabilization of the C14 polymorph of HfMo₂; *Journal of the Less Common Metals* 92 (1) 67–74 (July 1983); doi: 10.1016/0022-5088(83)90225-4. (citations on page: 9)
- [30] F. Laves, H. Witte; Die Kristallstruktur des MgNi2 und seine Beziehungen zu den Typen MgCu2 und MgZn2; *Metallwirtschaft* 14 (33) 645–649 (1935). (citation on page: 9)
- [31] F. Stein, M. Palm et al.; Structure and stability of Laves phases. Part I. Critical assessment of factors controlling Laves phase stability; *Intermetallics* 12 713–720 (2004); doi: doi:10.1016/j.intermet.2004.02.010. (citation on page: 9)
- [32] J. S. Lee, H. G. Armaki et al.; Causes of breakdown of creep strength in 9Cr–1.8 W–0.5 Mo–VNb steel; *Materials Science and Engineering: A* 428 (1) 270–275 (2006). (citation on page: 10)
- [33] F. Abe; Effect of fine precipitation and subsequent coarsening of Fe2W laves phase on the creep deformation behavior of tempered martensitic 9Cr-W steels; Metallurgical and materials transactions A 36 (2) 321–332 (2005). (citation on page: 10)

- [34] K. Miyahara, J.-H. Hwang et al.; Aging Phenomena before the Precipitation of the Bulky Laves Phase in Fe-10%Cr Ferritic Alloy; *Scripta Metallurgica et Materialia* 32 (12) 1917–1921 (1995). (citation on page: 10)
- [35] P. J. Ennis, A. Zielinska-Lipiec et al.; Microstructual stability an creep rupture strength of the martensitic steel P92 for advanced power plant; *Acta Metallurgica* 45 (12) 4901–4907 (1997). (citations on pages: 10, 45, 46, and 47)
- [36] G. Dimmler, P. Weinert et al.; Quantification of the Laves phase in advanced 9—12% Cr steels using a standard SEM; *Materials characterization* 51 (5) 341–352 (2003). (citation on page: 10)
- [37] J. Lopez Barrilao, M. Talík et al.; Microstructure Evolution of High Temperature Fully Ferritic Steels; In Proc. 1st International Conference on Advanced High-Temperature Materials Technology for Sustainable and Reliable Power Engineering (123 HiMAT-2015), Sapporo, Japan pp. 15–18. 123rd Committee of Japan Socity for the Promotion of Science, IAI (29th June 3rd July 2015); ISBN 978-4-9908874-0-7. (citations on pages: 10, 49, 50, 60, 79, and 82)
- [38] Y. Kitano, M. Takata et al.; High resolution electron microscopy of partial dislocations in the Laves phase structure; *Journal of Microscopy* 142 (2) (1986); doi: DOI:10.1111/j.1365-2818.1986.tb02755.x. (citation on page: 10)
- [39] C. Hsieh, W. Wu; Overview of Intermetallic Sigma (σ) Phase Precipitation in Stainless Steels; International Scholarly Research Network ISRN Metallurgy, Volume 2012, Article ID 732471, doi:10.5402/2012/732471 (2012). (citations on pages: 10 and 11)
- [40] E. O. Hall, S. H. Algie; The Sigma Phase; *Metallurgical Review* 11 (1966). (citations on pages: 10 and 11)
- [41] C. H. Cooke; Trans. Australian Inst. Metals (1950). (citation on page: 10)
- [42] A.van Bennekom, F. Wilke; Delta-Ferrit-Gehalt bei Werkstoff 1.4435 und der Basler Norm II; Technical report Thyssen Krupp Steel (2001); http://www.edelstahl-rostfrei.de/downloads/iser/tb_4435_dt.pdf; Bericht 2001-4. (citation on page: 10)
- [43] G. Schulze; Die Metallurgie des Schweißens; Springer Verlang 4th edition (2010). (citations on pages: 11 and 12)
- [44] D. M. Escriba, E. Materna-Morris et al.; Chi-phase precipitation in a duplex stainless steel; *Materials Characterization* 60 (11) 1214–1219 (2009). (citation on page: 11)

- [45] O. Kubaschewski; Iron-Binary Phase Diagrams; Springer (2014); ISBN 9783662080252; https://books.google.de/books?id=oeATswEACAAJ. (citation on page: 11)
- [46] Sigma Phase (28.03.2016); http://www.geocities.jp/ohba_lab_ob_page/ Structure/Sigma_Phase.JPG. (citation on page: 11)
- [47] H. K. Danielsen, J. Hald; Behaviour of Z phase in 9–12% Cr steels; *Energy Materials* 1 (1) 49–57 (2006). (citations on page: 11)
- [48] K. Sawada, H. Kushima et al.; Z-phase formation during creep and aging in 9-12% Cr heat resistant steels; *ISIJ international* 46 (5) 769–775 (2006). (citation on page: 11)
- [49] K. H. Danielsen, J. Hald; On the nucleation and dissolution process of Z-phase Cr (V, Nb) N in martensitic 12% Cr steels; *Materials Science and Engineering:* A 505 (1) 169–177 (2009). (citations on pages: 11 and 12)
- [50] H. K. Danielsen, J. Hald; Influence of Z-phase on long-term creep stability of martensitic 9 to 12% Cr steels; VGB powertech 89 (5) (2009). (citation on page: 12)
- [51] F. Liu, M. Rashidi et al.; A new 12% chromium steel strengthened by Z-phase precipitates; *Scripta Materialia* 113 93–96 (2016). (citation on page: 12)
- [52] D. H. Jack, K. H. Jack; Structure of Z-Phase, NbCrN; *Journal of The Iron and Steel Institute* pp. 790–792 (October 1972). (citation on page: 12)
- [53] T. Gerthsen; Chemie für den Maschinenbau volume Band 1; Universitätsverlag Karlruhe (2006). (citation on page: 12)
- [54] E. Houdremont; Handbuch der Sonderstahlkunde volume Band 1+2; Springer Verlag (1956). (citations on pages: 12 and 60)
- [55] K. G. Schmitt-Thomas; Metallkunde für das Maschinenwesen volume Band 2; Spektrum Verlag (1989). (citation on page: 12)
- [56] M. Binnewies, M. Jäckel et al.; Allgemeine und Anorganische Chemie; Spekrum Akademischer Verlag 2nd edition (2011). (citation on page: 12)
- [57] H.-D. Jakubke, H. Jeschkeit; Chemie volume 1+2; Brockhaus Verlag 5th edition (1987). (citation on page: 12)
- [58] G. Gottstein; Physikalische Grundlagen der Materialkunde; Springer Verlag 3rd edition (2007); http://link.springer.com/book/10.1007%2F978-3-540-71105-6. (citations on pages: 13, 14, 15, 17, 19, 24, 25, 26, and 94)

- [59] C. Kittel; Einführung in die Festkörperphysik; Oldenbourg Verlag München Wien 14th edition (2006). (citations on pages: 14, 15, 19, 23, and 26)
- [60] Burgers-Vektor als geometrische Charakteristik von Versetzungen (16.02.2016); https://elearning.physik.uni-frankfurt.de/data/FB13-PhysikOnline/lm_data/lm_324/daten/kap_25/node30.htm. (citation on page: 16)
- [61] R. Laska, C. Felsch; Werkstoffkunde für Ingenieure; Friedr. Vieweg & Sohn, Braunschweig/Wiesbaden (1981). (citations on pages: 18 and 19)
- [62] Weitere flächenhafte Defekte im Kristall (17.02.2016); http://www.physik.uni-augsburg.de/~ferdi/skript/teil1/node11.html. (citations on page: 19)
- [63] Partialversetzungen und Stapelfehler; http://www.tf.uni-kiel.de/matwis/amat/def_ge/kap_5/backbone/r5_4_1.html. (citation on page: 19)
- [64] R. Bürgel, H. J. Maier et al.; Handbuch Hochtemperatur-Werkstofftechnik; Vieweg + Teubner Verlag 4th edition (2011). (citations on pages: 21, 26, and 28)
- [65] C. Wagner; Theorie der Alterung von Niederschlägen durch Umlösen (Ostwald-Reifung); Zeitschrift für Elektrochemie, Berichte der Bunsengesellschaft für physikalische Chemie Volume 65 (Issue 7-8) 581–591 (September 1961); doi: 10.1002/bbpc.19610650703. (citation on page: 22)
- [66] I. Lifshitz, V. V. J. Slyozov; The Kinetics of Precipitation From Supersturated Sold Solutions; *Journal of Physics and Chemistry of Solids* 19 (1-2) 35–50 (April 1961); doi: 10.1016/0022-3697(61)90054-3. (citation on page: 22)
- [67] E. Hornbogen, H. Warlimont; Metalle-Struktur und Eigenschaften der Metalle und Legierungen; Springer Verlag 5th edition (2006). (citations on pages: 24 and 26)
- [68] R. Bürgel, H. A. Richard et al.; Werkstoffmechnik volume 2. Auflage; Springer Verlag (2014). (citation on page: 26)
- [69] E. Balitchev; Thermochemische und kinetische Modellierung zur Legierungsauswahl mehrphasiger Systeme für das Thixoforming und zur Optimierung ihrer Formgebungsprozesse; Ph.D. thesis Fakultät für Bergbau, Hüttenwesen und Geowissenschaften der Rheinisch-Westfälischen Technischen Hochschule Aachen (February); http://www.mch.rwth-aachen.de/thesis_Evgueni_Balitchev.pdf. (citations on page: 27)
- [70] M.-N. de Noirfontaine, C. Girod Labianca et al.; Equilibrium Phase Diagrams; Training course (27th Septemper 2007); http://iramis.cea.fr/meetings/matgen4/Presentations/MNDN-1.pdf; MATGEN-IV, Cargese, Corsica, France. (citation on page: 27)

- [71] A. Jacob; Thermochemical Modeling of Laves Phase Containing Ferritic Steels; Dr. RWTH Aachen University Jülich (2015); ISBN 978-3-95806-070-8; http://juser.fz-juelich.de/record/203363; RWTH Aachen University, Diss., 2015. (citations on pages: 27 and 60)
- [72] G. Cacciamani; An Introduction to the Calphad Methode and the Compound Energy Formalism (CEF); *Technology in Metallurgy, Materials and Mining* 13 (1) 16–24. (citation on page: 27)
- [73] M. Knoll, E. Ruska; Das Elektronenmikroskop; *Mitteilung aus dem Hochspannungslaboratorium der Technischen Hochschule Berlin* pp. 318–339 (1932). (citation on page: 29)
- [74] C. Gerthsen, H. Kneser et al.; Physik; Springer Verlag 13th edition (1969). (citation on page: 31)
- [75] H. Ibach, H. Lüth; Festkörperphysik; Springer Verlag 2nd edition (1988). (citations on page: 33)
- [76] Image Modes in TEM Bright Field Images (11.02.2016); http://www.microscopy.ethz.ch/TEM_BF.htm. (citation on page: 34)
- [77] Image Modes in TEM Dark Field Images (11.02.2016); http://www.microscopy.ethz.ch/TEM_DF.htm. (citation on page: 34)
- [78] H.-J. Penkalla; Modern Methods of Specimen Preparation for TEM including Focused Ion Beam (FIB). (citation on page: 36)
- [79] G. Cempura, K. P. Niżnik et al.; Sample preparation methods an overview; 4th Stanislaw Gorczyca School on TEM Basics and Advanced Sample Preparation, Kraków (01.-04.09.2013). (citation on page: 36)
- [80] F. Bernhard; Handbuch der Technischen Temperaturmessung volume 2; Springer Verlag (2014). (citation on page: 37)
- [81] S. Flegler, J. Heckman Jr. et al.; Elektronenmikroskopie; Spektrum Verlag (1995). (citations on pages: 37 and 38)
- [82] Institut für Strukturphysik der TU Dresden; Versuch TEM: Transmissionselektronenmikroskopie. (citation on page: 37)
- [83] P. A. Tipler, G. Mosca; Physik; Spektrum Verlag 2nd edition (2004). (citation on page: 37)
- [84] H.-J. Penkalla; ESTEEM, Workshop on advanced sample preparation techniques for TEM, Kraków (25.06 29.06.2007). (citation on page: 37)

- [85] Datenblatt Zeiss Merlin, Analysefähigkeit im Subnanometer-Bereich (11.02.2016); http://www.zeiss.de/microscopy/de_de/produkte/rasterelektronenmikroskope/merlin-materials.html#highlights. (citation on page: 37)
- [86] LIBRA 200, Operating Manual, 344000-0000-016. (citation on page: 38)
- [87] J. Ning; Influence of chemical composition on precipitation reactions in high chromium ferritic steels; Master's thesis RWTH Aachen Institute of Ferrous Metallurgy (June 2013). (citations on pages: 42 and 73)
- [88] ECCC Datasheets; Steel ASTM Grade 92 (2014). (citations on pages: 45 and 47)
- [89] J. Lopez Barrilao, B. Kuhn et al.; Microstructure of Intermetallic Particle Strengthened High Chromium Fully Ferritic Steels; In Proc. Parsons 2015: The 9th International Charles Parsons Turbine and Generator Conference (15 Sep 2015 - 17 Sep 2015, Loughborough, UK). (citations on pages: 50, 60, 79, 82, and 84)
- [90] W. Sykes, K. van Horn; Transactions of the American Institute of Mining and Metallurgical Engineers 105 198–212 (1933). (citation on page: 60)
- [91] H. Eggers, W. Peter; Mitteilungen aus dem Kaiser-Wilhelm-Institut fuer Eisenforschung 20 198–203 (1938). (citation on page: 60)
- [92] R. Genders, R. Harrison; The Journal of the Iron and Steel Institute 140 29–37 (1939). (citation on page: 60)
- [93] Y. Kato, M. Ito et al.; Effect of Si on Precipitation Behavior of Nb-Laves Phase and Amount of Nb in Solid Solution at Elevated Temperature in High Purity 17% Cr-0.5% Nb Steels; *Materials transactions* 51 (9) 1531–1535 (2010). (citation on page: 60)
- [94] N. Oono, H. Nitta et al.; Diffusion of niobium in α -iron; Materials Transactions 44 (10) 2078–2083 (2003). (citation on page: 60)
- [95] S. Takemoto, H. Nitta et al.; Diffusion of tungsten in α -iron; *Philosophical Magazine* 87 (11) 1619–1629 (2007). (citation on page: 60)
- [96] F. Chassagne, P. Santacreu; Ferritischer Edelstahl mit 19 % Chrom, der mit Niob stabilisiert ist (18. Juli 2012); http://www.google.com.ar/patents/EP1818422B2?cl=de; EP Patent 1818422. (citation on page: 71)
- [97] W. Chen; Precipitation reactions in high-chromium ferritic steels regarding thermomechanical pre-treatment and chemical; Master's thesis RWTH Aachen Institute of Ferrous Metallurgy (June 2013). (citations on pages: 73 and 74)

- [98] P. Ennis, A. Czyrska-Filemonowicz; Recent advances in creep-resistant steels for power plant applications; *Sadhana* 28 (3-4) 709–730 (2003). (citation on page: 83)
- [99] J. Lopez Barrilao, B. Kuhn et al.; Microstructure and Intermetallic Particle Evolution in Fully Ferritic Steels; *Proc.: 8th International Conference on Advances in Materials Technology for Fossil Power Plants* pp. 1029–1037 (10th 14th October 2016); ISBN-13: 978-1-62708-131-3. (citations on pages: 88, 95, and 96)
- [100] Z. W. Hsiao, B. Kuhn et al.; The influence of deformation on the precipitation behavior of a ferritic stainless steel; In J. Lecomte-Beckers, O. Dedry et al., editors, 10th Liege Conference: Materials for Advanced Power Engineering 2014 (14-17th of September 2014). (citation on page: 95)

List of Figures

1.1	Gross electricity and world net electricity by energy source	2
2.1	International research projects on AFM steels	5
2.2	Development of ferritic-martensitic steels for boilers with their pro-	
	posed 10^5 h proposed rupture strength at 600 °C	6
2.3	Nominal chemical composition of AFM steels for boilers	6
2.4	Lattice structure of TiC, TiN and (c) $Cr_{23}C_6$	9
2.5	Examples for Laves phase structure types and stacking orders: ${\rm MgZn_2},$	
	(C14) ${\rm MgCu}_2$ (C15) and ${\rm MgNi}_2$ (C36)	10
2.6	Phase equilibrium diagram of the Fe-Cr-system	11
2.7	Tetragonal lattice structure of the σ -phase	11
2.8	Tetragonal lattice structure of Z-phase	12
2.9	Overview of different point defects	13
2.10	Schematic illustration of an edge dislocation	14
2.11	Schematic illustration of a screw dislocation	15
2.12	Combined dislocation with location-dependent dislocation line	15
2.13	Circulation in a disordered crystal and an ideal crystal with Burgers	
	vector	16
2.14	Schematic illustration of a symmetric tilt boundary, dependence of	
	dislocation distance on tilt angle between grains and Schematic illus-	
	tration of an antisymmetric tilt boundary.	17
2.15	Schematic illustration of lattice deformation at a HAGB	18
2.16	Different types of phase boundaries	19
2.17	Stacking fault of a cubic close-packed structure with structure order	
	ABCABC.	19
2.18	Changes in free enthalpy regarding the precipitate radius r of globular	0.4
0.10	particles	21
2.19	Schematic illustration of dislocation movement induced by shear stress,	20
0.00	which moves the upper part of the crystal rightwards	23
2.20	Formation of kinks during intersection of dislocations	24
2.21	Annihilation of dislocations and sub-grain formation.	24
2.22	Cutting of a particle and Orowan mechanism	25

2.23	Development of the stress during particle cutting $\sigma_S \approx \sqrt{r_T}$ and the	
	Orowan stress $\sigma_{\rm OR} \approx -\frac{1}{r_{\rm T}}$	26
2.24	Schematic illustration of a physical creep curve ($\sigma = \text{const.}$) and tech-	20
	nical creep curve ($F = const.$)	28
2.25	Schematic architecture and beam path	31
2.26	Bragg condition	33
2.27	Ewald-construction	33
2.28	Optical path of bright field and dark field	34
2.29	Sample and magnification of the hole after electrolytic polishing	35
2.30	Individual steps of replica preparation	36
2.31	Imaging example of a FIB lamelle	36
2.32	Lift-out grid with FIB lamella	37
2.33	Dependence of acceleration voltage interaction	38
3.1 3.2	Creep specimen position of taken samples	40
3.3	evolution	42
3.4	regard to the cut plane	43 43
	Creep curves of the 2.5W0.57Nb0Ti, 2.1W0.49Nb0Ti and 18Cr alloys	
4.1	at 600 °C and 650 °C in comparison to P92	46
4.2	Comparison of the stress rupture properties of the 2.5W0.57Nb0Ti, 2.1W0.49Nb0Ti and 18Cr trial alloys and P92	47
4.3	Schematic illustration of the generation of a counter magnetic field in case of electrolytically polished sample and TEM image of a trial alloy prepared with the replica method	48
4.4	Mass fractions of Laves phases and σ -phase of alloy 2.5W0.57Nb0Ti, 2.1W0.49Nb0Ti and 18Cr	49
4.5	Dual phase particles with HT-shell and LT-core after 1,000 h at 600 $^{\circ}$ C and 650 $^{\circ}$ C in alloy 18Cr and 2.1W0.49Nb0Ti	51
4.6	Element mappings of dual phase particles at 600 °C after 1,000 h in alloy 18Cr and 2.1W0.49Nb0Ti	52
4.7	Element mappings of dual phase particles at 650 °C after 1,000 h in	02
	alloy 18Cr and 2.1W0.49Nb0Ti	52
4.8	Potentially dual phase particles with HT-shell and LT-core after 1,000 h at 600 °C and at 650 °C in alloy $2.5W0.57Nb0Ti$	53
4.9	Element mappings of dual phase particles in alloy 2.5W0.57Nb0Ti after 1,000 h at 600 °C and 650 °C.	54
4.10	Single phase particles in the grain interiors after 1,000 h at 600 °C and 650 °C in alloy 2.5W0.57Nb0Ti, 2.1W0.49Nb0Ti and 18Cr	55
4.11	Element mappings after 10 h of annealing at 600 °C and 650 °C	56
1.11	Example mappings area to n of announing at ooo C and ooo C	50

4.12	Single phase particles after long-term annealing at 600 °C in alloy 18Cr, 2.1W0.49Nb0Ti and 2.5W0.57Nb0Ti	57
4.13	Representative element mappings of single phase particles after long-term annealing at 600 °C	58
4.14	Particles in the quasi stress-free head sections at 650 °C of alloy 18Cr, 2.1W0.49Nb0Ti and 2.5W0.57Nb0Ti.	59
4.15	Particles in the stressed gauge length sections at 650 °C of alloy 18Cr, 2.1W0.49Nb0Ti and 2.5W0.57Nb0Ti	59
4.16	EDX spectrum of HT phase and LT phase	61
4.17	Chemical composition of alloys $2.1W0.49Nb0Ti$ and $18Cr$ at $600^{\circ}C$ after different annealing steps in comparison with calculated (TC) equi-	62
1 10	librium compositions	62
4.18 4.19	Chemical composition at 600 °C of alloy 2.5W0.57Nb0Ti Comparison of chemical composition at 650 °C of head section and	63
4.20	gauge length of alloys 18Cr, 2.1W0.49Nb0Ti and 2.5W0.57Nb0Ti Chemical compositions of alloy 2.5W0.57Nb0Ti, 2.1W0.49Nb0Ti and 18Cr at 650 °C after different annealing steps in comparison with TC equilibrium compositions	64 66
4.21	Differences in modelled and measured chemical compositions at 600 °C and 650 °C after different annealing steps.	67
4.22	Measured chemical composition of (Fe,Cr)-σ-phase in comparison to TC modelling of alloy 2.5W0.57Nb0Ti and 2.1W0.49Nb0Ti	69
4.23	Exemplary forescattered electron images of long-term head section samples at 600 °C	69
4.24	EBSD phase map (superimposed with band contrast image) of alloy 2.5W0.57Nb0Ti at 600 °C after 40,789 h	70
4.25	Element mappings after 40,789 h at 600 °C in alloy 2.5W0.57Nb0Ti	70
4.26	EBSD phase map (superimposed with band contrast image) of alloy 2.1W0.49Nb0Ti at 650 °C after 8,608 h	71
4.27	Element mappings after 8,608 h at 650 °C from alloy 2.1W0.49Nb0Ti.	71
4.28	EBSD phase map (superimposed with band contrast image) of alloy 2.5W0.57Nb0Ti at 650 $^{\circ}\mathrm{C}$ (9,808 h), 2.1W0.49Nb0Ti at 600 $^{\circ}\mathrm{C}$	
4.00	(37,916 h) and (18Cr at 600 °C (29,395 h.) and (d) at 650 °C (6,622 h).	72
4.29	Selected area diffraction investigations in alloy 2.1W0.49Nb0Ti after 1,000 h of annealing at 650 °C	73
4.30	Influence of image magnification on particle size distribution	74
4.31	Development of particle size distribution in terms of equivalent circle diameter at 600 °C and 650 °C for 2.5W0.57Nb0Ti, 2.1W0.49Nb0Ti	5 0
4.00	and 18Cr.	79
4.32	Temperature comparison of particle size distribution in terms of equivalent circle diameter at 600 $^{\circ}$ C and 650 $^{\circ}$ C	82

4.33	Comparison of stress-free and stressed particle number fraction at 70 MPa	84
4.34	Comparison of particle number fraction in stress-free head sections and stressed gauge lengths at 100 MPa and 145 MPa	85
4.35	HR-FESEM images of alloy 2.5W0.57Nb0Ti at 650 °C after different annealing times	88
4.36	Band contrast images, grain boundaries, misorientation mapping and crystal orientation of alloy 2.5W0.57Nb0Ti at 650 °C after 2,425 h (head section)	91
4.37	Band contrast images, grain boundaries, misorientation mapping and crystal orientation of alloy 2.5W0.57Nb0Ti at 650 °C after 2,425 h	
4.38	(gauge length)	92 93
4.39	Overview TEM images of alloy 2.5W0.57Nb0Ti after 2,425 h at 100 MPa.	95
4.40	Overview TEM images of alloy 2.5W0.57Nb0Ti after 9,808 h at 70 MPa.	96
4.41	Overview TEM images after 2,425 h at 100 MPa (grain interior)	97
4.42	Overview TEM images after 9,808 h at 70 MPa (grain interior)	98
A.1.1	Element mappings of dual phase particles in the head section and single-phase particles in the gauge length at 650 °C after 6,622 h in alloy 18Cr	103
A.1.2	Element mappings of dual phase particles in the head section and in	104
A.1.3	Element mappings of dual phase particles in the head section and single-phase particles in the gauge length at 650 $^{\circ}\mathrm{C}$ after 2,425 h in	104
A.1.4	Element mappings of single-phase particles in the head section and dual phase particles in the gauge length at 650 $^{\circ}$ C after 9,808 h in	105
A.2.5	·	105
A.2.6		106
A.2.7		106
	Element mappings of alloy 18Cr at 650 °C after 6,622 h: (a) Nb, (b) W	106
A.2.9	Selected area diffraction investigation in alloy 2.1W0.49Nb0Ti after	107
C.1.1	Band contrast image, misorientation mapping and crystal orientation of alloy 2.5W0.57Nb0Ti at 650 °C after 9,808 h (head section)	111
C.1.2	Band contrast image, misorientation mapping and crystal orientation	112

C.1.3	Additional TEM magnifications of alloy 2.5W0.57Nb0Ti at 650 $^{\circ}\mathrm{C}$ af	
	ter 2,425 h; head section	112
C.1.4	Additional TEM magnifications of alloy 2.5W0.57Nb0Ti at 650 $^{\circ}\mathrm{C}$ af	
	ter 2,425 h; gauge length	113
C.1.5	Additional TEM magnifications of alloy 2.5W0.57Nb0Ti at 650 $^{\circ}\mathrm{C}$ af	
	ter 9,808 h; gauge length	113

List of Tables

2.1	Chemical composition of Crofer [®] 22 APU	7
2.2	Chemical composition of Crofer® 22 H	7
3.1	Chemical compositions of trial alloys $2.5 \mathrm{W} 0.57 \mathrm{Nb} 0 \mathrm{Ti}, \ 2.1 \mathrm{W} 0.49 \mathrm{Nb} 0 \mathrm{Ti}$	
	and 18Cr (in wt.%)	39
3.2	Overview about the annealing time steps, temperatures and type of annealing of alloy 2.5W0.57Nb0Ti, 2.1W0.49Nb0Ti and 18Cr	40
4.1	Median and variance of the particle diameters in the 2.5W0.57Nb0Ti,	
	2.1W0.49Nb0Ti and 18Cr alloys at 600 °C	76
4.2	Median and variance of the particle diameters in the 2.5W0.57Nb0Ti,	70
4.9	2.1W0.49Nb0Ti and 18Cr alloys at 650 °C	76
4.3	Associated particle size distribution values of alloy 2.5W0.57Nb0Ti at 600 °C and 650 °C	80
1.4	Associated particle size distribution values of alloy 2.1W0.49Nb0Ti at	80
11	600 °C and 650 °C	81
4.5	Associated particle size distribution values of alloy 18Cr at 600 °C and	01
	650 °C	83
4.6	Mean width development and standard deviation of particle-free zones	
	after different annealing times at 650 °C	89
4.7	Dislocation densities evaluated in the PFZs of stress-free head sections	
	and the stressed gauge lengths	94
В.1	Considered number of particles for particle size evolution in alloy	
	2.5W0.57Nb0Ti, 2.1W0.49Nb0Ti and 18Cr at 600 °C	109
B.2	Considered number of particles for particle size evolution in alloy	
	2.5 W 0.57 Nb 0 Ti, 2.1 W 0.49 Nb 0 Ti and $18 Cr$ at 650 °C	109

Danksagung

An dieser Stelle möchte ich die Gelegenheit nutzen, um nachstehenden Personen für die fachliche und persönliche Unterstützung zur Erstellung meiner Promotionsschrift zu danken.

Mein Dank gilt zunächst meinem Doktorvater Univ.-Prof. Dr. Lorenz Singheiser sowie Univ.-Prof. Dr. Tilmann Beck für das Ermöglichen dieser Arbeit am Institut für Energie- und Klimaforschung, Werkstoffstruktur und -eigenschaften (IEK-2) und die Begutachtung meiner Dissertation. Außerdem danke ich Univ.-Prof. Dr. Robert Spatschek für die Übernahme des Korreferates und Univ.-Prof. Dr. Bernd Markert für die Übernahme des Vorsitzes. Ferner möchte ich mich für die angenehme Atmosphäre in der mündlichen Prüfung bedanken.

Ein ganz besonderer Dank gilt Dr. Bernd Kuhn für die hilfreiche Betreuung, seine jederzeit offene Tür, guten Ratschläge und Diskussionen sowie seine Geduld.

Ich danke Dr. Egbert Wessel für die Unterstützung bei den unzähligen mikroskopischen Untersuchungen und die fachlichen Gespräche, die mir während der gesamten Zeit sehr geholfen haben.

Bei den Kolleginnen und Kollegen des IEK-2 möchte ich mich für die nette Unterstützung und Zusammenarbeit während meiner Doktorandenzeit bedanken. Im Speziellen bedanke ich mich bei Dr. Erik Skiera, Marita Offermann und Torsten Fischer für die kritische Durchsicht der Arbeit, konstruktiven Anmerkungen sowie für die nützlichen Diskussionen und ihre aufbauenden Worte.

Des Weiteren danke ich Volker Gutzeit und Jörg Bartsch für die Hilfestellung bei der metallografischen Präparation meiner Proben und Daniela Eßer für die Anfertigung der FIB Lamellen.

Für die Durchführung meiner Auslagerungsversuche und mechanischer Tests sowie hilfreichen Gesprächen möchte ich außerdem Daniela Liebert, Alexander Moser, Harald Reiners und Burkhard Werner danken.

Furthermore I want to thank the colleagues Prof. Dr. Masao Takeyama and Dr. Satoru Kobayashi from the Department of Metallurgy and Ceramics Science of the Tokyo Institute of Technology in Japan for the selected area diffraction investigations of my specimen.

Ein großes Dankeschön gilt meiner lieben Freundin Franziska Kaesmacher und Simon für die Aufmunterung und Ermutigungen in den richtigen Momenten.

Den größten Dank schulde ich meinem Verlobten Dr. Marius Wirtz für die liebevolle Unterstützung. Ich bedanke mich dafür, dass er mir stets den Rücken frei gehalten hat, für das große Verständnis, auch wenn er Ziel meiner schlechten Laune wurde, für das Motivieren, wenn der Himmel für mich voller schwarzer Wolken hing und für die hilfreichen Diskussionen und Bemerkungen beim Korrekturlesen.

Zuletzt möchte ich meinen Eltern und meinem Bruder danken, dass sie immer an mich geglaubt haben und ohne die ich nie so weit gekommen wäre und möchte meinem verstorbenen Vater diese Arbeit widmen.

Schriften des Forschungszentrums Jülich Reihe Energie & Umwelt / Energy & Environment

Band / Volume 362

Process-based modelling of regional water and energy fluxes taking into account measured neutron intensities by cosmic-ray probes

R. Baatz (2017), xvi, 135 pp ISBN: 978-3-95806-211-5

Band / Volume 363

Quantitative Analyse der Lithiumverteilung in Kathoden- und Elektrolyt-Dünnschichten für Festkörperbatterien

C. Dellen (2017), vi, 161 pp ISBN: 978-3-95806-214-6

Band / Volume 364

Intragruppentrennung Seltener Erden mittels neuer phosphororganischer Liganden

S. Hadić (2017), VIII, 164 pp ISBN: 978-3-95806-215-3

Band / Volume 365

Automated Magnetic Divertor Design for Optimal Power Exhaust

M. Blommaert (2017), xxiv, 220 pp ISBN: 978-3-95806-216-0

Band / Volume 366

PEM-Elektrolyse-Systeme zur Anwendung in Power-to-Gas Anlagen

G. Tjarks (2017), IV, 135 pp ISBN: 978-3-95806-217-7

Band / Volume 367

Fundamental Insights into the Radium Uptake into Barite by Atom Probe Tomography and Electron Microscopy

J. Weber (2017), IX, 160 pp ISBN: 978-3-95806-220-7

Band / Volume 368

Entwicklung von elektronenleitenden Schutzschichten gegen die anodische Auflösung von Stromsammlern in neuartigen "Dual-Ionen"-Energiespeichern

G. Teucher (2017), VIII, 119 pp ISBN: 978-3-95806-222-1

Band / Volume 369

Herstellung und Charakterisierung oxiddispersionsverstärkter Haftvermittlerschichten

J. Bergholz (2017), V, 133, II pp ISBN: 978-3-95806-223-8

Schriften des Forschungszentrums Jülich Reihe Energie & Umwelt / Energy & Environment

Band / Volume 370

Performance of Plasma Facing Materials under Thermal and Plasma Exposure

I. Steudel (2017), XVI, 150 pp ISBN: 978-3-95806-226-9

Band / Volume 371

The Impact of Transient Thermal Loads on Beryllium as Plasma Facing Material

P. Spiller (2017), VII. 134 pp.

B. Spilker (2017), XII, 134 pp ISBN: 978-3-95806-227-6

Band / Volume 372

Analysis and Simulation of Macroscopic Defects in $Cu(ln,Ga)Se_2$ Photovoltaic Thin Film Modules

B. Misic (2017), iv, 147 pp ISBN: 978-3-95806-228-3

Band / Volume 373

Chemical and physical properties of sodium ionic conductors for solid-state batteries

M. Guin (2017), ix, 126 pp ISBN: 978-3-95806-229-0

Band / Volume 374

Prediction of Oxidation Induced Life Time for FCC Materials at High Temperature Operation

R. Duan (2017), vi, 180 pp ISBN: 978-3-95806-230-6

Band / Volume 375

Microstructure Evolution of Laves Phase Strengthened Ferritic Steels for High Temperature Applications

J. K. Lopez Barrilao (2017), XVI, 134 pp

ISBN: 978-3-95806-231-3

Weitere Schriften des Verlags im Forschungszentrum Jülich unter

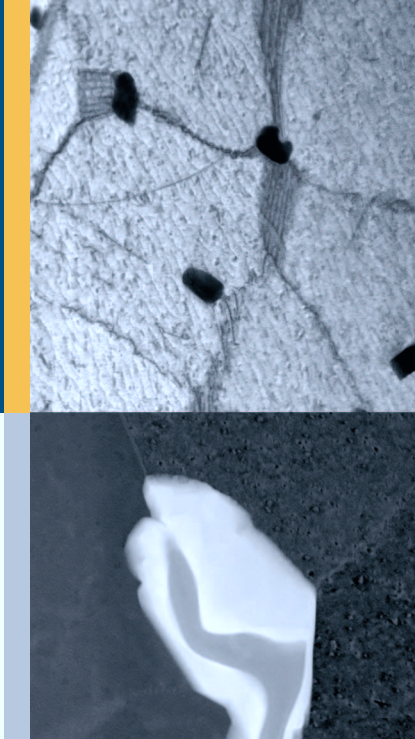
http://wwwzb1.fz-juelich.de/verlagextern1/index.asp

Microstructure Evolution of Laves Phase Strengthened Ferritic Steels for High Temperature Applications

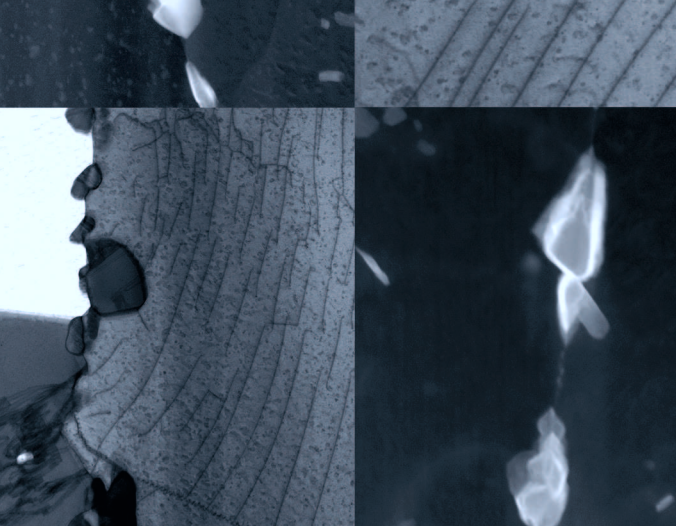
Jennifer Katharina Lopez Barrilao

375

Microstructure of Laves Phase Strengthened Steels







JÜLICH

J.K. Lopez Barrilao

Energie & Umwelt/ **Energy & Environment** Band/Volume 375 ISBN 978-3-95806-231-3



Energie & Umwelt/ Energy & Environment Band/Volume 375 ISBN 978-3-95806-231-3

